January 2023

Dynamics Of Flood Flow In Red River Basin

Vida Atashi

Recommended Citation

Atashi, Vida, "Dynamics Of Flood Flow In Red River Basin" (2023). *Theses and Dissertations*. 5228.
https://commons.und.edu/theses/5228

DYNAMICS OF FLOOD FLOW IN RED RIVER BASIN

by

Vida Atashi
B.Sc., Agricultural Engineering-Irrigation, Shahid Chamran University of Ahvaz, 2010
M.Sc., Hydraulic Structures, Shahid Chamran University of Ahvaz, 2012
Ph.D., Hydraulic Structures, Shahid Chamran University of Ahvaz, 2017

A Dissertation
Submitted to the Graduate Faculty
of the
University of North Dakota
in partial fulfillment of the requirements

for the degree of
Doctor of Philosophy

Grand Forks, North Dakota

May
2023

Name: Vida Atashi

Degree: Doctor of Philosophy

This document, submitted in partial fulfillment of the requirements for the degree from the University of North Dakota, has been read by the Faculty Advisory Committee under whom the work has been done and is hereby approved.

DocuSigned by:
Yeo H. Lim
E2D755C3824A4F5...
Yeo Howe Lim

DocuSigned by:
Taufique Mahmood
3F7DA8280EB4408...
Taufique Mahmood

DocuSigned by:
Gregory Vandeberg
5BD33C4CBF8B463...
Gregory S. Vandeberg

DocuSigned by:
Jeffrey VanLooy
1051975BE648413...
Jeffrey VanLooy

DocuSigned by:
Sven Egenhoff
F4360391FFDF47E...
Sven Egenhoff

This document is being submitted by the appointed advisory committee as having met all the requirements of the School of Graduate Studies at the University of North Dakota and is hereby approved.

DocuSigned by:
Chris Nelson
2E0AF088C733403...
Chris Nelson
Dean of the School of Graduate Studies

5/2/2023
Date

PERMISSION

Title	Dynamics of Flood Flow in Red River Basin
Department	Civil Engineering
Degree	Doctor of Philosophy

In presenting this dissertation in partial fulfillment of the requirements for a graduate degree from the University of North Dakota, I agree that the library of this University shall make it freely available for inspection. I further agree that permission for extensive copying for scholarly purposes may be granted by the professor who supervised my dissertation work or, in his absence, by the Chairperson of the department or the dean of the School of Graduate Studies. It is understood that any copying or publication, or other use of this dissertation or part thereof for financial gain shall not be allowed without my written permission. It is also understood that due recognition shall be given to me and to the University of North Dakota in any scholarly use which may be made of any material in my dissertation.

Vida Atashi
April 24th, 2023

Acknowledgments

I can honestly express that my academic journey would not have been possible without the constant technical guidance, support, and tremendous belief received by my Ph.D. advisors Dr. Yeo H. Lim and Dr. Taufique Mahmood. I am deeply grateful for the continuous help and generous collaboration that have helped me grow both personally and academically. I would like to thank my committee members, Dr. Jeffrey VanLooy, Dr. Gregory Vandeberg, and Dr. Sven Egenhoff for providing their valuable time and their presence.

I would like to thank Dr. Reza Barati and Dr. Hamed Taheri Gorji for their unwavering support and for allowing me to work on fascinating projects.

Thanks to Civil Engineering Graduate Programs, North Dakota Water Resources Research Institute (NDWRRI), and the School of Graduate Studies for providing continuous financial support during my Ph.D. studies.

My heart is filled with an overwhelming sense of gratitude and love for the incredible people who have helped shape me into the person I am today. First and foremost, I must express my deep appreciation to ***baba***, who taught me to always look for the good in every situation and to never give up on my dreams. To ***maman***, who has raised me to be an ambitious and determined woman, and your bravery and resilience have inspired me to push myself beyond my limits. You, both, have always given me motivation and taught me to be determined and strong throughout my path, while I am pursuing my goals. To ***Sepideh*** and ***Mehdi*** who have always been by my side, offering your unwavering support and love, I am eternally grateful for your presence in my life. To **Ramtin**, your kindness, patience, and support made this journey possible. Your motivating words kept me going when the going got hard. Thank you for being such a great companion!

And finally, I must express my deep appreciation to all of my wonderful friends, who have challenged me to think and feel in new ways and have been there for me through thick and thin.

As this journey ends, another begins and I can’t wait to enjoy post-Ph.D. life among all my beloved friends and family, and I look forward to whatever the future holds.

To the women of Iran and around the world, who inspire me every day with their courage, resilience, and unwavering commitment to freedom.

I am dedicating this dissertation to you, who fighting for women's rights and equality in Iran and worldwide.

You are not alone, and you are not forgotten.

I’m quoting my favorite part from the book “Man's Search for Meaning”: “Everything can be taken from a man but one thing: the last of the human freedoms—to choose one’s attitude in any given set of circumstances, to choose one’s own way.”

Abstract

In recent decades, flooding has become a major issue in many areas of the Upper Midwest. Many rivers and streams in the region had considerable increases in mean annual peak flows during this period, which was driven by a combination of natural factors including discharge synchrony with the spring thaw, ice jams, glacial lake plain, and a decrease in gradient downstream. The Red River of the North is a prominent river in the United States and Canada's Upper Midwest. It flows from its headwaters in Minnesota and North Dakota to Lake Winnipeg in Manitoba. The river is well-known for its spring floods, which can cause havoc on communities along its banks. There is an increasing need to improve the characterization and identification of precursors in the Red River basin that affect the hydrological conditions that cause spring snowmelt floods and improve predictions to reduce Red River flood damage.

This dissertation has developed different research that concerns the dynamics of floods in the Red River basin by integrating hydrological, hydraulic, and machine-learning models. The primary objectives were to improve flood prediction accuracy by deriving the parameters of the Muskingum Routing method using discharge measurements obtained by an Autonomous Surface Vehicle, to predict scour potential of the river through HEC-RAS modeling, and to provide an estimate of the flood progression downstream based on the flow characteristics. The study also compared the effectiveness of Seasonal Autoregressive Integrated Moving Average (SARIMA), Random Forest (RF), and Long Short-Term Memory (LSTM) algorithms for flood prediction. Additionally, the research investigated the surface water area variation and response to wet and dry seasons across the entire Red River basin, which can inform the development of effective flood mitigation strategies. The results of this study contributed to a better understanding of flood control strategies in the Red River Basin and helped to inform policy decisions related to flood mitigation in the region. Ultimately, this research aimed to understand the complex dynamics of the RRB and derive hydrological and hydraulic models that could help to improve flood prediction.

The first research developed a linear and nonlinear Muskingum model with lateral inflows for flood routing in the Red River Basin using Salp Swarm Algorithm (SSA). The distributed Muskingum model is introduced to improve the accuracy and efficiency of the calculations. The study focuses on developing a linear and nonlinear Muskingum model for the Grand Forks and Drayton USGS stations deriving the parameters of the Muskingum Routing method using discharge measurements based on spatial variable exponent parameters. The suggested approach minimizes the Sum of Square Errors (SSE) between observed and routed outflows. The results show for an icy river like Red River, the Muskingum method proposed is a convenient way to predict outflow hydrographs caused by snowmelt.

The second study improved flood inundation mapping accuracy in flood-prone rivers, such as the Red River of the North, by using simulation tools in HEC-RAS for flood modeling and determining Manning's n coefficient. An Autonomous Surface Vehicle (ASV) was used to collect bathymetry and discharge data, including a flood event with a 16.5-year return period in 2022. The results showed that Manning's n-coefficient of 0.07 and 0.15 for the channel and overbanks, respectively, agreed well with the observed and simulated water level values under steady flow conditions. The study also demonstrated the efficiency of using ASVs for flood mapping and examined the scour potential and any local scour development in the streambed near the bridge piers.

The third study of this dissertation used hourly level records from three USGS stations to evaluate water level predictions using three methods: SARIMA, RF, and LSTM. The LSTM method outperformed the other methods, demonstrating high precision for flood water level prediction. The results showed that the LSTM method was a reliable choice for predicting flood water levels up to one week in advance. This study contributes to the development of data-driven forecasting systems that provide cost-effective solutions and improved performance in simulating the complex physical processes of floods using mathematical expressions.

This last study focused on the spatiotemporal dynamics of surface water area in the Red River Basin (RRB) by using a high-resolution global surface water dataset to investigate the changes in surface water extent from 1990 to 2019. The results showed that there were four distinct phases of variation in surface water: wetting (1990-2001), dry (2002-2005), recent wetting (2006-2013), and recent drying (2014-2019). The transition from bare land to permanent and seasonal water area was observed during the wetting phase, while the other phases experienced relatively little fluctuation. Overall, this study contributes to a better understanding of the spatiotemporal variation of surface water area in the RRB and provides insights into the impact of recent wetting and drying periods on the lakes and wetlands of the RRB.

Table of Contents

List of Tables

List of Figures

CHAPTER 1. INTRODUCTION

1.1. Background

Studying floods is important because they can have significant impacts on human populations and infrastructure. Floods can cause damage to buildings, roads, and other structures, as well as disrupt transportation and communication networks. They can also lead to loss of life and injuries, and cause displacement of communities. Understanding the causes and patterns of floods, as well as predicting and managing them, can help minimize the negative impacts of floods on society. Flood prediction in rivers is important for several reasons:

1. Early warning: Flood prediction allows for early warning to be issued to at-risk communities, giving them time to prepare and evacuate if necessary.
2. Emergency response: With accurate flood predictions, emergency services can better prepare and respond to potential floods, minimizing the loss of life and property damage.
3. Infrastructure protection: With accurate flood predictions, communities and governments can take action to protect critical infrastructure such as dams, levees, and bridges from potential damage.
4. Water management: Flood predictions can be used to manage water resources, such as controlling the release of water from dams to prevent downstream flooding.
5. Economic benefits: Accurate flood predictions can help minimize economic losses by allowing businesses and industries to prepare and protect their assets.
6. Climate adaptation: Flood predictions can be used as a tool to better understand and adapt to the impacts of climate change on river systems.
7. Research and Development: Flood predictions can be used to support research and development of new technologies, models, and strategies to improve flood

prediction and management capabilities.

With this introduction, there is an increasing need to improve the characterization and identification of precursors that affect the hydrological conditions that cause spring snowmelt floods and improve predictions to reduce Red River flood damage.

The Red River of the North, which flows through the states of Minnesota and North Dakota in the United States, as well as the province of Manitoba in Canada, has a long history of flooding [1] with records dating back to the 17th century. One of the most devastating flood years in the history of the Red River of the North was 1997, which resulted in extensive damage to infrastructure and the displacement of thousands of people. Another significant flood year was 2009, which was caused by a combination of snowmelt and heavy precipitation, leading to widespread flooding in the region. These floods, as well as several other major floods that have occurred in the region, have resulted in significant loss of life and property damage.

Red River discharge varies annually and seasonally, and the water demand of the Red River basin may rise in the future due to a variety of factors, including economic development, population growth, and climate change [2]. Due to a long and severe winter for snow accumulation, warmer temperatures in the spring, and flat topography with weak permeability soil, the mid-latitude regions of North America are highly vulnerable to spring-melt floods [2]. Spring-melt floods are frequent in the Red River as it heads North [3, 4]. During the spring thaw, the southern part of the Red River basin melts first, and the river becomes hydrologically active; meanwhile, the northern part of the basin is often frozen. Along with the flat and homogenous topography, the river activity forms a slow, meandering river, which causes an overflow in the Red River of the North on the northern side, resulting in floods [5-8]. Surface runoff from snowmelt during significant floods leads the Red River to overflow its shallow banks, flooding the whole valley and causing immense damage. Researches by Hirsch and Ryberg (2012) and Rice et al. (2015) indicate that the frequency of floods in the Red River basin is increasing dramatically [9, 10].

Flood management efforts in the Red River of the North have been ongoing for many years. Over time, these efforts have become more sophisticated, with the development of advanced flood forecasting and warning systems, as well as land-use planning and zoning regulations to reduce the risk of flooding. However, the Red River of the North continues to be a flood-prone area, and there are ongoing efforts to improve flood management and mitigation strategies.

1.2. Research Objectives

The objective of the dissertation was to provide an understanding of the Red River's complex dynamics in order to improve flood prediction through a combination of hydrological, hydraulic, and machine-learning models. Specifically, the study aimed to improve flood prediction accuracy by understanding the routing process and enhancing parameter estimation using the Muskingum method, calibrated hydraulic models using Autonomous Surface Vehicle measurements to predict scour potential, and comparing the performance of classical statistical, classical machine learning, and deep learning algorithms for flood prediction in the Red River. Furthermore, the study sought to expand the scope of analysis to the entire Red River basin, examining surface water area variation and response to wet and dry seasons, which could contribute to the development of effective flood mitigation strategies. By combining these four projects, that study provided a comprehensive understanding of the factors affecting flood prediction accuracy in the Red River basin, contributing to the development of a more effective flood management system in the region.

1.3. Dissertation Outline

This dissertation is organized as follows. Four major studies were conducted to explore various approaches to improve flood prediction in the Red River. In Chapter 2, the Muskingum method was applied to understand the process of flood routing in the Red River and improve the parameters for flood prediction in the Red River. Chapter 3 focused on improving flood prediction in the Red River by employing a flood hydraulic model calibration approach. This involved predicting the scour potential of extreme flood events triggered by snowmelt, using advanced ASV (Autonomous Surface Vehicle) measurements. By calibrating the hydraulic model, this study has enhanced flood prediction accuracy and ultimately contribute to effective flood mitigation strategies. Chapter 4, classical statistical methods, classical machine learning algorithms, and deep learning methods were used to predict floods in the Red River. Chapter 5 expanded the scope of the study to the entire Red River basin to give a more critical assessment of surface water area variation and detect surface water area response to wet and dry seasons. Finally, chapter 6 concludes the dissertation by summarizing the main findings, discussing their implications for practice and policy, identifying limitations and directions for future research, and overall contribution to the field.

1.4. Publications

This section contains the journal published while working on the Ph.D. Peer-Reviewed conference papers and more published journal papers were not part of the Ph.D. projects and are not included in this dissertation.

Peer-Reviewed Journal Papers

J.1. **V. Atashi**, H. T. Gorji, S. M. Shahabi, R. Kardan, and Y. H. Lim, "Water Level Forecasting Using Deep Learning Time-Series Analysis: A Case Study of

Red River of the North," Water, vol. 14, no. 12, p. 1971, 2022.

J.2. **V. Atashi** and Y. H. Lim, "Flood Hydraulic Model Calibration and Scour Potential Prediction Based on Advanced ASV-Measured Extreme Flood Events Triggered by Snowmelt," Remote Sensing, 2023, (under review).

J.3. **V. Atashi**, M. H. Taufique, and K. Rasouli, "Impacts of climatic variability on surface water area observed by remotely sensed imageries in the Red River Basin," Geocarto International, 2023, (under review).

J.4. **V. Atashi**, R. Barati, and Y. H. Lim. "Development of A Distributed Muskingum Model for River Flood Routing Incorporating Lateral Flow Using Whale Optimization Algorithm, " Journal of Hydroinformatics, 2023, (under review).

2 CHAPTER 2. Red River Flood Routing Using a Spatial Variable Exponent Parameter Nonlinear Muskingum Model and Salp Swarm Algorithm by Considering Lateral Flow

2.1. Introduction and Background

Flood routing is the process of simulating the movement of water in a river or stream system during a flood event using mathematical models. The goal of flood routing is to predict the behavior of the water as it moves through the system, including the peak flow, the timing of the peak flow, and the overall duration of the flood. Generally, two basic approaches are used to route flood waves in natural channels: hydrologic (lumped) and hydraulic routing. The hydrologic (lumped) method relies on the storage continuity equation, whereas the hydraulic method relies on the Saint-Venant equations, which include the continuity and momentum equations [11, 12].

The Muskingum model is a widely accepted flood routing model due to its adequate levels of accuracy and the reliable relationships between its parameters and channel properties. The traditional Muskingum model seeks a method of parameter estimation to determine the values of wave travel time, K, and weight coefficient of discharge, x.

However, the linear Muskingum model leads to considerable inaccuracy in the forecast of flood behavior throughout its propagation along a river because natural channel reaches often have a nonlinear storage-discharge connection. To address this limitation, models such as the Muskingum model have been modified to account for the nonlinearity of flow movement processes. Gill introduced a nonlinear storage equation using the exponent of the Muskingum storage equation as the third parameter [13], and later models such as the Non-Linear Muskingum model (NLMM) have been developed to include lateral inflows and better simulate the nonlinear processes of flood movements in rivers. The NLMM with the lateral flow (NLMM-L) has been suggested as an accurate solution method for addressing the nonlinear Muskingum model [14-21].

The fourth order Runge-Kutta method has been offered as an accurate and acceptable solution method among the different explicit solution methods for addressing the nonlinear Muskingum model since it is simpler than the Runge-Kutta-Fehlberg method [22, 23].

The Salp Swarm Algorithm (SSA) is a metaheuristic optimization technique inspired by the behavior of salps, a type of marine organism. SSA simulates the movement and behavior of salps in the search for optimal solutions to optimization problems introduced by Mirjalili et. al [24]. In this algorithm, each individual solution is represented as a salp, and the population of salps evolves over time as they interact with each other and with their environment. Sarming behavior of salps is a type of marine animal belonging to the Salpidae family [25]. Salps have a transparent barrel-shaped bodies and move through the water by pumping it through their body. In deep oceans, salps form a swarm called a salp chain [26]. The proposed mathematical model for moving salp chains divides the population into two groups: leader and followers and defines the position of all salps in an n-dimensional search space. It is assumed that there is a food source called F in the search space as the swarm's target. There is little in the literature to mathematically model the swarming behaviors and population of salps [27, 28]. SSA has been successfully applied to a variety of optimization problems in engineering, science, and finance, and has shown to be a competitive alternative to other metaheuristic algorithms such as Particle Swarm Optimization and Genetic Algorithms. To the best of our knowledge, there is no prior research that has utilized the Salp Swarm Algorithm to create a model for the Muskingum method.

Mirjalili et. al [24] propose a new nature-inspired optimization technique based on the swarming behavior of salps, called Sthe alp Swarm Algorithm (SSA) and its multi-objective variant, called Multi-Objective Salp Swarm Algorithm (MSSA). Two mathematical models are proposed to update the position of leading and follower salps, and both algorithms are shown to be effective in solving both benchmark and real-world optimization problems with unknown search spaces. The performance of SSA and MSSA is compared with other well-known algorithms in the literature using statistical tests, and it is found that SSA and MSSA outperform these algorithms in a statistically significant manner. The paper recommends further research in applying these algorithms to single- and multi-objective problems in different fields, proposing binary versions of the algorithms, and investigating the impacts of different constrained handling methods on their performance.

In short, the objective of this research is to develop a nonlinear Muskingum model for two Red River USGS stations, Grand Forks and Drayton, to estimate the parameters of the nonlinear Muskingum models (*K, x, m,* and *β*) by using the distributed Muskingum to improve the accuracy of the procedure by splitting a reach into numerous periods, with the Muskingum model calculations conducted individually for each interval.

2.2. Methodology

2.2.1. Study Area

The Red River Basin is an international watershed shared by the United States and Canada, with 80% of its area in the former (North Dakota, South Dakota, and Minnesota) and 20% in the latter (Manitoba). The Red River of the North is a major river in this basin that flows from south to north through the Red River Valley, which was formed by a glacial lake Agassiz remnant. The basin is around 60 miles wide and 315 miles long, with a total area of 45,000 square miles [1]. The climate is semi-arid, with cold winters and hot, dry summers, and most of the streamflow occurs in spring and early summer due to snowmelt or heavy rainfall [2]. The flat terrain and climatic conditions often lead to severe floods in the Red River and its tributaries during wet seasons, particularly in spring and early summer. The river's floodplain is broad and shallow, which makes it susceptible to flooding during heavy rainfalls or spring snowmelt. Some of the most devastating floods in North American history have occurred along the Red River. Atashi et. al studied the performance of classical statistical, machine learning, and deep learning methods in forecasting water levels for flood warning systems evaluated. Results showed that the Long Short-Term Memory (LSTM) method outperformed the other methods in terms of accuracy and precision, making it a reliable choice for flood prediction, especially for downstream stations without any discharge information available [29].

During a high-flow period in the spring snowmelt period, it is necessary to observe the flow hydrographs at upstream and downstream cross-section pairs. Drayton (station No. 05092000) and Grand Forks (station No. 05082500), which are existing USGS streamflow gauging stations, are chosen for flow observation because they are the only two stations from Grand Forks to the US-Canada border that provide streamflow data that enable researchers to study hydrographs (Figure 2-1). The other stations, Pembina, and Oslo, only provide gauge height information. The discharge flow of these two dataset stations is collected from USGS'S mean daily discharge. Fourteen different flood events between 1990 and 2022 are sampled to calibrate and verify the model summarized in Table 2-1.

Figure 2-1- Location of USGS stations on Red River in Pembina, Drayton, and Grand Forks

Table 2-1- Characteristics of the water level time series at two hydrology stations of the Red River

Station Name	Period	No. and Type of Events	Frequency
Drayton	1990-2022	16-flood	Daily
Grand Forks	1990-2022	16-flood	Daily

2.2.2. Muskingum Model

The Muskingum method is a popular hydrological modeling technique used for predicting flood routing in rivers and streams. It is a simple and practical model that has been widely used for several decades in the field of hydrology. In this section, we will explain the Muskingum model in detail, including its mathematical formulation and the associated equations.

The Muskingum method is based on the principle of conservation of mass and momentum, which assumes that the discharge at a point in the river is equal to the inflow minus the outflow [30]. This method uses a linear reservoir approach to model the river channel, in which the channel is divided into a series of reaches with equal lengths. Each reach is characterized by two parameters, namely, the reach time delay (K) and the reach weighting factor (x).

The reach time delay (K) is the time required for the water to travel through the reach, which is dependent on the channel geometry, roughness, and other hydraulic characteristics. The reach weighting factor (x) is the proportion of the discharge that enters the reach from the upstream section, which is also known as the weighting coefficient. These parameters can be determined using various techniques, including trial and error, optimization algorithms, and regression analysis. The Muskingum model can be represented mathematically as follows [31]:

$$S = K[xI + (1 - x)O] \qquad (2\text{-}1)$$

where O is the discharge at the downstream end of the reach (m^3/s), I is the discharge at the upstream end of the reach (m^3/s). x is the weighting factor for the reach (ranges between 0 and 0.5 for reservoir storage and between 0 and 0.3 for stream channels [32]), K is the time delay for the reach(s), and S is the storage volumes of the reach (m^3). By combining equation 2-1 with continuity equation an explicit equation can be obtained to calculate the outflow at the next time step:

$$O_2 = C_0 I_2 + C_1 I_1 + C_2 O_1 \qquad (2\text{-}2)$$

The subscripts 1 and 2 on I and O represent the values at time t_1 and t_2 respectively. C_0, C_1, and C_2 are the coefficients.

The nonlinear Muskingum method is an extension of the classical Muskingum method, which allows for a better representation of the nonlinear relationship between the inflow and outflow in the river channel. This method is based on the principle of conservation of mass and momentum, and it uses a nonlinear reservoir approach to model the river channel. Previous research has advocated a nonlinear Muskingum model for accounting for nonlinearity which is presented in equation 2-3 [13, 32-35]:

$$S = K[xI_t + (1 - x)O_t]^m \qquad (2\text{-}3)$$

where *m* takes the nonlinearity without lateral flow into the models. These models feature an extra parameter m (= exponent power), which may be calculated using various parameter estimation approaches. Equation 2-4 shows modified storage equation that considers lateral flow.

$$\frac{dS}{dt} = \frac{\Delta S}{\Delta t} = (1 + \beta)I_t - O_t \qquad (2\text{-}4)$$

where β is the parameter accounting for the lateral flow. The storage at time t+1 is shown in equation below.

$$S_{t+1} = S_t + \Delta S \qquad (2\text{-}5)$$

By substituting Equation 2-4 into Equation2-5, the storage at time t+1 considering lateral flow in a nonlinear relationship between the inflow and outflow will represent in Equation 2-6:

$$S_t = K[(1 + \beta)xI_t + (1 - x)Q_t]^m \qquad (2\text{-}6)$$

2.2.3. Distributed nonlinear Muskingum model incorporating lateral flows

Hosseini (2009) developed a concept for the linear Muskingum flood routing model to perform it in a river by considering multi-reach [36]. Vatankhah (2014) proposed the Fourth order Runge-Kutta approach as a numerical method to solve the ordinary first order differential equations of nonlinear Muskingum models [22]. Karahan et al. (2015) presented a nonlinear Muskingum model taking the contribution from lateral flow in flood routing calculations [37].

In the present study, a distributed nonlinear Muskingum model incorporating lateral inflows has been developed. Nonlinear Muskingum models can be considered as a cascade of nonlinear Muskingum reaches. Figure 2-2 illustrates the concept of distributed nonlinear Muskingum model. As it can be seen, one, two, three, or more equal nonlinear Muskingum sub-reaches can be used to represent the flow behavior of a single reach. Only one set of hydrological model parameters (*K*, *x,* and *m*) must be calibrated and used in the nonlinear routing calculations. Starting from the main inflow hydrograph at the upstream section, this flood hydrograph can be routed to the downstream section of the first sub-reach. Then, the routed flood hydrograph at the end of the first sub-reach is used as inflow for the second sub-reach and is routed subsequently to the downstream section of the second sub-reach [38]. This sequential procedure is repeated to obtain the flood hydrograph at the downstream section of the final sub-reach. The number of sub-reaches (*NR*) can be determined by a trial-and-error approach. In other words, the model could be calculated for one, two, three, or more sub-reaches and the best results between different *NR* options could be selected by comparing an objective function value and other performance evaluation criteria. The continuity and storage equations used in the distributed nonlinear Muskingum model incorporating lateral inflows are as follows:

$$\frac{dS_t^j}{dt} = (1+\beta)Q_t^{j-1} - Q_t^j \tag{2-7}$$

$$S_t^j = K\left[(1+\beta)xQ_t^{j-1} + (1-x)Q_t^j\right] \tag{2-8}$$

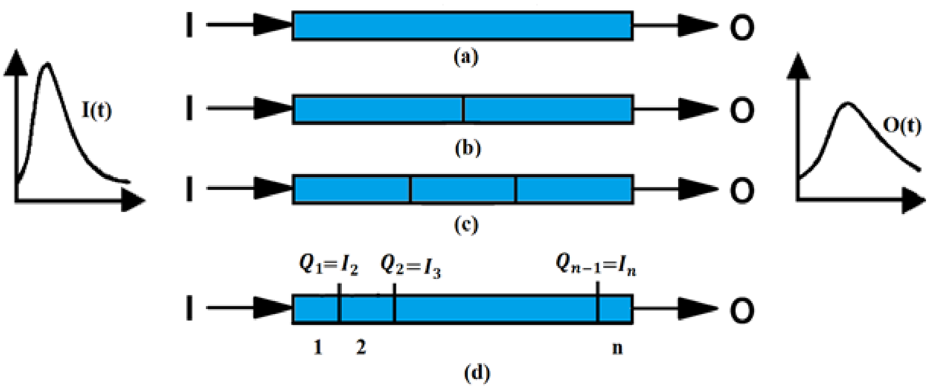

Figure 2-2- Models for distributed nonlinear Muskingum model: (a) single reach with no sub-reaches, (b) two sub-reaches within a reach, (c) three sub-reaches within a reach, and (d) multi-interval sub-reach within a reach.

where the lateral inflows varied linearly along the river reach and could be represented as a ratio of the inflow rate by considering the β parameter. *t* is the index of time between zero and the ending time of the flood. *j* is the spatial index between two and *NR+1*. The routing procedure of the distributed nonlinear Muskingum model using the Fourth order Runge-Kutta method uses the following steps:

1. Assume random values for hydrological model parameters K, x, and m, lateral flow parameter β and select one, two, three, or more reaches as NR.
2. Estimate the initial storage by using Eq. (8). Initial flow rate at the downstream section of each sub-reach is the same as the initial flow rate at the upstream section of the sub-reach.
3. Calculate the next storage. The next storage is computed by the present value plus the product of the size of the interval, Δt, and an estimated slope. The slope will be a weighted average of the following slopes using the Fourth order Runge-Kutta method:

$$L_{1}{}_{t}^{j} = -\left(\frac{1}{1-X}\right)\left(\frac{S_t^j}{K}\right)^{1/m} + \left(\frac{1+\beta}{1-X}\right) Q_t^{j-1} \qquad (2\text{-}9)$$

$$L_{2}{}_{t}^{j} = -\left(\frac{1}{1-X}\right)\left(\frac{S_t^j + 0.5 L_{1}{}_{t}^{j} \Delta t}{K}\right)^{1/m} + \left(\frac{1+\beta}{1-X}\right)\left(\frac{Q_t^{j-1} + Q_{t+1}^{j-1}}{2}\right) \qquad (2\text{-}10)$$

$$L_{3}{}_{t}^{j} = -\left(\frac{1}{1-X}\right)\left(\frac{S_t^j + 0.5 L_{2}{}_{t}^{j} \Delta t}{K}\right)^{1/m} + \left(\frac{1+\beta}{1-X}\right)\left(\frac{Q_t^{j-1} + Q_{t+1}^{j-1}}{2}\right) \qquad (2\text{-}11)$$

$$L_{4}{}_{t}^{j} = -\left(\frac{1}{1-X}\right)\left(\frac{S_t^j + L_{3}{}_{t}^{j} \Delta t}{K}\right)^{1/m} + \left(\frac{1+\beta}{1-X}\right) Q_{t+1}^{j-1} \qquad (2\text{-}12)$$

By weight averaging these four slopes, one can calculate the next storage by using the following equation:

$$S_{t+1}^{j} = S_t^j + \frac{\Delta t}{6}\left(L_{1}{}_{t}^{j} + 2L_{2}{}_{t}^{j} + 2L_{3}{}_{t}^{j} + L_{4}{}_{t}^{j}\right) \qquad (2\text{-}13)$$

1. Calculate the next outflow by using the following equation:

$$Q_{t+1}^{j} = \left(\frac{1}{1-X}\right)\left(\frac{S_{t+1}^{j}}{K}\right)^{1/m} - \left(\frac{X}{1-X}\right)(1+\beta)Q_{t+1}^{j-1} \tag{2-14}$$

1. Repeat Steps 3 and 4 for the following time intervals.
2. Repeat Steps 2 and 5 for subsequent sub-reaches.

The flowchart of the distributed nonlinear Muskingum model using the Fourth order Runge-Kutta method steps is shown in Figure 2-3.

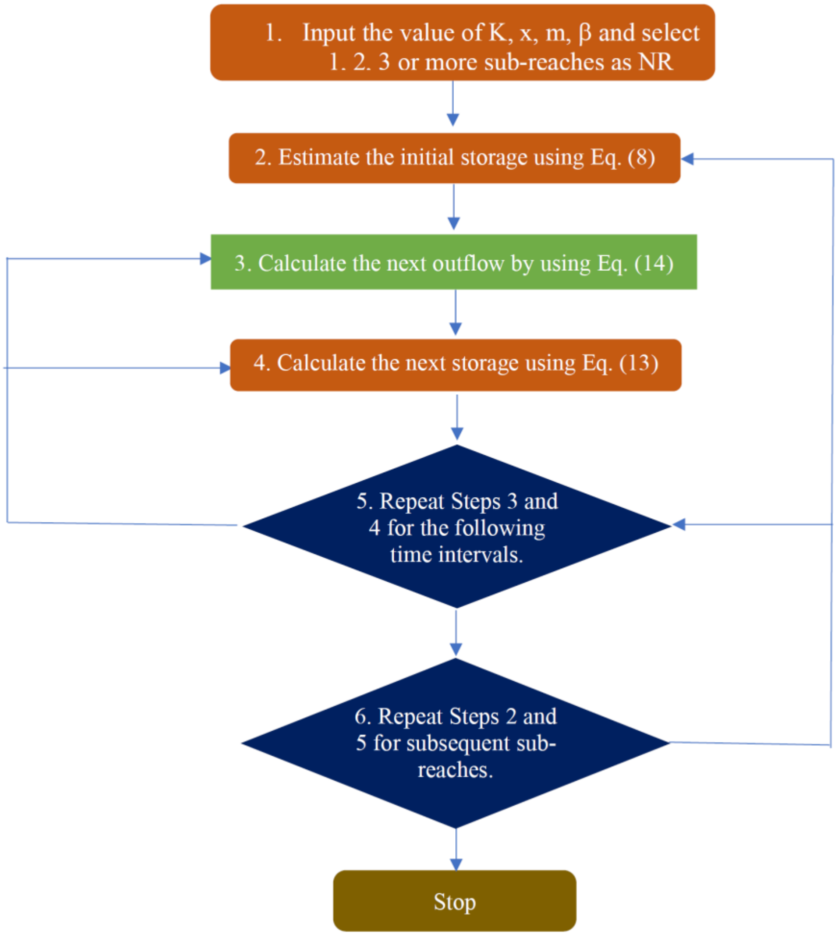

Figure 2-3- Flowchart of model steps for the distributed nonlinear Muskingum model

2.2.4. Salp Swarm Algorithm (SSA)

Salp Swarm Algorithm (SSA) is a recent swarm intelligence algorithm developed in 2017 by *Mirjalili* et. al [24] which is a population-based method. Researchers believe that the movement behavior of salp swarm is primarily aimed at improving their search for food. The position of salps is determined by multiple variables in a search space. The food source, which is the objective of the swarm, is represented by F. The leader of the swarm updates its position using a specific equation below:

$$x_j^1 = \begin{cases} F_j + c_1\big((Ub_j - lb_j)c_2 + lb_j\big) & c_3 \geq 0 \\ F_j \ - \ c_1\big((Ub_j - lb_j)c_2 + lb_j\big) & c_3 < 0 \end{cases} \tag{2-15}$$

Where x_j^1 is the position of leader in j^{th} dimension, Ub_j are the upper and lower boundary at j^{th}dimension, F_j is the food source position. The coefficient c_1 plays an important role in SSA which *balances* between exploration and exploitation. During the process of optimization, exploration refers to searching the search space thoroughly to find better solutions, while exploitation refers to utilizing the information present in the local region to improve the current solution. The parameter c_1 is gradually decreased over iterations and can be calculated using the following formula.

$$c_1=2exp^{-(\frac{4t}{L})^2} \tag{2-16}$$

Where *l* is the current iteration and *L* is the maximum number of iterations. The parameters c_2 and c_3 are random numbers generated within the interval [0,1]. $c_3$is responsible for indicating whether the next position of current leader salp should be toward +∞ or -∞. The other members of the salp swarm update their positions based on Newton's law of motion, which is expressed using the following equation:

$$x_j^i = \frac{1}{2}at^2 + v_0^t \tag{2-17}$$

Where $i \geq 2$, x_j^i is the position of the i^{th} follower in the j^{th}dimension, *t* is the time, v_0 is the initial speed, and $a = \frac{v_{final}}{v_0}$ where $v \ = \ (x - x_0)/t$.

Since the time is considered as iterations and $v_0 = 0$, Equation 2-15 can be reformulated as the equation below:

$$x_j^i = \frac{1}{2}(x_j^i + x_j^{i-1}) \tag{2-18}$$

Where $i \geq 2$, x_j^i is the position of the i^{th}follower in the j^{th} dimension.

The main steps of the SSA can be summarized as follows:

- Parameter initialization: The algorithm starts by initializing the parameters such as the population size N, number of the iterations t, and the maximum number of iterations $\max_{itr}$.
- Initial population: We generate the initial population x_i, $i = \{1, \ldots, n\}$ randomly in the range [u,l], where u and l are the upper and lower boundaries respectively.
- Individual evaluations: Every individual (solution) within the population is assessed by determining its value using the objective function, and the best overall solution is designated as F.
- Exploration and Exploitation: To balance between the exploration and the exploitation of the algorithm, the value of the parameter c_1 is updated as shown in Equation 2-16.
- Update the position of the solutions: The position of the leader solution and the other follower solutions are updated as shown in Equations 2-15 and 2-18, respectively.
- Boundary violations: Boundary violations occur when a solution goes beyond the allowable range of the search space while updating, and it is then adjusted to fall within the problem's range.
- Termination criteria: The number of iterations t is increased gradually until it reaches the maximum number of iterations $\max_{itr}$. Then the algorithm terminates the search process and produces the overall best solution found.

2.2.5. Statistical Performance Evaluation Criteria

Statistical Performance Evaluation Criteria refers to a set of metrics and measures that organizations use to evaluate the performance of their systems and processes using statistical methods. These criteria are used to quantify the performance of a system and to make decisions based on data and evidence, rather than intuition or subjective judgment. Several performance evaluation criteria were developed to compare the results of different approaches [32, 34, 39-45].

The SSE is calculated by summing the squared differences between the predicted values and the actual values for each data point. The goal is to minimize the SSE, as a lower SSE indicates that the model is a better fit for the data and predicts the observations more accurately. Muskingum storage equations are to minimize the sum of square error (SSE) between computed $\widehat{\mathrm{Q}}_{\imath}$ and observed Q_i outflows as follows:

$$SSE = \sum_{t=1}^{N}\left\{O_t - \hat{O}_t\right\}^2 \tag{2-19}$$

where Q_i and $\hat{Q}_{\imath}$ respectively are the observed and calculated outflow rates at the ith time, and *N* is the number of data.

Three performance evaluation criteria are used to evaluate and compare the models' performances.

1. SAD stands for Sum of Absolute Differences and is a statistical performance evaluation criterion commonly used to evaluate the performance of the Muskingum model. The SAD metric is used to evaluate the accuracy of the Muskingum model by comparing the estimated discharge values with the observed discharge values.

$$SAD = \sum_{t=1}^{N}\left|O_t - \hat{O}_t\right| \tag{2-20}$$

2. DPO (Deviation of Peak Observed) and DPOT (Deviation of Peak Time) are performance evaluation criteria used to evaluate the accuracy of the Muskingum model. DPO measures the deviation of the estimated peak discharge values from the observed peak discharge values. The deviation of the peak is the absolute difference between the estimated and observed peak discharge values. The formula for DPO is [39]:

$$DPO = \left|Peak_{routed} - Peak_{Observed}\right| \tag{2-21}$$

3. The formula for deviation of peak time of routed and actual outflows (DPOT) is:

$$DPOT = \frac{|T_{\mathrm{pest}} - \mathrm{T}_{\mathrm{pobs}}|}{\Delta t} \qquad (2\text{-}22)$$

T_{pobs} and T_{pest} denote the observed and estimated times to peak discharge, respectively.

All the criteria presented are measurements of the accuracy of a routing model, with the optimum value at 0.

2.3. Results of Journal Paper 1

floods can be classified based on the quantity of snow participation in the flood and the relationship between weighted discharge and storage. The contribution of snow is directly related to the amount of lateral flow, which is determined by the coefficient "β". Additionally, the value of coefficient "m" determines the link between storage and weighted discharge. The snowmelt events of this study have been categorized into three distinct categories: a, b, and c. Category “a” comprised the years 1997, 2001, 2005, 2006, 2009, 2010, and 2018. Category “b” consisted of the years 1999, 2004, and 2013, while category “c” included the years 2011 and 2019. All of the years included in the categorization process were used to calibrate the data. Specifically, year 2020 was used to validate category “a”, and year 2022 was used to validate category “b”.

Table 2-2 displays a case study of computation and optimization for a one- to three-reach problem using data category “a”.

The study model was applied to the flood data for mentioned years agreed well with the method proposed in this study. The optimal parameters of the model for the flood data were determined to be 0.54 for K, 0.24 for x, 1.38 for m, and 0.19 for β using SSA associated with single sub-reaches. Consequently, the proposed flood routing model finds 29.64 and 67.77 percent better results in terms of SSE in comparison with two and three number of sub-reaches, respectively.

Table 2-2- Hydrologic Parameters Estimates and Performance Evaluation Criteria (PEC) parameters for different numbers of sub-reaches applied for category “a”

Number of sub-reaches	Model Parameters				PEC			
	x	K	m	β	SSE	SAD	DPO	DPOT
1	**0.24**	**0.54**	**1.38**	**0.19**	**404942172.92**	**111755.01**	**2686.62**	**0**
2	0.08	0.35	1.24	0.09	524984042.89	136482.56	608.52	1
3	0.09	0.20	1.26	0.05	679360429.21	157998.12	1030.29	1

The findings for category “b” events show that NR=2 has the lowest SSE value among the different numbers of sub-reach. Notably, the value Muskingum parameters for NR=2 are K = 0.06, x = 0.06, m = 1.46, and β = 0.16. Table 2-3 shows the optimal outflows and intermediate results for flood routing.

Table 2-3- Hydrologic Parameters Estimates and Performance Evaluation Criteria (PEC) parameters for different numbers of sub-reaches applied for category “b”

Number of sub-reaches	Model Parameters				PEC			
	x	K	m	β	SSE	SAD	DPO	DPOT
1	0.12	0.08	1.60	0.39	785220033.00	192284.99	4180.37	1
2	**0.06**	**0.06**	**1.46**	**0.16**	**730213882.59**	**197004.36**	**3425.99**	**1**
3	0.02	0.05	1.37	0.10	773926769.66	205472.96	2035.31	2
4	0.00	0.04	1.29	0.07	840716718.70	211969.22	1175.80	2

The model was calibrated using observed data from years 2011 and 2019. However, no observed data was available for category "c" for validation. As a result, the model could not be validated for category "c". Table 2-4 shows the amount of parameters for different numbers of sub-reaches but since we did not have PEC analysis due to lack of validation analysis. The results of the Muskingum model show that the model is a valuable tool for simulating the routing of flood waves in rivers.

Table 2-4- Hydrologic Parameters Estimates and Performance Evaluation Criteria (PEC) parameters for different numbers of sub-reaches applied for category “c”

Number of sub-reaches	Model Parameters			
	x	K	m	β
1	0.54	1.38	0.19	1

2	0.35	1.24	0.09	2
3	0.20	1.26	0.05	3
4	0.12	1.27	0.04	4

The simulated and observed hydrographs for 2020 and 2022 are shown in Figures 2-4 and 2-5. The figures show that the trends and shapes of the hydrographs are similar. However, the peaks of the simulated hydrographs are slightly lower than the peaks of the observed hydrographs. The shape of the recession limb of the simulated hydrograph for 2020 is exactly the same as the shape of the observed hydrograph, while the simulated hydrograph for 2022 matches the observed hydrograph perfectly.

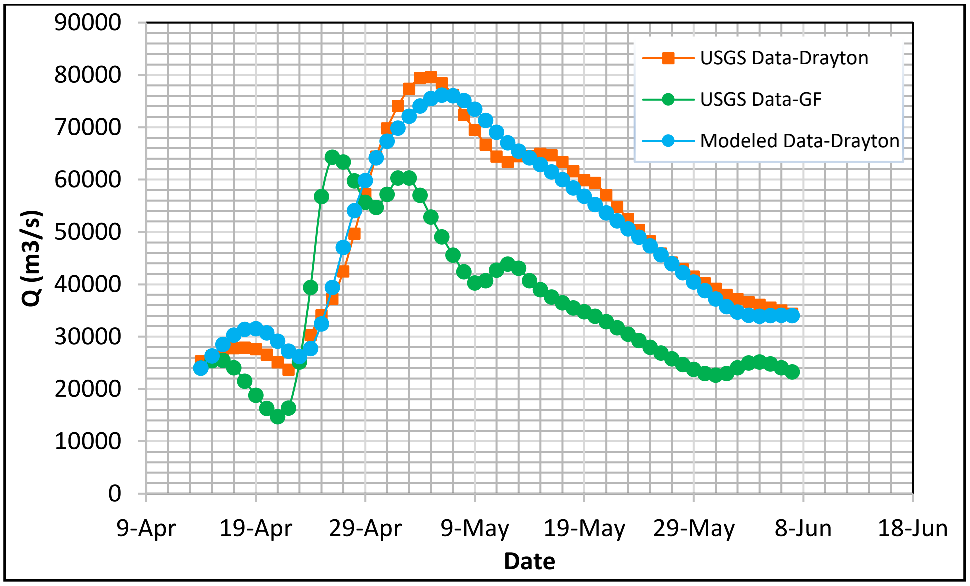

Figure 2-4- Observed and simulated hydrographs of 2020 under validation for category “a”

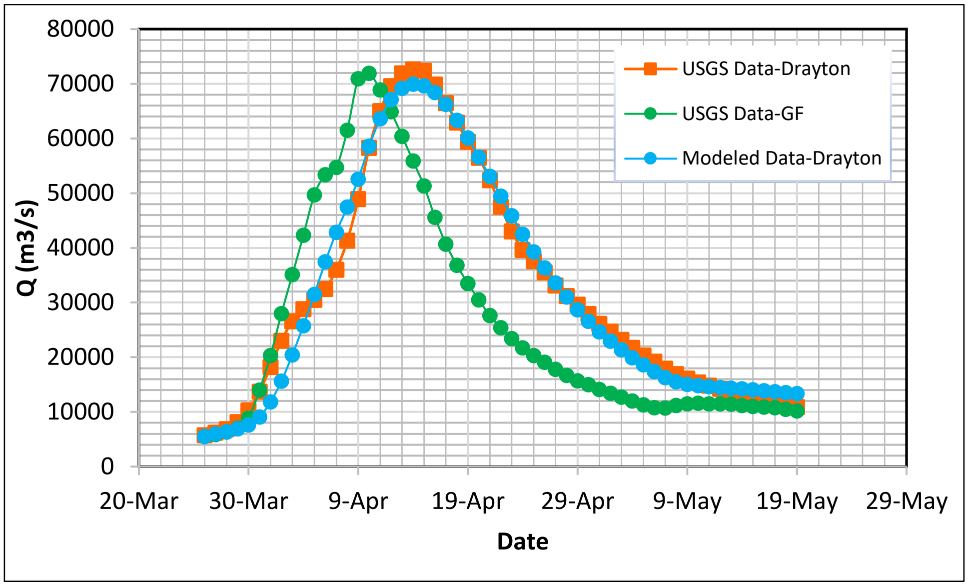

Figure 2-5- Observed and simulated hydrographs of 2022 under validation for category “b”

2.4. Conclusion of Journal Paper 1

This paper discusses the Muskingum method, a simplified approach to modeling river systems. However, including lateral inflow in the model can improve accuracy, particularly when it has a significant impact on the system's behavior. The study develops a nonlinear Muskingum model for the Grand Forks and Drayton USGS stations and estimates parameters using distributed Muskingum. The results demonstrate that the nonlinear Muskingum model accurately routes floods through the two studied USGS stations. The outcomes are as follows:

The Muskingum method is a convenient way to predict flood occurrences caused by snowmelt in icy rivers like the Red River. The Salp Swarm Algorithm (SSA) is a promising optimization algorithm that can handle the optimization of the Muskingum method. The results of the study show that NR=2 yields the optimized outflow for group “b“, whereas NR=1 produces the best results for group “a“. The optimized parameters for category “a” are x= 0.24, K=0.54, m=1.38, and β= 0.19. While for category “b”, the optimized parameters are x= 0.06, K=0.06, m=1.46, and β= 0.16. These results suggest that the Muskingum method can be effectively optimized using the SSA algorithm. The optimized parameters can be used to improve the accuracy of flood predictions in icy rivers.

3 CHAPTER 3. Flood Hydraulic Model Calibration and Scour Potential Prediction Based on Advanced ASV-Measured Extreme Flood Events Triggered by Snowmelt

3.1. Introduction and Background

The flood phenomenon is a dynamic problem. A good understanding of channel bed bathymetry and velocity field is required for flood prediction. Forecasting river and lake water flows are critical for flood warnings and water resource management. Few peer-reviewed articles specifically address flood forecasting in the Red River despite the Red River of the North's propensity for flooding. Atashi et al. [29] established effective methods that use a classical statistical method, a classical Machine learning algorithm, and a Deep Learning method. The results indicated that the LSTM approach outperformed the SARIMA and Random Forest methods in terms of prediction accuracy for three stations in the Red River: Pembina, Drayton, and Grand Forks. Lim and Voeller (2009) discussed methods for estimating flood levels in the Red River using two different techniques: L-Moment-Based Index-Flood and Bulletin 17B Procedures [1]. Their findings showed that the L-moment-based index-flood (LMIF) approach has various benefits over standard moment methods, including higher resilience and identifiability of the best-fitted distribution, which is especially important for regional research. Todhunter [46] investigated the maximum flow data for the Grand Forks, North Dakota station. Todhunter (2012) advised investigating the assumptions based on the LP3 distribution to apply the stationary frequency analysis suggested in Bulletin 17B, guidelines for Determining Flood Flow Frequency. The existence of climate cycles, the temporal independence of the records, changes in watersheds, and flood mechanisms were suggested in the Todhunter study [46]. Deschamps et al. (2002) also concluded that the Red River floodplain is not clearly defined, although it does encompass the lakebed of ancient Lake Agassiz [47].

Bathymetry and LiDAR data offer valuable insights into the topography of land and water bodies, enabling more effective flood prediction and prevention strategies. Bathymetry data provides information on the depth and shape of water bodies, aiding in flood forecasting and mitigation efforts. LiDAR data, on the other hand, can create highly detailed topographic maps of land and floodplains. Recently, the average current depth, velocity, and discharge field have been estimated using the ADCP [48-53]. These devices can generate spatially extensive velocity and discharge patterns [54-57], which could be utilized to calibrate and validate numerical models.

In this study, we provide flow measurements using an ASV called HYCAT (Figure 3-3 b) and an ADCP (Acoustic Doppler Current Profilers) [58], which measures flow discharge and velocities (Figure 3-3 a). This ASV uses GPS to navigate autonomously along preprogrammed routes on the water surface. A bathymetric survey of the streambed around the bridge sites allows us to collect water depth data as point clouds for 3-D bathymetric mapping, which is created using the HEC-RAS model. The HEC-RAS model is a valuable tool for modeling floods and identifying flood maps for 10-, 25-, 50-, and 100-year return periods [59]. Also, to gather input data on river geometry characteristics (cross sections, streamlines, river banks), several DEMs including Shuttle Radar Topography Mission (SRTM), Light Detection and Ranging (LiDAR), and Interferometric Synthetic Aperture Radar (IFSAR) were integrated into HEC-RAS [60-63].

The integration of bathymetry and LiDAR datasets can also lead to the creation of precise flood maps, which can be used to develop targeted flood prevention and mitigation strategies. By identifying at-risk communities and infrastructure and enabling precise flood forecasting, flood mapping plays a crucial role in mitigating and preventing the impact of floods.

The first part of the study used the Ras-Mapper tool in HEC-RAS to plot flood inundation mapping. Flood inundation mapping assists flood hazard management and flood extent area identification by visualizing prospective flooding scenarios, identifying locations and resources that may be in danger, and improving local response efforts during a flooding disaster [64]. Inundation mapping accuracy can be improved by using high-resolution topographic data generated by LiDAR technologies associated with ADCP bathymetry data to reveal unprecedented-level topographic features. The maps typically show the extent of flooding, including the depth and velocity of the water, and may also include information on evacuation routes, critical infrastructure, and other relevant data.

The study of Namara et al. (2022) aimed to map flood inundation using the HEC-RAS model for the Awash Bello flood plain in Ethiopia. The HEC-HMS model was used to compute annual peak flood frequency analysis for different recurrence intervals. The results showed that the whole area is under the influence of flood inundation due to intensive rainfall events [65]. Zheng et al. (2018) propose a new workflow called GeoFlood for flood inundation mapping using high-resolution terrain data. The approach involves automatic channel network extraction, computing a Height Above Nearest Drainage (HAND) raster to quantify elevation differences, and generating inundation maps using synthetic stage-discharge rating curves. The approach is evaluated in the Onion Creek Watershed in Central Texas and shows promising results in capturing general inundation patterns, with potential for informing real-time flood disaster response [66]. Pinos et al. (2019) evaluated the performance of three hydraulic 1D models (HEC-RAS, MIKE 11, and Flood Modeller) in estimating inundation water levels for a mountain river. The models were evaluated under steady-state conditions for 10 scenarios, using two types of cross-sectional data. The authors found that the models performed similarly when using detailed field survey data (type I), but the goodness of fit decreased when using cross-sections derived exclusively from DEM (type II). The authors recommend using type I geometric data for practitioners to obtain similar model performance [67].

The second part of the research was focused on assessing the scour that occurs specifically around the pier of the bridge, known as local scour. Both bathymetry and LiDAR datasets can help prevent scour near bridges by providing detailed information on the underwater topography, such as the depth of the water and the composition of the riverbed. Scouring at bridges is a highly intricate phenomenon which involves various processes such as local scour around the piers and abutments, contraction scour, channel bed degradation, channel widening, and lateral migration, which can occur simultaneously. The collective and interconnectedness of these river processes make the scouring process very complex and difficult to model mathematically. Furthermore, the presence of countermeasures such as riprap, grout bags, and gabions adds another layer of complexity to the analysis. To fully comprehend the scouring process around bridges, a thorough evaluation should account for all these factors. Engineers have been working to create and sustain bridge and hydraulic structure foundations that are secure from scouring more for than four decades. The HEC-RAS is a popular tool researchers used for analyzing bridge scour. While there are several equations available for computing scour around piers and abutments, the ones included in the HEC-RAS are widely preferred by researchers and engineers [68-70]

In accordance with the introduction, the main goals of this project are as follows: 1) to map the 2022 flood in Red River of the North in Grafton using the bathymetric and LiDAR data, 2) to evaluate local scour around the bridge pier which employs the Colorado State University method as a default equation. There was a concern for scour potential around the mentioned bridge. Flow conditions were approximated for a 2022 flood event with a 16.5 return period in the Red River of the North using HEC-RAS flow modeling software. The outcomes will enable us to understand the hydraulics and scour potential, propose remedial design options, and revisit the site for measurements after implementing the countermeasure. It is important to note that one of novelty of our study lies in the fact that we measured one of the rare flood events and due to a lack of tools and the risk involved in taking measurements during flood events, not many studies have been done on these measures in the past.

3.2. Methodology

To produce the flood inundation map and investigate scour depth around the bridge in HEC-RAS, we first constructed a hydraulic model of the river or channel using the most reliable bathymetry and Lidar data available. Subsequently, we introduced the roughness coefficient for the channel and overbanks based on previous research, as well as any other necessary parameters into the model. We executed the model to compare predicted water surface elevations and velocities with observed data. The primary data employed in this study included pier dimensions, pier shapes, flow depth, sediment samples, and river cross-section, while secondary data consisted of discharge data, topographic maps, map of the study area, and river length, all of which were entered as input data. Finally, we utilized HEC-RAS software 6.0.0 to analyze the data and determine the local scour depth around the bridge piers, and to generate the flood map of the study area.

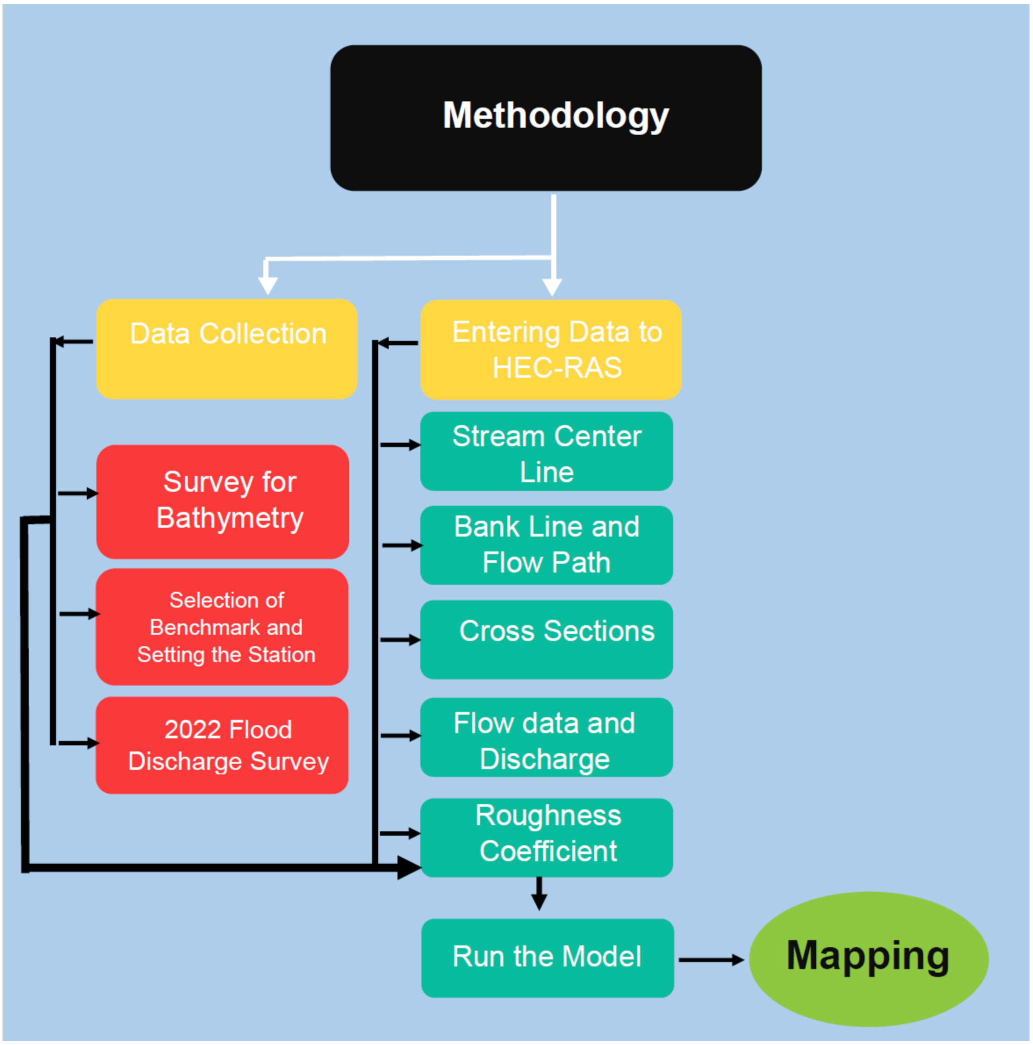

Figure 3-1- Flowchart outlining HEC RAS model development.

3.2.1. Study Area

The Red River originates near Wahpeton in North Dakota at the intersection of the Bois de Sioux and the Otter Tail rivers between the U.S. states of Minnesota and North Dakota. The river's mouth is located northeast of Winnipeg in Manitoba, Canada, flowing into Lake Winnipeg. The slope of the Red River of the North varies along its length which is 545 miles. In the region of Fargo-Halstad, the gradient of the Red River averages 5 inches per mile of length. In the region of Drayton-Pembina, however, the gradient drops to 1.5 inches per mile. The Red River of the North is considered to have a relatively gentle slope with the catchment area of 178,645 mi^2 (287,500 km^2) (Figure 3-1 a) [3]. Ice jams in the north cause major floods because of the backwater effect of the frozen water

[71]. The warmer, southern part of the Red River melts first during the spring thaw, and the meltwater flows north into colder temperatures while the northern portion of the Red River basin is still frozen, resulting in floods [1]. Rainfall in the spring and early summer, when there is still snow on the ground, relates to quick melting, and when paired with the previously described features, the Red River Valley is extremely vulnerable to floods in March and April. These factors increase the need to study flooding in this region to better identify the precursors that influence the hydrological conditions generated during spring snowmelt floods.

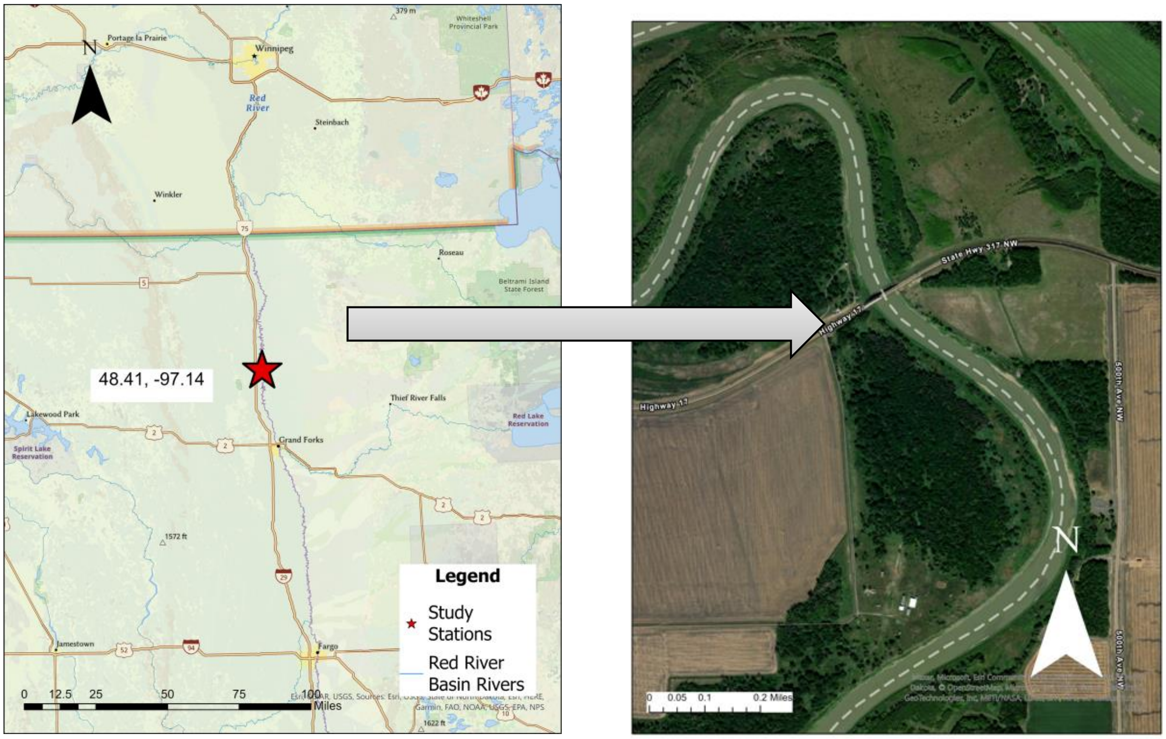

(a) (b)

Figure 3-2- a) The research location in the Red River of the North
b) Red River East of Grafton, ND (48°24'47.56"N 97° 8'15.99" W)

A section of the Red River east of Grafton, Walsh County, North Dakota (48°24'47.56"N 97° 8'15.99" W) and Marshall County, Minnesota has been chosen for this study (Figure 3-1 b). The study reach is approximately 11 miles upstream of the Drayton USGS station, No. 05092000, which is in Pembina County, North Dakota. This study location is between two USGS stations which provide discharge data: the Red River at Drayton, ND (05092000) and the Red River at Grand Forks, ND (05082500), therefore, there are no stations with discharge information for around 50 miles. Additionally, there were concerns about potential scour holes near the Red River of the North the Grafton Bridge (Bridge 5872 in Minnesota and Bridge 0017-140.372 in North Dakota) is a two-span Parker through truss that carries State Highway 17 in Walsh County, North Dakota, and Minnesota Trunk Highway 317 in Marshall County, Minnesota since the bridge scour is the primary cause of bridge failure in the United States, making the risks associated with it substantial [72].

3.2.2. Bathymetry and LiDAR Data

RiverSurveyor and HYPACK software were used to collect discharge and raw velocity and bathymetry data from the Red River, respectively. The stationary measurement instrument M9 ADCP (Figure 3-3 a) was deployed on an Autonomous Surface Vehicle (ASV), kept in position using a remote controller on the channel riverbed (Figure 3-3 b). The M9 can monitor water depth (ranging from 0.2 to 131.23 feet at velocities ranging from 0 to 65.6 ft/s), velocity, and discharge profiles [73].

Morphological changes were measured with an acoustic Doppler current profiler on peak discharge days in April, May, and June 2022. Moving boat measurements for the repeat transects perpendicular to the flow were obtained at each transect location to begin collecting bathymetry data [74, 75]. Most of the transects captured several acoustic reciprocal pairs, whereas the remaining transects contained one to three traversing passes. There was a total of 64 transects, which each transect took an average contact time of 4.5 minutes. The discharge was measured between April 2022 and June 2022, which was a flood event with a 16.5-year return period. The occurrence frequency of a specific flood event, also known as its return period, was computed using PeakFQ software obtained from the US Geological Survey [76]. The dataset used for the analysis spans from the year 1882 up to 2021 and is based on peak discharge measurements collected at the Grand Forks station. The maximum discharge based on which the return period was estimated is 63,900 cfs, which is the highest recorded discharge for Grand Forks USGS station on April 24th, 2022. The return period of a flood refers to the average number of years between occurrences of a flood of a certain size or greater. It is calculated based on the probability of the flood occurring and the frequency of occurrence. The discharge in this investigation ranged from 13,000 to 47,150 cfs. LiDAR data is commonly used to create high-resolution topographic maps and digital elevation models. In this study, the overbank's elevation was obtained from LiDAR data using the National Map of the U.S. Geological Survey with a resolution of 7.5 x 7.5 minutes to complete the cross-sections as input for the source of elevation information for flood mapping in HEC-RAS.

(a) (b)

Figure 3-3- a) RiverSurveyor/HydroSurveyor M9 ADCP unit b) ASV stationed at the Red River

3.2.3. Model Description

HEC-RAS simulates 1D hydraulic processes for a complete network of natural and man-made channels. Four 1D hydraulic components in HEC-RAS simulate water quality, moveable boundary sediment transport, steady water flow, and unsteady water flow surface profiles. The HECRAS 6.0.0 software was used in this paper to generate a 1D hydrodynamic model and determine and map the flooding of the present Red River reach. The conventional step method is used to calculate water surface profiles from one cross-section to the next by solving the energy equation iteratively. The coefficients of contraction or expansion were multiplied with the change in velocity head to determine energy losses when the channel geometry changed. The following is the energy equation [77]:

$$Z_1 + Y_1 + \frac{\alpha_1 {V_1}^2}{2g} + h_e = Z_2 + Y_2 + \frac{\alpha_2 {V_2}^2}{2g} \qquad (3\text{-}1)$$

in which:

Y_1, Y_2 = flow depth at cross sections (ft)

Z_1, Z_2 = elevation of the main channel inverts (ft)

V_1, V_2 = average velocities (ft/s)

α_1, α_2 = velocity weighting coefficients

g = gravitational acceleration (ft^2/s)

h_e = energy head loss (ft)

The empirical Energy equation, in the form of equation 3-1, was used in the model to provide the relationship between river discharge, hydraulic resistance, river geometry, and friction energy loss. The determination of total conveyance and the velocity coefficient for a cross-section requires that flow be subdivided into units for which the velocity is uniformly distributed.

Using the input cross-section *n*-value break points as the foundation for subdivision, the HEC-RAS method divides flow into main channel and the overbank regions. Manning's equation, expressed in the equation 3-2, is used to determine conveyance within each subdivision [78]:

$$Q = (1.486/\mathrm{n})\, \mathrm{A}R^{2/3}S_f^{1/2}, \qquad (3\text{-}2)$$

In the equations above:

Q = flow rate (cfs)

S_f = energy slope (ft/ft)

n = Manning's roughness coefficient

A = flow area (ft^2)

R = hydraulic radius (ft)

3.2.4. Geometric and Hydrologic Data and Data processing in the RAS-mapper tool

The bathymetry data obtained from both ADCP and LiDAR was used to prepare cross-sectional data and hydraulic structure data for river networks. Discharge and boundary conditions are provided in a steady flow file. Discharge data were established for the calculation procedure and completing the model building after geometric data entry. Six different discharges collected in the 2022 flood have been used as steady flow data to run HEC-RAS. In this study, the normal depth was used as the boundary condition for both the upstream and downstream areas. The normal depth was determined based on the slope of the study area. The defined plan is executed in a steady flow analysis when the proper data is entered into the geometry and steady flow files. Twenty 100-foot interval cross-sections were surveyed along the 2000-foot study reach, with two 40-foot interval cross-sections upstream and downstream of the bridge for greater bathymetry precision. RAS-Mapper was used to generate terrain models and display HEC-RAS data on maps by using river digitization to extract GIS data from overbank lines, centerlines, flow, and cross-section lines (Figure 3-4) [79]. In Figure 3-4, red points show channel overbanks which describe a cross-section's primary channel overbanks, the blue arrows indicate the flow path lines, and the green lines are representative of cross-sections cut lines are used to obtain the terrain's elevation data to build a ground profile spanning channel flow.

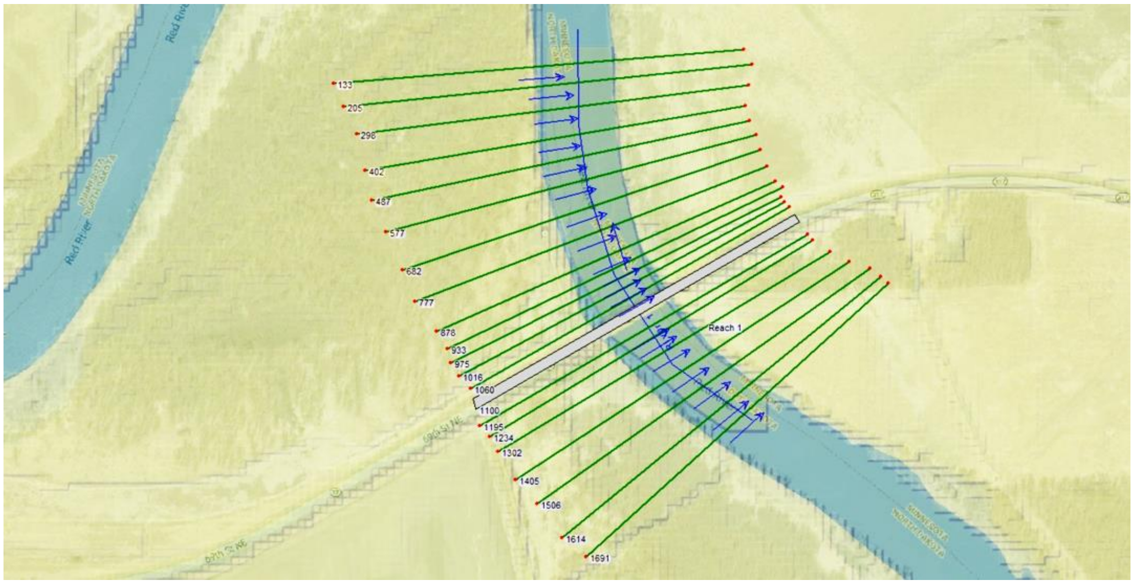

Figure 3-4- Locations of the cross-sections over the study's reach

3.2.5. Bridge Scour Modeling

The scour depth of bridge piers located on rivers can be determined by the software using hydraulic flow data, along with the shape and geometric characteristics of the bridge pier, and the composition and form of the riverbed substrate. The default model for estimating the local scour depth around bridge piers in the software is known as the CSU model, which is described as follows [69].

$$\mathrm{Y_s} = 2.0\ \mathrm{K_1K_2K_3K_4}\alpha^{0.65}\mathrm{Y_1^{0.35}Fr_1^{0.43}} \qquad (3)$$

Where: $\mathrm{Y_s}$= the maximum scour depth; α= width or diameter of the pier; $\mathrm{Y_1}$= the flow depth in the pier upstream; $\mathrm{K_1}$= the pier shape coefficient; $\mathrm{K_2}$=the coefficient of the impact angle; $\mathrm{K_3}$=the bed condition coefficient; $\mathrm{K_4}$=the bed's coefficient of reinforcement by the sediment particles; $\mathrm{Fr_1}$= Froude number.

To calculate bridge scour, one can open the Hydraulic Design Functions window and choose the scour at bridges function. This selection will prompt the program to retrieve output for the approach section, upstream section, and sections within the bridge from the output file. Input data, a graphic, and a summary results window are also available. Input data tabs can be accessed for contraction scour, pier scour, and abutment scour. When entering contraction scour data, variables other than K_1 and D_{50} can be automatically obtained from the HEC-RAS output file. When calculating contraction scour, the user needs to input only the D_{50} (average size of bed material) and water temperature to determine the K_1 factor. To enter pier scour data, the user only needs to provide the pier nose shape (K_1), the angle of attack for incoming flow, the bed condition (K_3), and the D_{95} size fraction of bed material, with all other values, obtained automatically from the HEC-RAS output file.

3.3. Results of Journal Paper 2

3.3.1. Model Manning Coefficient

An observed flow of 13,250 cfs, 47,150 cfs, 36,250 cfs, 27,700 cfs, 19,500 cfs, and 13,000 cfs at the river upstream was used from the flood event in 2022 with a 16.5-year return period. These flow rates are considered low, medium, and high flow in the Red River. In this study, we selected the value for Manning's roughness coefficient based on previous studies. The previous studies introduced ranges of Manning’s *n-coefficient* values and we evaluated these ranges using statistical parameters to determine the best *n-coefficient* value for our case study. The selected n value was then used in our hydrological analysis to improve the accuracy of flood prediction. Based on the literature review [78, 80], the initial value of *n-coefficient* was set to be between 0.04 and 0.05 for the channel bed river and between 0.06 and 0.16 for the river banks.

Table 1 presents information on water level data that was both observed and simulated for a range of discharge data collected on the 2022 flood. R-squared is a statistical measure that indicates how well a regression model fits the observed data, with higher values indicating a better fit. For statistical analysis, the R-squared for Red River bathymetry data and simulated data were calculated, and the formula is:

$$R^2 = 1 - \frac{Sum\ Squared\ Regression\ (SSR)}{Total\ Sum\ of\ Squares\ (SST)} = 1 - \frac{\sum(y_i - \hat{y}_i)^2}{\sum(y_i - \bar{y})^2} \qquad (3)$$

where:

y_i is the i^{th} water level value generated by the model,

$\hat{y}_i$ is the i^{th} water level value generated by measured data,

$\bar{y}_i$ is the mean water level value of measured data series,

n is the total number of data series.

The value of the coefficient of determination (R^2), 93%, indicates that 0.046 for the river channel, and 0.06 for the overbanks, is the best Manning's *n-coefficient* value to use because it offers an excellent match between the observed and simulated water surface profile. $n_{Channel}$ shows the value of Manning's *n-coefficient* for the main channel, and $n_{overbank}$ indicates the value of Manning's *n-coefficient for* the overbanks. Since the left overbank (LOB) and right overbank (ROB) areas have similar vegetation, so only one value used is used for both overbanks.

Table 3-1- Manning's *n-coefficient* for observed and simulated water level data

Date	Q (cfs)	Water Elev (ft)	Water Elev (Hec-RAS) (ft)
		Observed Data	$n_{channel}$=0.046 $n_{overbank}$=0.06
4/8/2022	13,250	787.00	787.24
4/27/2022	47,150	807.00	800.98
5/7/2022	36,250	805.00	799.37
5/27/2022	27,700	799.00	798.08
6/12/2022	19,500	795.00	792.11
6/20/2022	14,500	791.00	788.05

3.3.2. Model Flood Mapping

Figure 3-5 depicts the topographical surface, which comprises multiple cross-sections in the HEC-RAS model for the research area at the Red River near the Grafton Bridge (Bridge 5872 in Minnesota and Bridge 0017-140.372 in North Dakota). The 3D Viewer's multiple cross-sections visualize HEC-RAS simulation results and terrain data in three dimensions, which assists engineers when communicating hydraulic modeling results to decision-makers. The simulated inflow discharge water surface profile of 47,150 cfs and 13,000 cfs are depicted in Figure 3-5 a, and Figure 3-5 b, which are the high and low flow values of the measured data, respectively. The river flow entered the overbanks on the left overbank first due to the lower altitudes of the left overbank incorporated into the backwater phenomena when the flow gets close to the bridge or any obstacles. The term "backwater" refers to the rise in water level [81]. The bridge's pier will obstruct the flow and raise water levels upstream for subcritical flows. The entire overbank was underwater during the April 2022 Red River flood near Grafton (Figure 3-5 b).

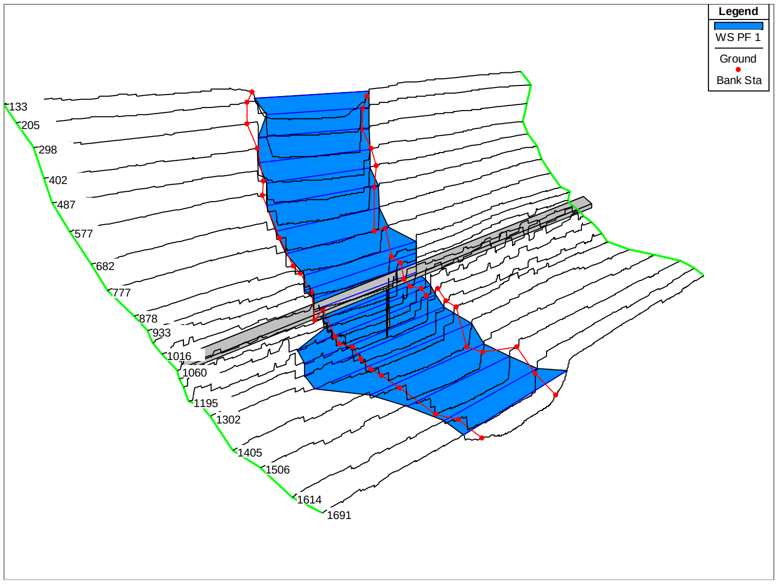

(a)

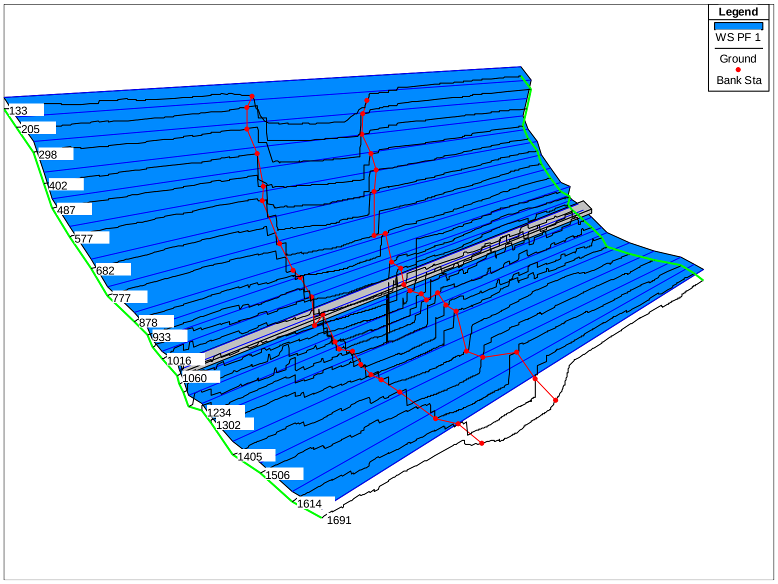

(b)

Figure 3-5- HEC-RAS simulated topographical surface profile (a) Q=13,000 cfs, and (b) Q=47,150 cfs

Figure 3-6 depicts the water levels at the first and the last cross-section (Figure 3-4) extracted from DEMs using geometry data. The ADCP bathymetry and LiDAR data could be combined into a single point cloud because the ADCP incorporated with ASV used in this study is a sensor platform capable of using data from multiple sources. A broad framework of standard specifications, practices, and guidelines is also necessary to enable multiple groups to consistently contribute well-described LiDAR and integrated digital elevation models (DEMs) to the development of an elevation in the river area. The National Geophysical Data Center (NOAA) and the USGS Earth Resources Observation & Science Center collaborated to create this framework to provide a single national representation of bathymetry and topography in the United States. Combining these two sets of information in the Ras Mapper's terrain-making capability enables the creation of a single, continuous surface from several tiles that are all registered, have the same cell resolution, and are edge matched. This option can use many LiDAR tiles that line up.

The simulation results indicate that cross-section No. 133, the last designed cross-section, is less impacted by the flood, whereas cross-section No. 1691, located upstream of the bridge, is more susceptible to flooding at low flow discharge conditions, which is 13,000 cfs (Figure 3-6 a and b). The water level for cross-sections No. 133 and No. 1691 is 788.14 ft and 789.00 ft, respectively. The existence of bridge piers or abutments in the streams will affect the stream flow and riverbed locally, causing the water to flow faster, the bridge to scour, and potentially jeopardizing the structure. A faster cross-section would have less depth when the discharge is the same, according to the continuity equation.

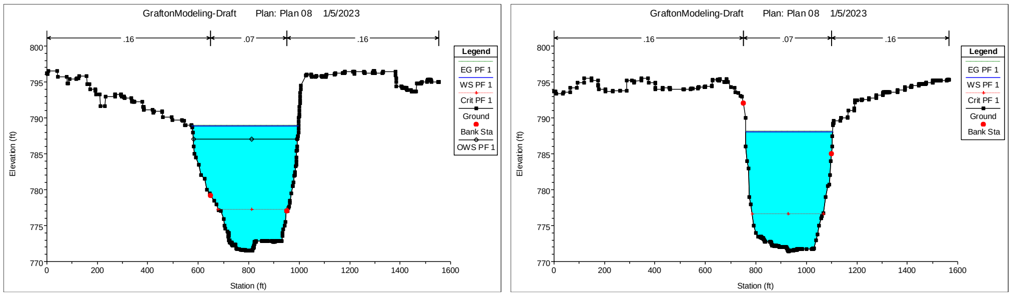

(a) Cross-section No. 1691 (b) Cross-section No. 133

Figure 3-6- Water depths at the Upstream and Downstream Cross-sections

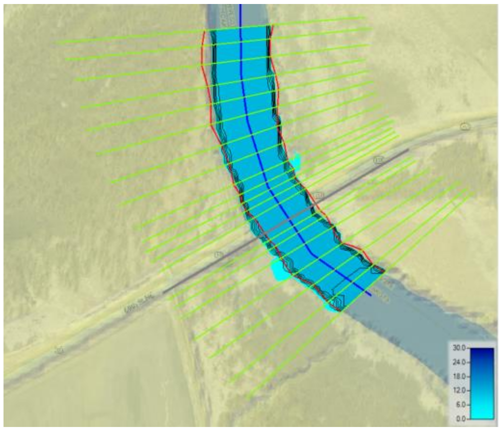

Q=13,000 cfs

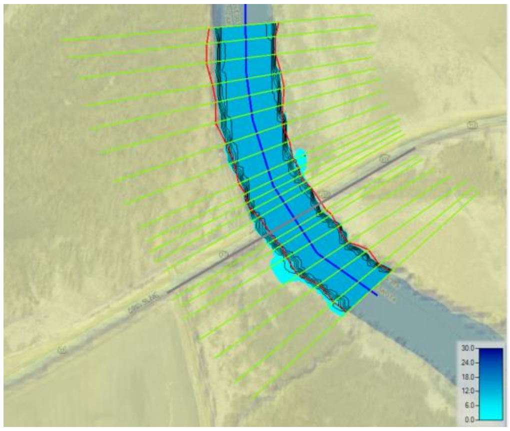

Q=14,500 cfs

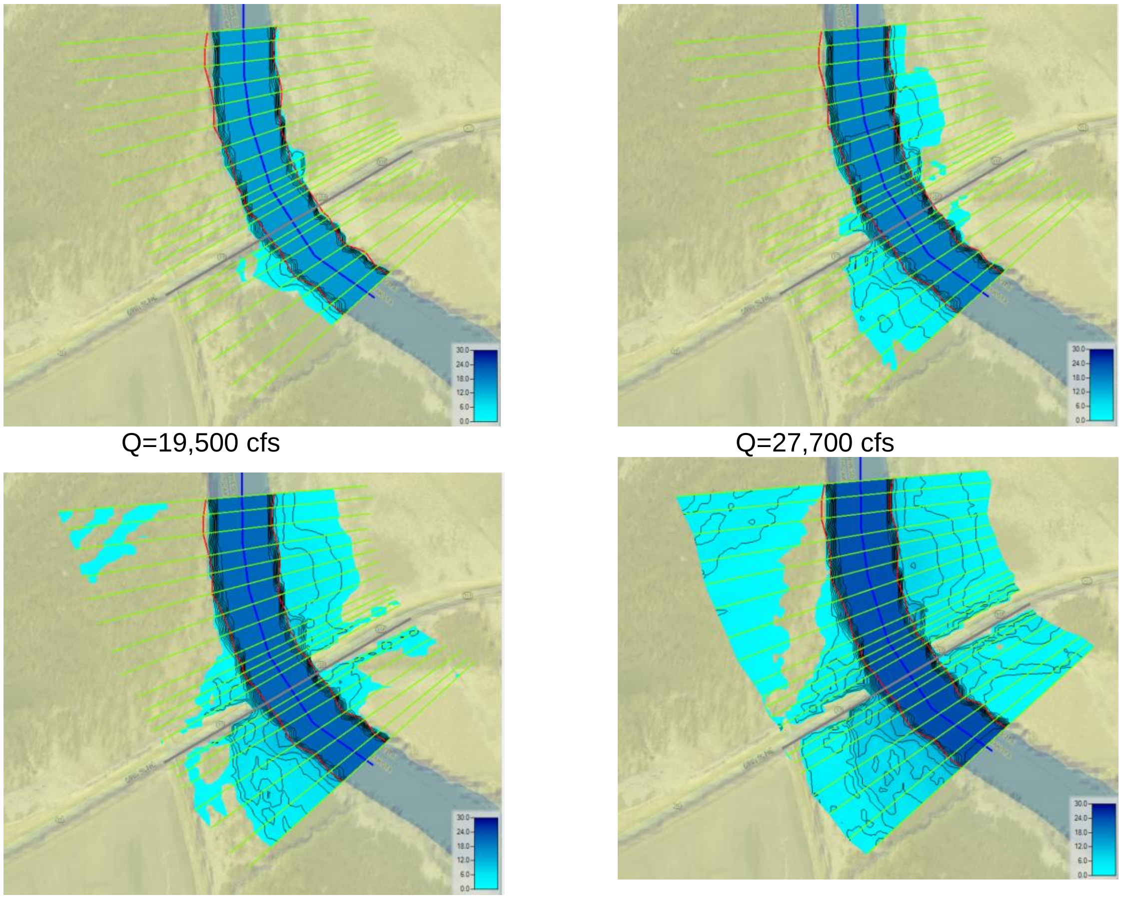

Q=19,500 cfs

Q=27,700 cfs

Q=36,125 cfs

Q=47,150 cfs

Figure 3-7- Simulated flood inundation map of Red River near Grafton from April 2022 to June 2022 flood event for different discharges

The flood map presented in Figure 3-7 illustrates the depth changes at each cross-section with a steady flow simulation, where dark blue denotes deeper depths, and light blue denotes lower depths. The simulated flood maps illustrate the variance in water depths along the channel in terms of color. All discharges were measured for six time periods, from April 2022 to June 2022, and the highest flow was on April 27th at the Red River study location. The current study's results indicate that the corresponding discharge was between 13,000 cfs and 47,150 cfs from April 2022 to June 2022. Downstream cross-sections, which were located downstream from the bridge, had a shallower depth during peak discharge conditions, and the upstream cross-sections were more affected by the flood (Figure 3-7 a and b). The results indicate that a substantial change in water flow of 34,150 cfs resulted in a significant difference in flooding extent. The flood inundation extent determined using the HEC-RAS model varied substantially with slight changes in water depth because the Red River has a flat landscape.

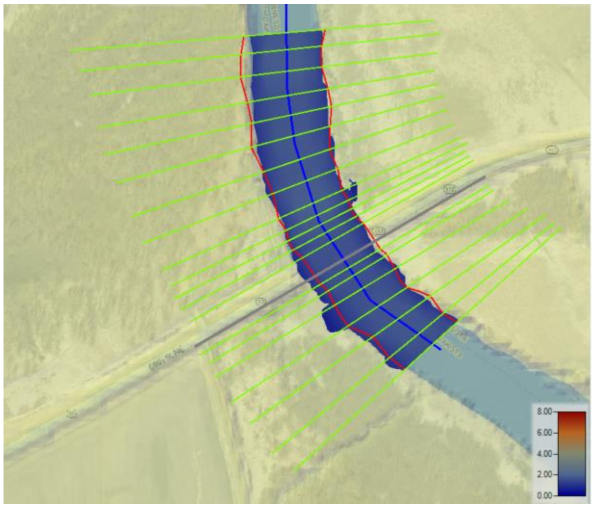

Q=13,000 cfs

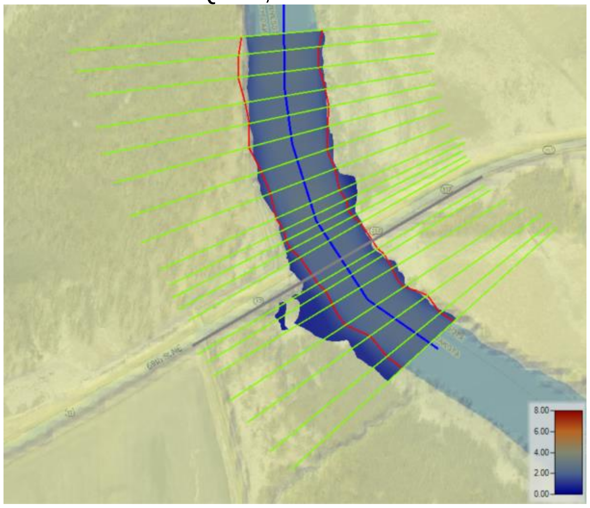

Q=19,500 cfs

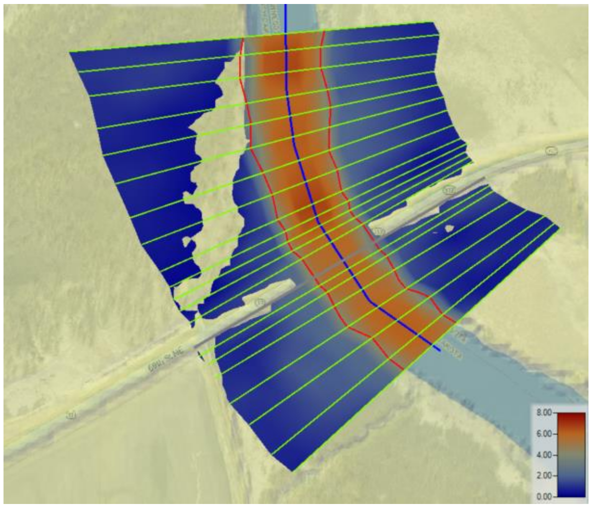

Q=47,150 cfs

Figure 3-8- Simulated velocity distribution for Q= 13,000 cfs, 19,500 cfs, and 47,150 cfs (base map from google earth [82]).

Figure 3-8 illustrates the simulation results of the velocity distribution for Q= 13,000 cfs, 19,500 cfs, and 47,150 cfs. These velocity mapping effects will help prevent erosion in the river overbanks and around bridge piers. The results from all three scenarios, which are low, medium, and high flow in the 2022 flood event, indicate that the flow velocity near the right side of the river overbank after the bridge location had higher values; therefore, protection may be required on this side of the river overbank. Furthermore, a high-velocity counter line, which is eddy flow, can be observed at all three discharges after bridge pier cross-section No. 933 (Figure 3-4) in the river's center. The existence of piers can cause the formation of eddies, which are circular currents that can change the flow patterns and speed of the water downstream of the pier. This fast-moving eddy flow becomes larger at higher velocities after the bridge pier, which could increase scour after the bridge pier. The maximum recorded velocity in the study area was 1.85 ft/s, 2.79 ft/s, and 6.75 ft/s for discharge values of 13,000 cfs, 19,500 cfs, and 47,700 cfs, respectively, after cross-section No. 933 (Figure 3-4).

3.3.3. Model Scour Bridge

In this project, hydraulic analysis was conducted using the HEC-RAS 6.0.0 software, which uses a steady flow simulation. The study aimed to predict local scour depth around an existing bridge, specifically caused by contraction scour and piers with square nose shapes. Most of the data required for calculating contraction scour was generated automatically by the HEC-RAS program, based on the steady flow analysis. The remaining data, including sediment diameter (D_{50}) on each left and right overbank and channel, were entered manually. The HEC-RAS program automatically calculated the coefficient K_1 using the available D_{50} field measurements. Finally, the program analyzed the contraction scour depth around the piers using the CSU equation. Then the modeling of local contraction scour depth with HEC-RAS 6.0.0 can be seen in Figure 3-9.

Figure 3-9 shows the relationship between contraction scour depth (Y_s) and the Froude number (F_r) on the existing bridge concerning discharge increasing. There is a rise in Froude number between Q=19,500 cfs and Q=36,250 cfs. The contraction scour depth and the Froude’s number increase further for the Q=13,000 cfs to Q=14,500 cfs of as the water level overtopped to the deck of the bridge. For the discharge of 47,150 cfs the water level reaches the deck of the bridge and due to this contraction scour depth increases whereas Froude’s number decreases.

When the discharge increases in a river, the velocity of the water also increases, which leads to a higher Froude number. This is because the inertial forces become relatively more significant as the velocity increases. However, as the water reaches the deck, the depth of the water decreases, and the gravitational forces become more important. This causes a decrease in the Froude number, even though the velocity may still be high.

As water flows towards a bridge, the channel or riverbed in which it is flowing becomes constricted due to the presence of the bridge piers or abutments. This narrowing of the channel causes an increase in the velocity of the water as it passes through the bridge opening and the cross-sectional area of the channel must decrease to maintain the same mass flow rate. Therefore, as the water passes through the bridge opening, the depth of the water decreases. This can lead to a concentrated flow of water around the piers or abutments, which can increase the potential for erosion and scour around the bridge foundations. On the other hand, the contraction scour depth continues to increase even after the Froude number has decreased. This is because the velocity of the water is still high, and it can still cause erosion of the riverbed, leading to deeper contraction scour depths.

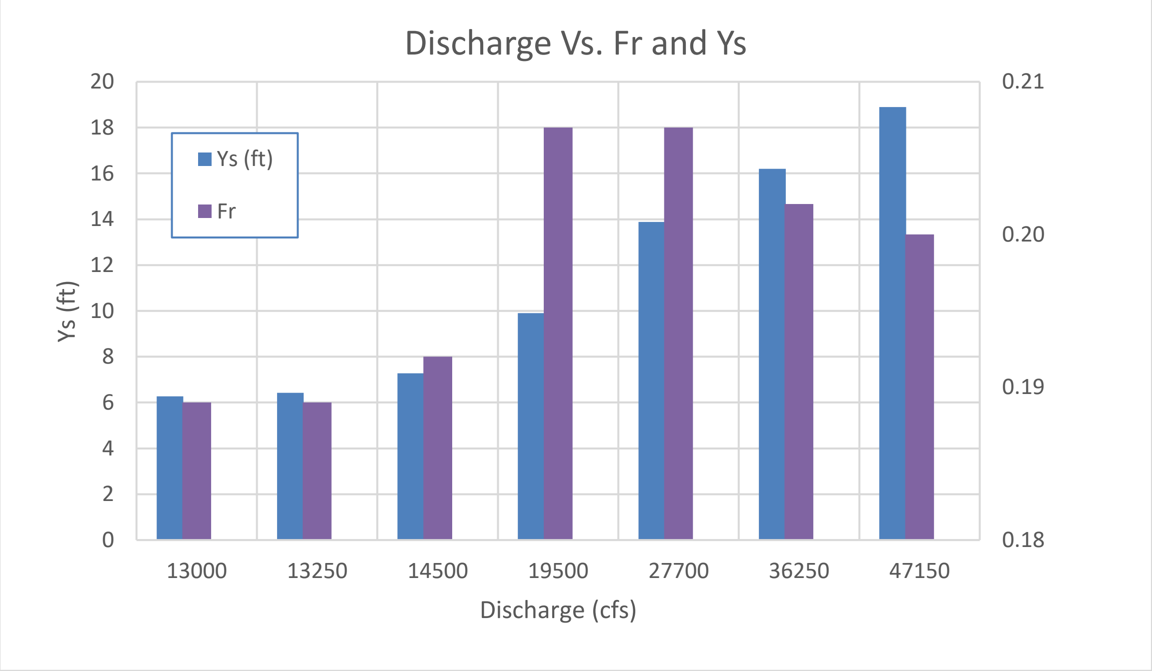

Figure 3-9- Discharge Vs. Froude number and contraction scour Depth

3.4. Conclusion of Jornal Paper 2

Our measurement of one of the most extreme flood occurrences in this paper's invention allowed us to validate the accuracy of the HEC-RAS model's flood predictions and evaluate the model's performance under extreme flood events. By using geospatial techniques, we were able to enhance the accuracy of the model's flood mapping by incorporating topographic data and other relevant information. This study's findings can contribute to better flood management and emergency response planning in the study area and other regions facing similar flood events.

The study aims to determine the best value for the Manning coefficient to improve the accuracy of flood prediction in the Red River. The selected value for Manning's roughness coefficient was based on previous studies, and statistical analysis was performed to determine the best value for the case study. The value of the coefficient of determination (R_2), which was 93%, indicates that 0.046 for the river channel and 0.06 for the overbanks is the best Manning's n-coefficient value to use.

The bathymetry data were collected using ADCP and ASV combined with LiDAR data to determine the flow for a flood event in 2022, and the flood mapping was generated using HEC-RAS modeling. Flood inundation mapping indicates that an eddy flow occurs immediately after the bridge and becomes relatively larger with an increase in flow discharge and velocity. The results showed good agreement between the methodologies, indicating the potential of using ADCPs incorporated with ASV and LiDAR data together for flood inundation mapping studies due to the advantages of integrating bathymetry, flow velocity, and discharge flood data.

The study also showed that as discharge increases, Froude number and contraction scour depth increase, but as water level reached the deck of the bridge, the Froude number decreases while contraction scour depth continues to increase due to high velocity. Narrowing the channel by bridge piers can lead to concentrated flow and increase scour potential.

4 CHAPTER 4. Water Level Forecasting Using Deep Learning Time Series Analysis in Red River of The North

4.1. Introduction and Background

Machine learning has become a popular tool in many fields, including environmental science, where it is being used to predict and manage natural disasters. In recent years, the Red River has experienced several devastating floods that have caused significant damage to the surrounding communities. As a result, researchers are exploring new approaches to flood prediction, including the use of machine learning algorithms. By analyzing historical data on weather patterns, river levels, and other factors, these algorithms can identify patterns and make accurate predictions about the likelihood of a future flood. In this chapter, we used Machine Leaning approaches to improve flood prediction in the Red River of the North.

Forecasting water levels in rivers and lakes are essential for flood warnings and water resource management. Hydrological stations provide water level data in a time series format, which requires researchers to use time series hydrological prediction models for forecasting future data. The combination of classical statistical methods and Machine Learning (ML) algorithms has significantly contributed to the development of data-driven forecasting systems, which offer cost-effective solutions and improved performance in simulating complex physical processes of floods. By analyzing historical data, these methods can make predictions about future flood events, analyze patterns, and evaluate flood management strategies.

In general, there are three methods for forecasting streamflow. The first approach mainly depends on physically-based models [83] that have long been used to forecast hydrological events, including storms [84, 85], runoff or rainfall [86, 87], shallow streamflow [88], hydraulic models [89, 90], and more cases of global circulation [91], encompassing the interaction between atmosphere, water, and floods [92]. While physical models can forecast various flooding scenarios, they usually depend on several hydro-geomorphological monitoring datasets, which can be expensive to acquire and process, and this also makes short-term predictions difficult [93]. In addition, creating physically-based models often requires a deep understanding and expertise in hydrological factors, which has been identified as a difficult task [94]. Furthermore, many types of research demonstrate that there is a gap in the short-term prediction capability of physical models [92].

The second approach involves using mathematical models to simulate the hydrodynamics of streamflow. This approach is widely adopted in many countries due to its basis on fundamental hydrologic and hydraulic principles. Flood modeling studies have utilized physically-based hydrologic models such as the hydrologic engineering center-hydrologic modeling system (HEC-HMS) [95], soil and water assessment tool (SWAT) [96], IHACRES [97], and HSPF model [98] have been engaged in flood modeling studies. However, using these models necessitates substantial field observations and trial and error parameters [99]. They still only supply at-site flood risk estimates based on local streamflow data obtained at gauging hydrometric stations, making them inappropriate for regional flood assessment [100, 101].

The final approach is based on data and uses statistical relationships between input and output data to predict near-future outcomes. One of the most commonly used frameworks in this data-driven method is the Machine Learning (ML) model, which has been employed in flood forecasting since the 1990s. Unlike physically-based numerical models, ML models do not require explicit knowledge of nonlinear dynamic processes, making them a potent tool for flood prediction [102].

Numerous research has been conducted to predict the water levels in rivers, lakes, and other water bodies worldwide using different time series models. The Autoregressive Integrated Moving Average (ARIMA) model is widely used for river discharge and flood forecasting [103-109]. Yürekli et al. presented a monthly streamflow forecasting method for three gauging stations in the north Anatolia fault line and evaluated the residuals of the ARIMA model [103]. The authors state that a comparison of monthly mean and standard deviation for observed and anticipated data using the ARIMA model reveals that the anticipated values maintained the main statistical features of the observed data. By comparing the observed and anticipated monthly data sequences using linear regression, they discovered a statistically significant linear relationship between the observed and anticipated monthly data. In another study by [104], data from two Schuylkill River stations in Berne and Philadelphia were collected over six years. The author demonstrated that daily data have no seasonality; therefore, there was no seasonality in the proposed ARIMA formulation. Even though both stations are located along the same river, the proposed ARIMA models provided for each station differed due to the differing watershed coverage. Exponential Smoothing was employed by [110] to study and predict water level trends in the Mtera dam in Tanzania. They discovered that the water level in the Mtera dam has been declining over time, and the highest and lowest water levels were both showing a declining trend in recent years. Additionally, estimates for the next five years based on Exponential Smoothing of time series data revealed that the water level would be below the lowest water level required for energy production in the spring of 2023. The authors evaluate the efficiency and the accuracy of several models for predicting Tanshui River water levels in Taiwan during 50 historical typhoon events that occurred over 11 years between 1996 and 2007. The authors compared three eagers models, including artificial neural network (ANN), linear regression (REG), and support vector regression (SVR), with two lazy models, including locally weighted regression (LWR) and the k-nearest neighbor (kNN). According to the results, ANN and SVR outperformed REG among eager learning models. However, the authors state that although ANN, SVR, and REG were considered eager learning models, their prediction capabilities differed due to different learning optimizers. In their results, among lazy learning models, LWR outperformed kNN, and both lazy models showed more accurate predictions than REG eager model.

Our objective is to utilize three models: SARIMA (a conventional statistical model), RF (a classical ML algorithm), and LSTM (a Deep Learning method) to create a flood susceptibility map and recognize flood hazard regions in the Red River of the North. No prior research has explicitly employed a classical statistical method, a classical ML algorithm, and a state-of-the-art Deep Learning method to improve flood forecasting for the Red River of the North. The findings from this study will support regional and local authorities as well as policymakers in mitigating flood risks and developing effective measures to minimize potential damages.

To forecast the water level, we utilize data collected at three United States Geological Survey (USGS) stations in the Red River of the North (Pembina, Drayton, and Grand Forks), sampled hourly from 2007 to 2019. We forecast the water level six hours, twelve hours, one day, three days, and one week in advance at the Red River of the North. Pembina is the downstream forecasting location, but it only has a water level station. However, Drayton and Grand Forks have full discharge measurement stations that provide water level and discharge series.

4.2. Methodology

4.2.1. Study Area

The Red River of the North was selected for several reasons. Firstly, its river network has few minor flow-control structures, making it suitable for ML flood prediction techniques. Secondly, it presents a challenge for using satellite altimetry to estimate the stage due to its narrow main stem channel. Thirdly, there are established USGS gaging stations along the main tributaries for field-based estimates of river flow and stage verification. Finally, the river basin's hydrologic response to climatic variability has not been extensively modeled, despite typical devastating property losses in years with substantial snow accumulations. However, among the three selected stations, the downstream Pembina station lacks data for river flow discharge. Water level data from USGS stations at Pembina, Drayton, and Grand Forks sampled hourly from 2007 to 2019 are used to forecast the water level for different time intervals in advance at the Red River of the North. Drayton and Grand Forks have full discharge measurement stations, while Pembina only has a water level station. A map in Figure 4-1 shows the locations of these three stations.

Figure 4-1- Location of USGS stations on Red River in Pembina, Drayton, and Grand Forks.

4.2.2. Data representation and pre-processing

Table 4-1 summarizes the characteristics of the three datasets used in this study and Figures 4-2 and 4-3 preset monthly and annual water level data for the selected stations, respectively. The water level data were collected from USGS mean daily gauge height for the period November 1, 2007, to December 31, 2019. To prepare the data for time series forecasting algorithms, it was resampled and pre-processed to have equal time intervals of hourly sampling. Missing data were identified as periods of non-sampling or days without data when the data sampling was less than 8 times per day. Linear interpolation was used to fill in missing data for periods with more than 8 samples per day but with some missing hourly data.

Table 4-1- Characteristics of the water level time series at three hydrology stations of the Red River

Station No.	Station Name	Period	No. of Samples	Frequency
1	Pembina	2007-2019	104616	Hourly
2	Drayton	2007-2019	100140	Hourly
3	Grand Forks	2007-2019	105117	Hourly

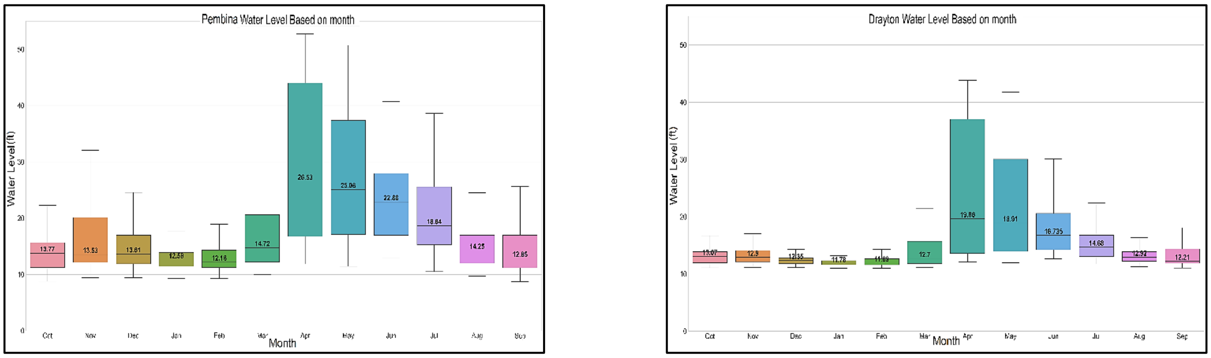

(a) (b)

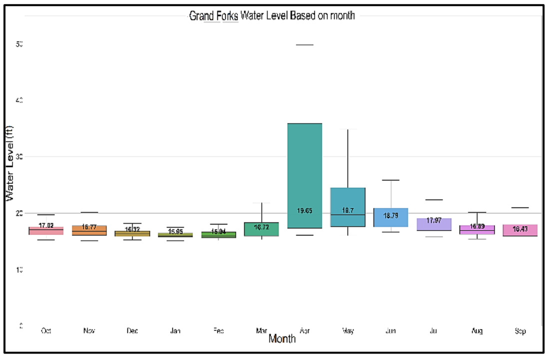

(c)

Figure 4-2- Monthly water level at three hydrology stations of Red River of the North (a) Pembina, (b) Drayton, and (c) Grand Forks stations

The main source of water in south-central Manitoba is the Pembina River, a tributary of the Red River of the North. The Pembina River runs southeast from the highlands of the Turtle Mountains, commencing at its highest point (elevation 2000 feet). It flows west into the Red River in Pembina, North Dakota, about 2 miles south of the US-Canadian border. A stream gauge near Pembina measures the height of the water flowing down the Red River. The sensor, one of around 8,000 maintained by the USGS, serves as a sentinel for towns along the river that were flooded in 2009, 2010, and 2011. The Pembina gauge was targeted mainly for flood prediction because of two main reasons: First, this station is the last station on the Red River before it flows into Canada, and second, two upstream stations, Drayton and Grand Forks, have discharge information in USGS, but Pembina station, as the downstream station, does not have any discharge information.

According to Figure 4-2, the Pembina station records the highest streamflow in April, with an average water level of 26.53 feet, and the maximum water level recorded was 52.71 feet on April 15, 2009. On the other hand, the Drayton station has been recording streamflow records continuously since 1942, and specific-conductance measurements have been taken since 1970 at both Drayton and Emerson stations, approximately once a month, whenever discharge measurements were obtained. This long-term data has allowed for the examination of trends in streamflow and water quality. The USGS crew obtained streamflow measurements under ice conditions on the Red River at Drayton on January 21, 1986 [22]. As shown in Figure 4-2, April is also the month with the highest streamflow at the Drayton station, with an average water level of 19.66 feet, and the maximum water level recorded during the study period was 43.82 feet on April 6, 2009. Additionally, Figure 4-2 indicates that May is the month with the second-highest streamflow for both the Pembina and Drayton stations, with an average water level of 25.08 feet and 18.91 feet, respectively.

The US Army Corps of Engineers established the upstream gage station on the Red River of the North at Grand Forks in 1882. On May 26, 1901, Charles M. Hall, a geology professor at North Dakota Agricultural College, installed an additional station above the original stream gauge. Hall's main purpose was to explore the possibility of storing Red River floodwaters for hydropower, irrigation, and domestic supply needs [23]. Today, this stream gauge has a continuous record of stream gauge height, discharge, stream velocity, and water quality parameters, as well as real-time web data. According to Figure 4-2, May is the month with the highest flow recorded at the Grand Forks station, which has an average water level of 19.70 feet. On April 06, 2009, the maximum water level during the time of this study was recorded, with an average water level of 49.84 feet.

Frequent flooding has been a concern for the Red River of the North in Grand Forks, ND, most notably the major floods of 1882, 1897, 1950, 1996, 1997, 2006, 2009, and 2011, which is why Grand Forks stream gage data is critical to flood protection for the cities of Grand Forks, ND and East Grand Forks, MN.

Figure 4-3 depicts the annual box and whisker plot of water level data from three Red River of the North hydrology stations. In 2019, the maximum annual average of water level data for all three stations was 21.54, 16.05, and 18.84 feet for the Pembina, Drayton, and Grand Forks stations, respectively.

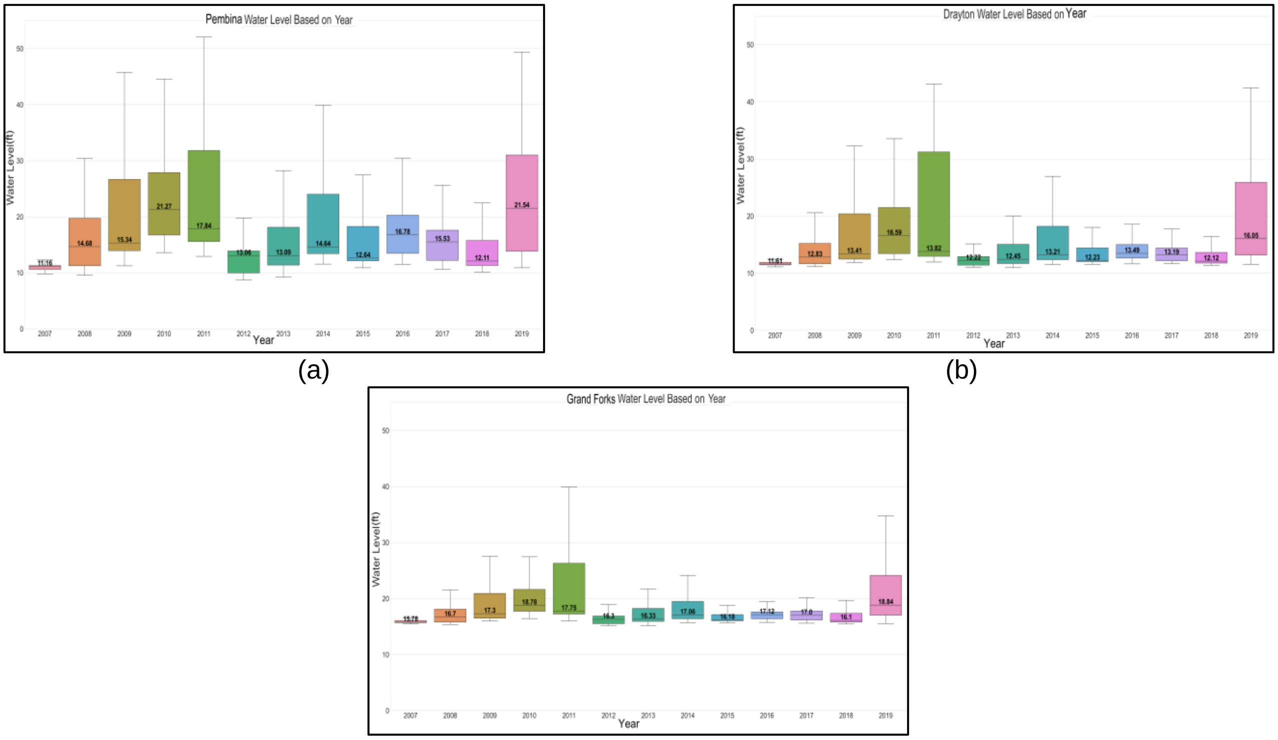

(a) (b)

(c)

Figure 4-3- Box and whisker plot of water level data at three hydrology stations of Red River of the North (a) Pembina, (b) Drayton, and (c) Grand Forks stations

Inspired by the success of the Autoregressive Integrated Moving Average (ARIMA) model [86, 92, 93], we propose Seasonal Autoregressive Integrated Moving Average (SARIMA) method to individually capture the components of the time series. This approach is tested on real Red River datasets for hourly water level predictions. Linear statistical models, such as SARIMA, may not be ideal for representing nonlinear interactions in time series, but they are adequate for modeling the linear component [111].

Meanwhile, non-parametric statistical ML models, such as long short-term memory (LSTM), can model any nonlinear components (universal approximators). Furthermore, for the last method, RF was selected due to its popular use as an ML algorithm in hydrology applications [112-114]. All these three selected methods are discussed in the following section.

4.2.3. Seasonal Autoregressive Integrated Moving Average (SARIMA)

SARIMA, or Seasonal Autoregressive Integrated Moving Average, is an extension of ARIMA, which stands for Autoregressive Integrated Moving Average. ARIMA combines differencing with AR (Autoregressive) and MA (Moving Average). This means that in ARIMA, "AR" indicates the relationship between a variable in time-series data and its own lagged values, "I" represents the differencing of an observation's value from its previous values to create stationary time-series data, and "MA" denotes the linear combination of observations and errors from previous observations. ARIMA is referred to as non-seasonal ARIMA and is not suitable when time-series data includes seasonal components. Therefore, a modified version of ARIMA called Seasonal ARIMA, or SARIMA for short, was introduced by adding seasonal terms. The ARIMA (p, d, q) can be represented mathematically b the following formulas:

$$Y_t = (1 - l)^d X_t \tag{4-1}$$

$$(1 - \sum_{i=1}^{p} \phi_i \, l^i) Y_t = (1 + \sum_{i=1}^{q} \theta_i l^i) \, \varepsilon_t \tag{4-2}$$

where l represents a lag operator; p and q are the orders of autoregressive and moving average parts, respectively, and d is the degree of difference. SARIMA can be written as $ARIMA(p, d, q)(P, D, Q)_s$ where P, D, Q are the seasonal terms of p, d, q, and s is the number of observations per year.

4.2.4. Random Forest

The Random Forest (RF) model is a supervised machine learning algorithm that uses an ensemble of decorrelated decision trees to make predictions. A decision tree is a model that relates the output to explanatory variables or attributes, and each tree has a set of nodes that are devoted to a dataset. These trees are grown from random resampled training batches selected from the original data to make them orthogonal. For regression applications, multiple decision trees provide independent numerical predictions of the target variable, while for classification, they predict class labels. The outcome of the RF model is the average prediction of all the individual trees. The purpose of RF is to identify the spatial relationships between flood occurrences and the associated characteristics for classification and regression tasks. The RF was selected due to its simplicity; tuning a few parameters can result evaluates accuracy more than other ML models [115]. In this research, we evaluate python's scikit-learn package. The systemization of the RF algorithm's importance function is briefly described as follows: The system selects a set of independent values to make an impact on each tree response which is a subset of the predictor values of the initial dataset. The optimal subset of predictor variables is calculated using: $log_2^{(M+1)}$, where M is the input. Now we can calculate the mean-square error (RMSE) for an RF from

$$\varepsilon = \left(v_{observed} - v_{response}\right)^2 \qquad (4\text{-}3)$$

where ε, $v_{observed}$, and $v_{response}$ are mse, variables from observed and result respectively. Also, we can calculate the trees average prediction.

$$S = \frac{1}{t}\sum t^{th}\, v_{response} \qquad (4\text{-}4)$$

where S and t are RF prediction, and the number of trees in the forest, respectively. In classification, after defining a set of random trees and prediction, the algorithm compares the number of excess votes to other classes' average votes. Although a predictor set is randomly chosen for each tree from the equal distribution in the regression algorithm, each tree can add a numerical value response to form the RFs.

4.2.5. Long short-term memory (LSTM)

In this study, we utilized another Deep Learning technique called the long short-term memory (LSTM) network, which is similar to the recurrent neural network (RNN). RNNs are designed to apply input data sequentially over extended periods. It performs the same task for all elements in the series, and the output is dependent on the previous computations. Specifically, RNNs contain a memory cell that stores data until the training data sequence is completed. RNNs are suitable for non-linear time series problems, but they encounter gradient issues when training with long time lags, which are necessary for predicting time series or hydrology. Therefore, LSTM networks were employed, which are a type of RNN that can overcome the gradient problem by using gates to control the information flow within the network [32]. LSTM is developed to build a robust many-to-one model for hydrological time series similar to RNN memory cells structure of the input, self-recurrent connection, forget, and output gates [33]. Assume the i_t, o_t , f_t are input, output, and forget gate at the time of t.

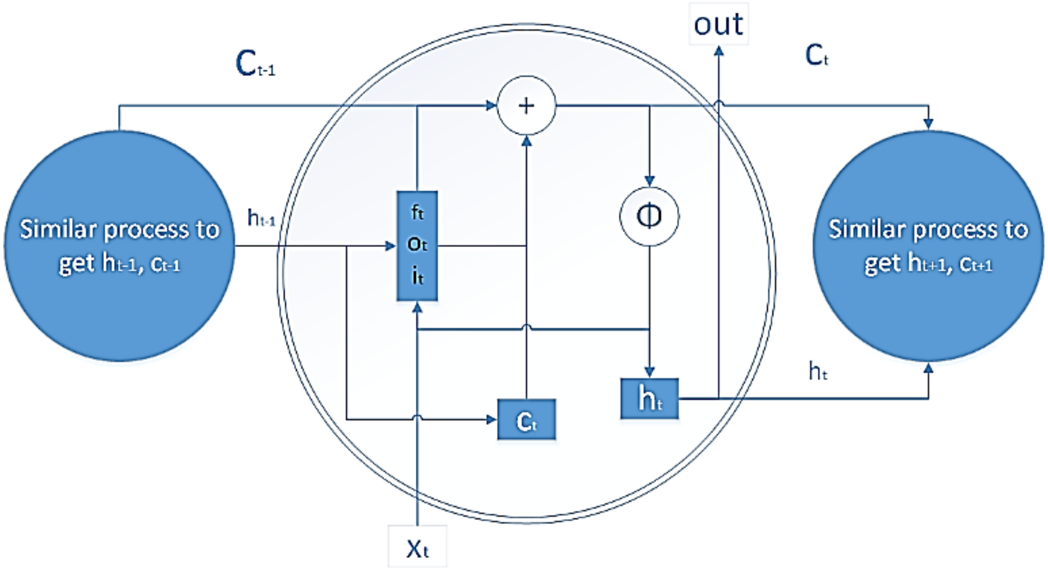

Figure 4-4- memory block with the memory cell Ct

Figure 4-4 illustrates the (LSTM) adopted from [116], where x_t and h_t show the input and state at time t. Similarly, we have h and x at time t-1 and t+1, etc. C_t and h_t are defined as long-term and short-term (hidden) memory in this cell. According to the diagram, the chain of action happens in the network and lets the network learn long-term. The following equation will demonstrate the calculation of h_t and C_t at the tth step in this process.

$$f_t = \sigma(U_f x_t + W_f h_{t-1} + b_f) \qquad (4\text{-}5)$$

$$i_t = \sigma(U_i x_t + W_i h_{t-1} + b_i) \qquad (4\text{-}6)$$

$$o_t = \sigma(U_f x_t + W_f h_{t-1} + b_f) \qquad (4\text{-}7)$$

$$\acute{c}_t = tanh(U_o x_t + W_o h_{t-1} + b_o) \qquad (4\text{-}8)$$

$$c_t = f_t c_{t-1} + i_t \acute{c}_t \qquad (4\text{-}9)$$

$$h_t = o_t \tanh(c_t) \qquad (4\text{-}10)$$

where U_i and W_i are matrices for weight; b_i is the bias; σ is a sigmoid activation function c_t' is the candidate for the cell state value.

In this study, we utilized "*Keras: The Python Deep Learning library*" to construct the time delay model. Similar to previous approaches, we split the dataset into training and testing sets, with 70% of the data allocated for training, 15% for validation, and 15% for testing. The LSTM-RNN architecture consists of one layer each for input, output, and LSTM with memory blocks. To evaluate the model's accuracy, we used two criteria: i) root mean square error (RMSE), and ii) ENS (Nash-Sutcliffe efficiency coefficient), which are commonly used in hydrological research to assess the correlation between predicted and observed outcomes. The calculation formula is shown as follows:

$$\text{MSE}=\sqrt{\frac{\sum_{i=1}^{N}(O_i-P_i)^2}{N}}, \qquad (4\text{-}11)$$

where O_i, P_i, and N are observation at time i, prediction at the time i, and several observations, respectively.

4.3. Results of Journal Paper 3

Forecasting time series accurately, particularly water levels for early flood warnings, is an essential but complicated process. A classical statistical method, a classical ML algorithm, and a state-of-the-art Deep Learning method. Respectively, the methods are seasonal autoregressive integrated moving average (SARIMA), Random Forest (RF), and Long Short-Term Memory (LSTM) which are widely used and effective forecasting models that have been proposed and tested on hydrological time series. Figures 4-2 and 4-3 present the monthly and annual data of these three selected stations. We evaluated and compared all tested ML methods by dividing collected data into two parts for training and testing. The samples were taken with different frequencies from January 1, 2007, to June 3, 2017, for Pembina station, from January 1, 2007, to February 7, 2017, for Drayton station, and from January 1, 2007, to August 5, 2017, for Grand Forks station. As mentioned previously, studied data involve 70 percent of data as a training set, 15 percent as validation, and 15 percent as a testing set. All models were trained on the training datasets and then used the trained models to forecast at a different time on the testing sets.

Table 4-2- Evaluation of the performance of SARIMA, RF, and LSTM models at three USGS stations root mean square error (RMSE between the predicted and observed water level data in the testing phase)

Pembina	**6 Hours RMSE**	**12 Hours RMSE**	**1 day RMSE**	**3 days RMSE**	**1 week RMSE**
SARIMA	0.108	0.204	0.505	1.860	2.268
RF	0.101	0.160	0.269	0.865	2.287
LSTM	0.023	0.031	0.039	0.076	0.190
Drayton	**6 Hours RMSE**	**12 Hours RMSE**	**1 day RMSE**	**3 days RMSE**	**1 week RMSE**
SARIMA	0.041	0.074	0.152	0.535	1.491
RF	0.038	0.096	0.184	0.707	1.819
LSTM	0.028	0.035	0.041	0.065	0.151
Grand Forks	**6 Hours**	**12 Hours**	**1 day**	**3 days**	**1 week**

	RMSE	**RMSE**	**RMSE**	**RMSE**	**RMSE**
SARIMA	0.609	0.655	0.754	1.198	2.027
RF	0.135	0.246	1.059	1.632	2.673
LSTM	0.022	0.028	0.051	0.086	0.107

After applying the algorithms described above to three different sampling stations, the models were extracted for further evaluation and tabulated in Table 4-2. The table gives the details on the average forecast results of all tested methods at five different time intervals: six hours, twelve hours, one day, three days, and one week, for the Pembina, Drayton, and Grand Forks datasets. Low values of RMSE indicate higher forecast accuracy of the chosen models. The best results for each forecasting horizon are highlighted in bold. By detecting the structures of the SARIMA, RF, and LSTM models, it was verified that the LSTM is more accurate than the two other models. The reason is that the LSTM model possesses a lower RMSE than the RF and SARIMA models for predicting the water level data for the Red River of the North. Comparing the LSTM to the RF and SARIMA models in the Pembina station, the RMSE values are lower by 77.22 percent and 78.70 percent, respectively. Furthermore, there are 26.31 percent and 31.71 percent reductions in RMSE between the RF and SARIMA models at Drayton station, respectively, when using LSTM. Finally, the RMSE values for the Grand Forks station for LSTM are 83.70 percent lower than the RF model and 96.39 percent lower than the SARIMA model.

Figures 4-5, 4-6, and 4-7 present the visual comparisons of all methods for forecasting one week of water level at Pembina, Drayton, and Grand Forks using a classical statistical method, SARIMA, a classical ML algorithm, RF, and a deep Learning method, LSTM. The green line indicates the observed data which were used as test data, and the red line indicates prediction data which is the output of our models.

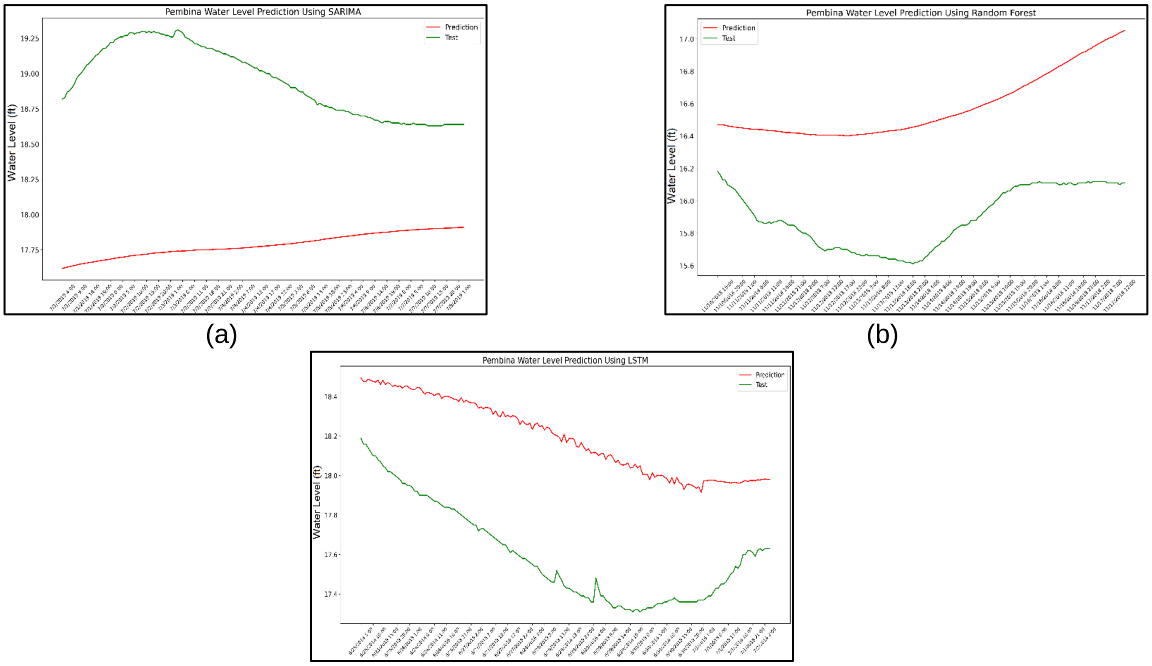

(a)

(b)

(c)

Figure 4-5- Visual comparison of one week-ahead predicted values using (a) SARIMA, (b) RF, and (c) LSTM forecasting methods with true values on the Pembina series

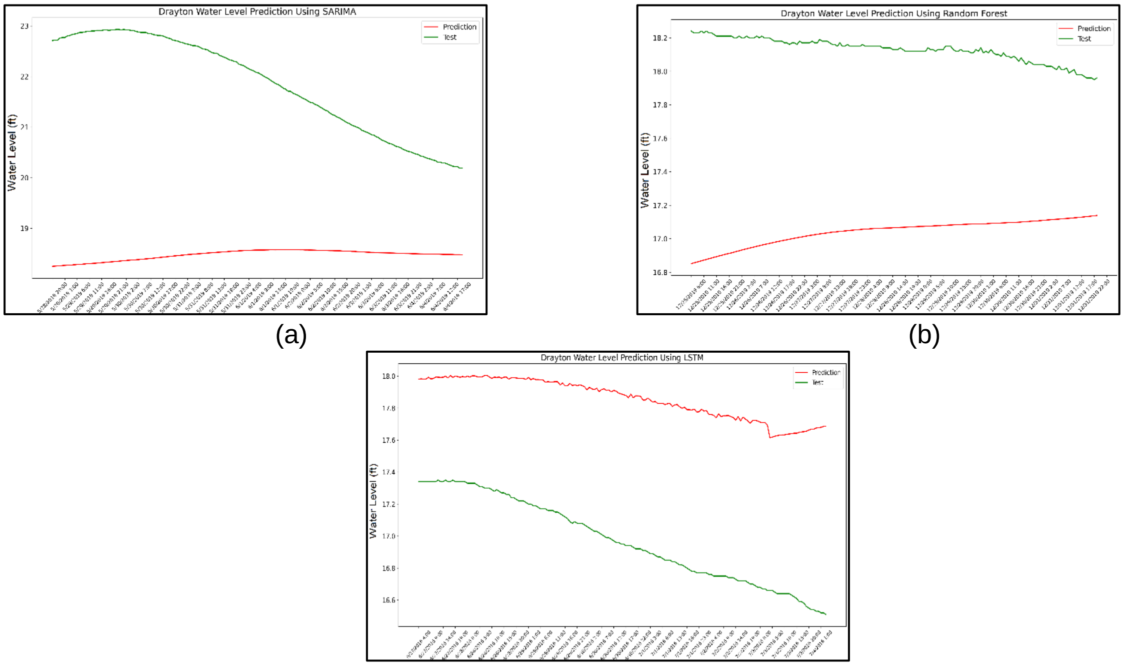

(a)

(b)

(c)

Figure 4-6- Visual comparison of one week-ahead predicted values using (a) SARIMA, (b) RF, and (c) LSTM forecasting methods with true values on the Drayton series

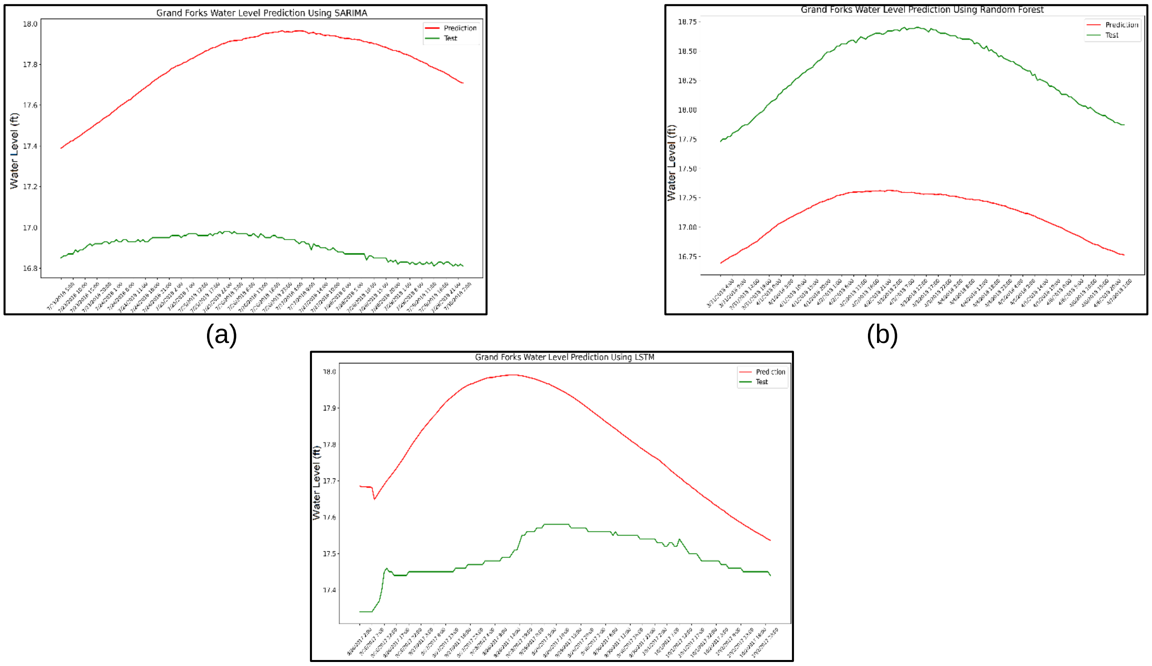

(a) (b)

(c)

Figure 4-7- Visual comparison of one week-ahead predicted values using (a) SARIMA, (b) RF, and (c) LSTM forecasting methods with true values on Grand Forks series

Figure 4-5 shows the results of forecasting the water level in a randomly chosen period at Pembina station one week ahead using SARIMA (from 07/01/2019 to 07/08/2019, Figure 4-5-a), RF (from 11/10/2018 to 11/18/2018, Figure 4-5-b), and LSTM (from 06/25/2018 to 07/02/2018, Figure 4-5-c). When forecasting one week in advance, the LSTM yields the best results, as it could capture well the trend of the actual data. The results show that the LSTM performed better than the RF and SARIMA to predict the water level, with an average difference of 0.583 ± 0.21 feet between tested and predicted water levels for three stations. The mean difference between the tested and predicted water levels for RF and SARIMA is 0.983 ± 0.64 feet, and 1.848 ± 0.97 feet, respectively. The other two methods do not work as well as LSTM for the Pembina station. Figure 4-6 demonstrates the results of forecasting the water level in a randomly chosen period at Drayton station one week ahead using SARIMA (from 05/28/2019 to 06/04/2019, Figure 4-6-a), RF (from 12/25/2019 to 12/31/2019, Figure 4-6-b), and LSTM (from 06/27/2016 to 07/04/2016, Figure 4-6-c). Figure 4-7 shows a similar result to the case of Drayton station in that LSTM could forecast quite accurately the peak one week ahead. It still captures rather well the trend of the data in one-week ahead forecasts, but the errors are high. Meanwhile, all other methods failed to forecast and could not capture the data trend.

For Grand Forks data with hourly sampling, in a randomly chosen period for one-week prediction ahead using SARIMA (from 07/23/2018 to 07/30/2018, Figure 4-7-a), RF (from 03/31/2018 to 04/07/2018, Figure 4-7-b), and LSTM (from 08/08/2019 to 08/15/2018, Figure 4-7-c). Figure 4-7 demonstrates once again that the LSTM approach is superior to the SARIMA and RF methods. When predicting water levels one week ahead, LSTM produces the closest values to the real ones (Figure 4-7-c). When forecasting water levels one week in advance, SARIMA and RF originate good results as in the case of one week, but LSTM produces predicted values, which are more similar to the true ones than other methods (Figure 4-7-c). Although RF is second behind LSTM, the gaps between the forecast errors of the two methods are rather wide.

Figures 4-5, 4-6, and 4-7-c demonstrate that for all water levels in all three stations, the LSTM method forecasted slightly overestimated. As can be seen in Figures 4-5, 4-6, and 4-7-a, SARIMA underestimated the water level for Pembina and Drayton stations but overestimated the water level for Grand Forks station. Finally, the RF method overestimates the water level for the Pembina station but underestimates the water level for Drayton and Grand Forks stations (Figures 4-5, 4-6, and 4-7-b).

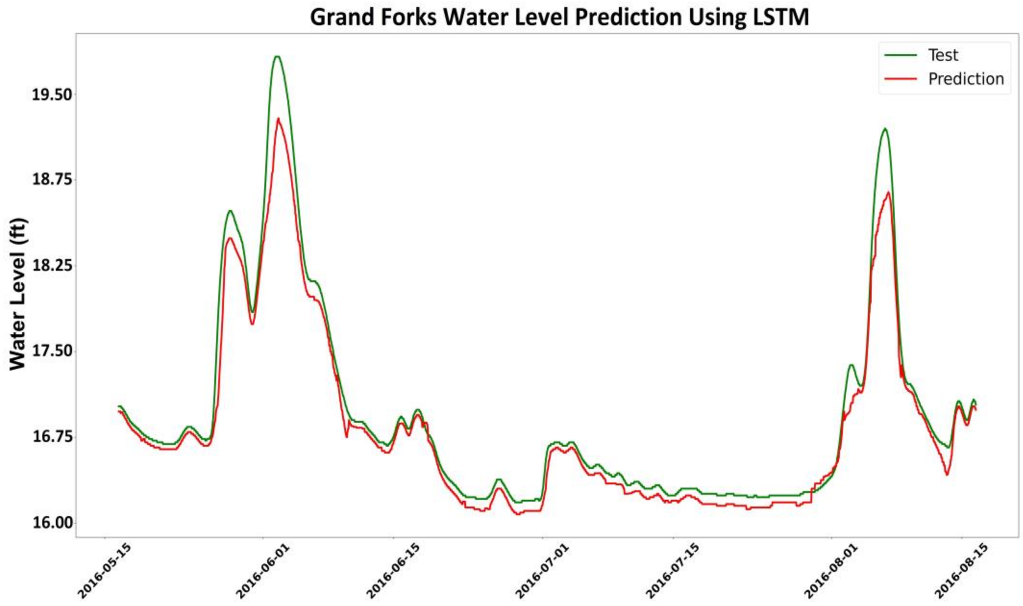

Figure 4-8- Visual comparison of 3 months predicted values using LSTM forecasting method with true values on Grand Forks series

Although figures 4-5, 4-6, and 4-7 indicate the capacity of the model to estimate water level in two weeks, the short duration of sampling data may not be a suitable representation of the models' capturing the flood peak. To present the accuracy of our model with different water level datasets as driving inputs in capturing the flood peaks and time of the peak, we have considered one extreme three months period that occurred in 2016 from May 16 to August 14. The major reason we offer this plot is that the reader cannot see how our model is excellent based on the statistics above. For this purpose, we have considered the maximum water level events in the year 2016 and forecasted these events one week ahead. Figure 4-8 presents a comparison between observing and predicted data in Grand Forks station. The green line indicates the observed data which were used as test data, and the red line indicates prediction data which is the output of our model. The results indicate that the peak flow scenarios in the field for May to August 2016 are well captured by trained LSTM.

4.4. Discussion and Conclusion of Journal Paper 3

Accurately predicting time series, particularly water levels for flood warning systems, is a crucial yet challenging task. Forecasts of water levels at Red River flow gauging stations, particularly downstream stations like Pembina in this study where no discharge information is available, are critical for early flood warning systems. In this research, we evaluated three different methods: SARIMA, a classical statistical method; RF, a classical ML algorithm; and LSTM, a Deep Learning method. Our analysis of the models for Pembina, Drayton, and Grand Forks stations revealed that the LSTM method outperformed SARIMA and RF in terms of accuracy and prediction performance. While SARIMA is useful for modeling linear data, other statistical and machine learning models are better suited for modeling machine learning. To effectively predict water levels in a time series, it is necessary to consider both linear and nonlinear correlation structures. Results from this study indicate that the Deep Learning LSTM algorithm is a dependable choice for flood prediction. The LSTM model performed better than both the RF and SARIMA models at all three stations (Pembina, Drayton, and Grand Forks) for all prediction times, with significantly lower RMSE values by 77.22% and 78.70%, respectively. At the Drayton station, the LSTM model resulted in a 26.31% and 31.71% reduction in RMSE compared to the RF and SARIMA models, respectively. For the Grand Forks station, the LSTM model achieved lower RMSE values by 83.70% compared to the RF model and 96.39% compared to the SARIMA model. The study also found that a water stage time series can have both linear and nonlinear correlation structures.

5 CHAPTER 5. Impacts of Climatic Variability on Surface Water Area Observed by Remotely Sensed Imagery in the Red River Basin

5.1. Introduction and Background

The Northern Great Plains (NGP) is a region in northern central North America that includes parts of the United States and Canada. The NGP has a variety of unique hydrological habitats that are characterized by topographic depressions and create dynamic aquatic water features such as lakes, marshes, washouts, and wetlands [117]. These depressions work like sponges, absorbing up surplus water during floods and releasing it during droughts [118, 119]. Due to the relatively flat topography of NGP, it is home to millions of prairie pothole depressions of glacial and post-glacial origin [120]. According to recent research, global climate change has resulted in a significant rise in precipitation regime [121], which has a cascading effect on surface water area in cold region plains (e.g., NGP, plains of Russia) [122, 123]. Precipitation is projected to rise in NGP in the future. The effects of a recent climate change toward increasing precipitation on surface water area were not well recognized, particularly in the Red River Basin (RRB), which is located on the eastern boundary of the NGP.

Because of a highly changing precipitation regime, the hydroclimatic conditions in NGP have evolved during the previous three decades, and NGP has become wetter in general. This increased wetness has resulted in the extension of existing wetlands and lakes, as well as the formation of new wetlands in many watersheds due to the fill-spill process [124]. Climate change has already had an impact on the area, since precipitation has increased [125, 126] and caused NGP to shift from dry to extremely wet periods in the last four decades [127]. Since 1991, NGP has had two wet periods of increased precipitation, both of which resulted in disastrous flooding: 1994-1999 [128] and 2004-2011 [129]. There was only one drought period (1999-2003) between the two wet periods [124]. During the wet season, some NGP basins saw major floods caused by snowmelt, spring/summer rain, and rain-on-snow (ROS) occurrences. Recent flooding happened in 2009, 2011, and 2013 [130-133]. On the other hand, dry periods result in no change or decrement in the surface water area [125, 128, 130, 134, 135].

The RRB was chosen as a crucial section of the NGP in this study because it is home to a diversity of wetlands and prairies. It is an important migration route for many species, and frequent flooding has presented a constant danger to this environment over the last 30 years, restricting habitat and significantly harming water quality [29]. The total water storage changes dramatically over the year, with the peak levels happening prior to snowmelt in the spring and the lowest levels occurring at the end of the summer. Based on Gravity Recovery and Climate Experiment (GRACE) satellite measurements, the average range of seasonal changes during the previous decade was 124 mm [136]. Variation in water levels of wetlands in the RRB has been previously studied, which consists of water level measurements at the local scale [137, 138]. Therefore, a complete investigation of the inter-annual and intra-annual RRB surface water area is required to identify flood-prone locations and water bodies that expand or contract with climate variability.

Recent research has shown that remote sensing technology and image classification algorithms may be used to accurately estimate changes in the area of surface waters [139-141]. Sethre et al. (2005) delineated water bodies, i.e., wetlands, in Devils Lake, North Dakota, using a standard density slicing approach of the short-wave infrared (SWIR) band (Band 5) from Landsat Thematic Mapper (TM) images. It is the RRB's largest natural aquatic feature and the sole terminal lake. Since 1990, Devils Lake has experienced an important change in area climate, resulting in a 10-meter increase in water level [142]. Todhunter and Fietzek-DeVries (2016) discovered that interannual and interdecadal climate variability in Devils Lake is superimposed over two longer-term climate variation modes; the principal drivers of long-term lake volume variations are a more extended and drier mode and a shorter and wetter mode. During the drier phase, precipitation dominates Devils Lake's water budget [134]. As the long-term climate moves to a wetter deluge phase, the lake adopts a runoff-dominated water budget after a temporal lag caused by basin memory effects. Another study on a Devils Lake headwater basin found two unique cold region hydrologic responses, one before 2011 dominated by increased fall antecedent soil moisture and rain on snow occurrences, and one after 2011 regulated by streamflow and evapotranspiration [143].

This study investigates the spatiotemporal variability of the RRB's surface water area from 1990 to 2019. In the majority of studies [139, 140], surface water area is reported to have increased over the whole drought-to-deluge transition (1990-present). However, we believe there are two wet periods [144] and one drought period between them [143] during the 1990-present period. We used the Global Surface Water Dataset (GSWD) with a 30 m resolution for 30 years (1990-2019) [141]. The time series of annual and monthly surface water extent was estimated using this dataset. The GSWD was obtained using the Google Earth Engine (GEE). The GSWD annually offers information on the presence of both permanent and seasonal water across the continental land of Earth. In order to extract precise information from time series for 30 years in the RRB and reduce noisy information, the study employed singular spectrum analysis (SSA) [145]. The Mann-Kendall trend test also was used to detect trends in time-series data in the RRB over the study period [146]. The goals of this study are to determine surface water area responses to drought times and to give a more critical assessment of the surface water area variance in RRB. In this study, we investigate three types of water areas: permanent (occurring all year), seasonal (occurring part of the year), and total (a sum of permanent and seasonal water areas). Using a dataset that Pekel et al. presented, our objective is to identify the spatiotemporal variability of the surface water area (2016) [141].

5.2. Methodology

5.2.1. Study Area

80 percent of the Red River basin is in the United States and 20 percent is in Manitoba, Canada. It is a 116,550 km^2 (45,000 mi^2) international, transboundary, and multijurisdictional watershed (Figure 5-1a). It measures 507 kilometers in length and 97 km at its widest point. It reaches its northernmost point in Lake Winnipeg in Manitoba from the southernmost portion of Traverse Lake in South Dakota [147]. Eastern North Dakota, northern Minnesota, northeastern South Dakota, and southern Manitoba in Canada are all included in the RRB drainage region [148].

RRB's climate is humid continental, with warm to hot summers and cold winters [149, 150]. The air temperature fluctuates from 48°C in August to -48°C in January and February [151]. The average annual precipitation in the basin ranges from approximately 430 mm in the west to more than 673 mm in the east [152]. Typically, 22% of yearly precipitation falls as snow in winter and the remainder as rain, mainly as severe thunderstorms in summer, with up to 7.5 cm of rain per day [147]. Most streamflow occurs in the spring due to snowmelt and rain on snow, whereas runoff in the summer is caused by many days of intense rainfall on saturated soil [130]. Yet, the Red River and its tributaries regularly experience significant flooding due to the basin's relatively flat geography and humid climate. Flooding mostly happens in the spring and early summer, and it gets worse when it rain [2]. Spring floods account for most of the significant historical floods.

The RRB has several unique watershed features in addition to the significant snowmelt streamflow and associated floods. The basin features a large number of regulated reservoirs and dams [153], a low channel gradient and lack of topographic relief, and frozen ditches and culverts that temporarily retain water during spring runoff [4]. Furthermore, wetlands remove pollutants and nutrients from water systems allowing lakes, streams, and aquifers to remain clean. Besides, they decrease erosion, lessen flooding, and refill groundwater [153-155]. Many wetlands in the RRB have been lost because of excessive drainage and urbanization [156]. The basin is a nearly featureless plain with poorly drained silty and clayey soils. The entire basin is covered with a layer of glacial drift (sand, gravel, and rocks deposited by glaciers). Although groundwater is a vital water source in the RRB, snowmelt runoff provides the majority of the streamflow in the Red River and its tributaries [157].

Three major ecoregions in the RRB are upland, lowland, and escarpment. We define them below (Figure 5-1b):

1) Upland: The Northern Glaciated Plains (Aspen Parkland) comprise one-third of the RRB in the west, and the majority of the basin is located in North Dakota (Figure 5-1b). In the region, flat to moderately sloping plains produced by glacial moraine may be seen. Lacustrine and hummocky to ridged fluvioglacial deposits exist, with Tertiary and Cretaceous sandstones and shales as the dominant bedrock. The density of streams and rivers on the site is modest. The Devils Lake basin is a closed basin in the Red River watershed in the north, covering 9,868 km^2 and encompassing a substantial amount of the highland ecoregion. The topographic formation of the Devils Lake Basin is unique due to the great number of shallow depressions of small lakes, ponds, wetlands, moraines, outwash plains, and drumlins [117, 120, 158].

2) Lowland: The lowland region covers about half of the RRB's central section (Figure 5-1b). It descends from the basin's center, encompassing the Red River Valley and orienting itself north/south following the river. The topography is extremely flat, with higher altitudes found exclusively in the south and lower elevations found in the north. When the tributaries hit the lowlands of the lakebed, the river slopes become flat, with poorly defined watershed limits. The region is crisscrossed with low-density, low-gradient stream and river networks, which frequently flood in late winter and early spring [159].

3) Escarpment: The Manitoba Escarpment is an escarpment between upland and lowland in the western region of the RRB (also known as the Pembina Escarpment in North Dakota). The escarpment has a relief of 200 meters and fairly steep topography

[130]. The eastern margin is much less distinct and marked by a gentle topographic rise to late Quaternary glacial deposits.

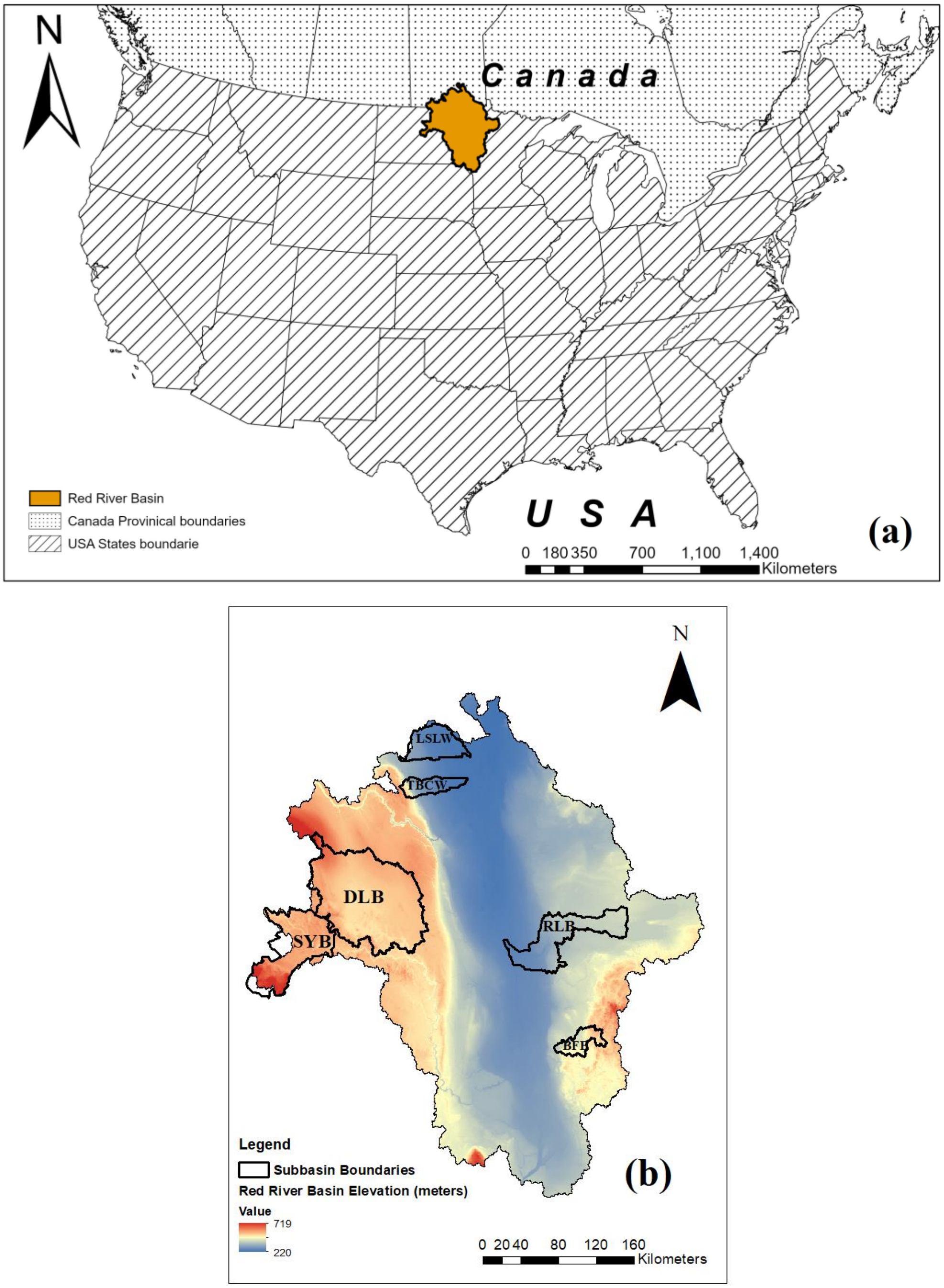

Figure 5-1- Location of the study site and hydrometeorological observatories and land surface properties: (a) The frame shows the location of the Red River in the USA, (b) Locations of the subbasins selected to study the spatiotemporal variation of the surface water area in the Red River. The six headwater basins are: Devils Lake Basin (DLB), Sheyenne River Basin (SYB), LaSalle Watershed (LSLW), Tobacco Watershed (TBCW), Red Lake River Basin (RLB), and Buffalo Basin (BFB).

5.2.2. Data

GSWD cloud-free water images from spring through summer were used to estimate yearly and monthly surface water extent time series [141]. This dataset is free and comprises photos at a resolution of 30 m for 30 years (1990-2019). Whole archive of orthorectified, top-of-atmosphere reflectance and illumination temperature images (L1T) from the Landsat 5 Thematic Mapper (TM), Landsat 7 Enhanced Thematic Mapper-plus [160]. Landsats 5, 7, and 8 are in a near-polar orbit with 16-day repeat coverage; two satellites operate on an 8-day cycle at the same time. We quantify the local and regional changes in permanent, seasonal, and total surface water area over a 30-year period in our analysis of this data. The pixels are divided into two groups: permanent water area (PWA) and seasonal water area (SWA) (SWA). Total water area (TWA) for a year is the sum of PWA and TWA. A PWA pixel is continuously submerged throughout the year, whereas an SWA pixel is inconsistently underwater throughout the year. It should be noted that the water bodies in NGP frozen over during the winter season (4-5 months depending on the duration of the winter). Surfaces that are covered in water seasonally are those that have water for fewer than 12 months of the year or fewer months than the total number of months having valid observations. Total surface water referred to streams, rivers, lakes, reservoirs, and wetlands which can persist all year long or for only part of the year.

The Google Earth Engine (GEE), a computational platform developed by Google, Inc., has enabled the development of global-scale data products based on satellite picture time series, such as the Landsat archive [161]. GGE presents GSWD water history on an annual and monthly basis. Water is a highly variable land surface feature that presents a difficult spectral target (at the wavelengths measured by the TM, ETM+, and OLI sensors) to chlorophyll concentration, total suspended solids, and colored dissolved organic matter load, depths, and bedload material for shallow waters, as well as variations in observation conditions (sun-target sensor geometry, and optical thickness). Pekel et al. (2016) used big data technology systems including expert systems [162-164], visual analytics [165], and evidential reasoning to address these issues [166].

The annual GSWD offers statistics on permanent and seasonal water occurrence over the Earth's continental land area [141]. The monthly statistics from Spring through Summer, on the other hand, report the incidence depending on the water month of interest. The European Commission Joint Research Centre (JRC) sponsored and released this dataset, and it also maintains a current archive. Using GEE, we created algorithms to obtain both annual and monthly water data for the RRB from 1990 to 2019 (from Spring to Summer with little cloud cover). While annual water data is available for all years with no limits owing to large cloud cover and Landsat 7 SLC off issues, the monthly dataset did encounter significant cloud cover and Landsat 7 SLC off difficulties. Obtaining images was frequently challenging owing to severe and continuous cloud cover during the winter season (Oct-Mar). Therefore, we visually checked all monthly water maps from 1990 to 2019 and created a database of maps with no cloud cover. In this research, we interpret the water maps during April–May period as the spring season water area while the water maps of the July- September period is considered to represent the summer season.

To broaden our research, we incorporate precipitation and temperature data, as well as their temporal history over the study region, to better support our findings and the relationship with climatic variability. Obtaining full yearly precipitation and temperature data can be difficult, especially in the absence of a comprehensive source. The National Weather Service (NWS) was employed in this example to acquire precipitation and temperature data for the research period. It is usual practice to choose selected stations as proxies for the area to guarantee that the data is reflective of the region of interest. To overcome this issue, the stations in Grand Forks and Fargo were chosen as proxies for the lowland region, whereas Edmore was picked to represent the highland region.

Monthly data for the research period was then downloaded and utilized to construct annual datasets. Given the scarcity of data throughout the research period, the data from these three stations are regarded as typical of the region of interest and acceptable for further analysis and interpretation. We conducted an additional Mann-Kendall test to examine the correlation between water surface area, temperature, and precipitation over the four recognized phases to further analyze these trends.

5.2.3. Data Analyses

During a period of 30 years in the RRB, we utilized Singular Spectrum Analysis (SSA) on water regions to dissect significant hydroclimatic phases. SSA is a nonparametric technique for time series analysis. By removing noise from time series, it can extract as much correct information as feasible [167, 168]. SSA has evolved into a standard tool for analyzing climate, meteorology, and geophysics time series [169-171]. SSA provided the trend, periodic components, and noise components. The SSA-denoised waveforms are then reprocessed to improve the applicability and accuracy of altimeter data. Since surface water fluctuation dominates a basin's water budget variability, monthly surface water data were utilized for SSA and to define the hydroclimatic phases. As the monthly surface water data includes serial dependencies and may be divided into seasons, years, or decades, SSA is able to decompose it.

In addition, for the 1990-2019 period, we used the Mann-Kendall trend test on annual total, permanent, and seasonal water areas, as well as precipitation and air temperature in the RRB. The Mann-Kendall test [172] s widely known as a non-parametric test to analyze long-term data sets and detect statistically significant trends. Due to its rank-based procedure with resistance to the influence of extreme values, the method facilitates the trend analysis for variables having skewness [173-175]. The Mann-Kendall test can be utilized to determine whether an increasing or decreasing trend exists [146]. The p-value in this test shows the chance of error when the trend differs from zero. The absolute value of Z is compared to the standard normal cumulative distribution to assess whether or not there is a trend at the chosen significance level. A Z number that is positive or negative shows an upward or downward trend.

5.3. Results of Journal Paper 4

5.3.1. Annual Spatiotemporal Variability of Surface Water Area

TWA expanded from 3247 km^2 in 1990 to 6031 km^2 in 2019. TWA covers both permanent and seasonal water areas (PWA and SWA) (Figure 5-2c). The PWA expanded from 2590 to 3635 km^2, accounting for 79% to 60% of the TWA (Figure 5-2a). PWAs include big lakes such as Lake Alice, Red Lake, and Devils Lake (Figure 5-3), whereas SWAs are classified wetlands in the RRB and have increased from 656 to 2395 km^2 during the research period, accounting for 20% to 40% of TWAs (Figure 5-2b). The basin's central region, which is adjacent to Grand Forks, North Dakota, and Emerson, North Dakota (Figure 5-3), has the most noticeable seasonal water area and is frequently flooded in the spring when it rains heavily. Table 5-2, which is consistent with previous research in the Western Region, displays a rising trend for TWA and PWA for 1990-2019 based on the Mann-Kendall trend test that is significant at $p < 0.05$ [120, 176] and the Northern Great Plain [177]. During the 1990-1997 era, the temporal dynamics of the total water area agreed with both permanent and seasonal regions. Yet, SWA fluctuates significantly after 1997, but PWA fluctuates just slightly.

The chain of lakes in the Devils Lake area (upland area) and the large lakes in the Red Lake area are the two most prominent permanent water features shown in Figure 5-3. (eastern edge of the basin). While TWA, PWA, and SWA across the Devils Lake Basin have all significantly increased, they are still constant in the Red

Lake region. PWA and SWA expanded their territory in the western (near Devils Lake) and southeastern regions of the RRB, which are likewise located at higher elevations (> 370 m), during the wet years (for example, 1997, 1998, 2011, and 2013). We also investigated the spatiotemporal variation of PWA and SWA in two test sites. These sites include Devils Lake with about 10,000 km^2 drainage area in the west (Figure 5-4) and a large wetland Roseau River with a 30 km^2 drainage area in the east of the basin (Figure 5-5). At the beginning of the study period (1990), the Devils Lake Basin had high PWA and SWA, and the PWA is only restricted to Devils Lake (Figure 5-4). However, the wetting filled up the large depressions north of Devils Lake and converted them into a seasonal water body in 1997 and 1998. The continued wetting in these further added moisture to the system and transformed these seasonal water bodies into permanent water bodies during the 2001-2011 period. Lake Alice and Irvine are the names of these bodies of water. Consequently, the Devils Lake Basin saw two phases of wetness that substantially altered the PWAs: the conversion of the empty depression into a seasonal water region from 1990 to 1999, and the transformation of the seasonal water area into a permanent area from 1999 to the present (2001-2011). The PWA and SWA have declined slightly since 2011.

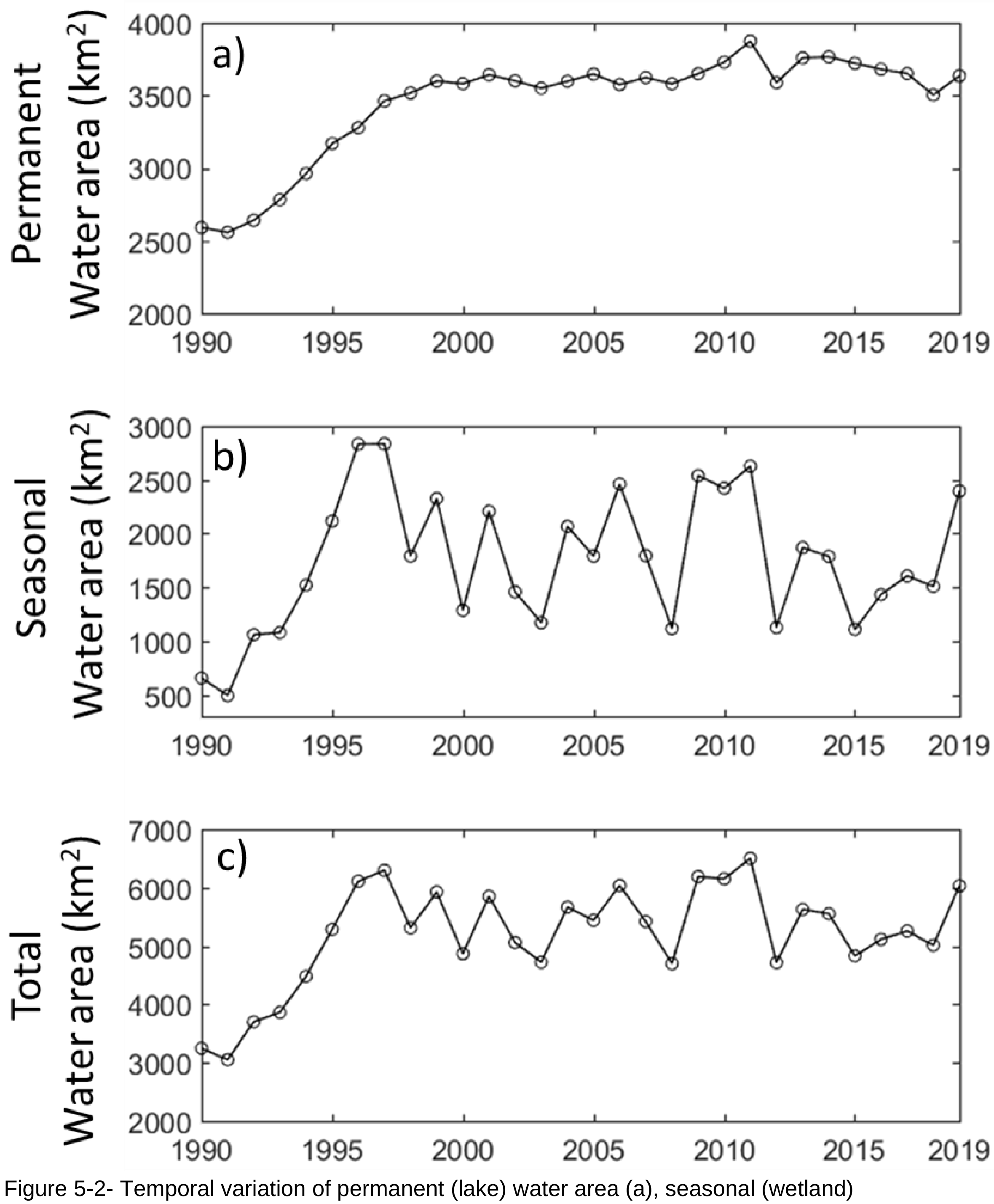

Figure 5-2- Temporal variation of permanent (lake) water area (a), seasonal (wetland) water area (b), and total (lake + wetland) water area (c) during 1990-2019.

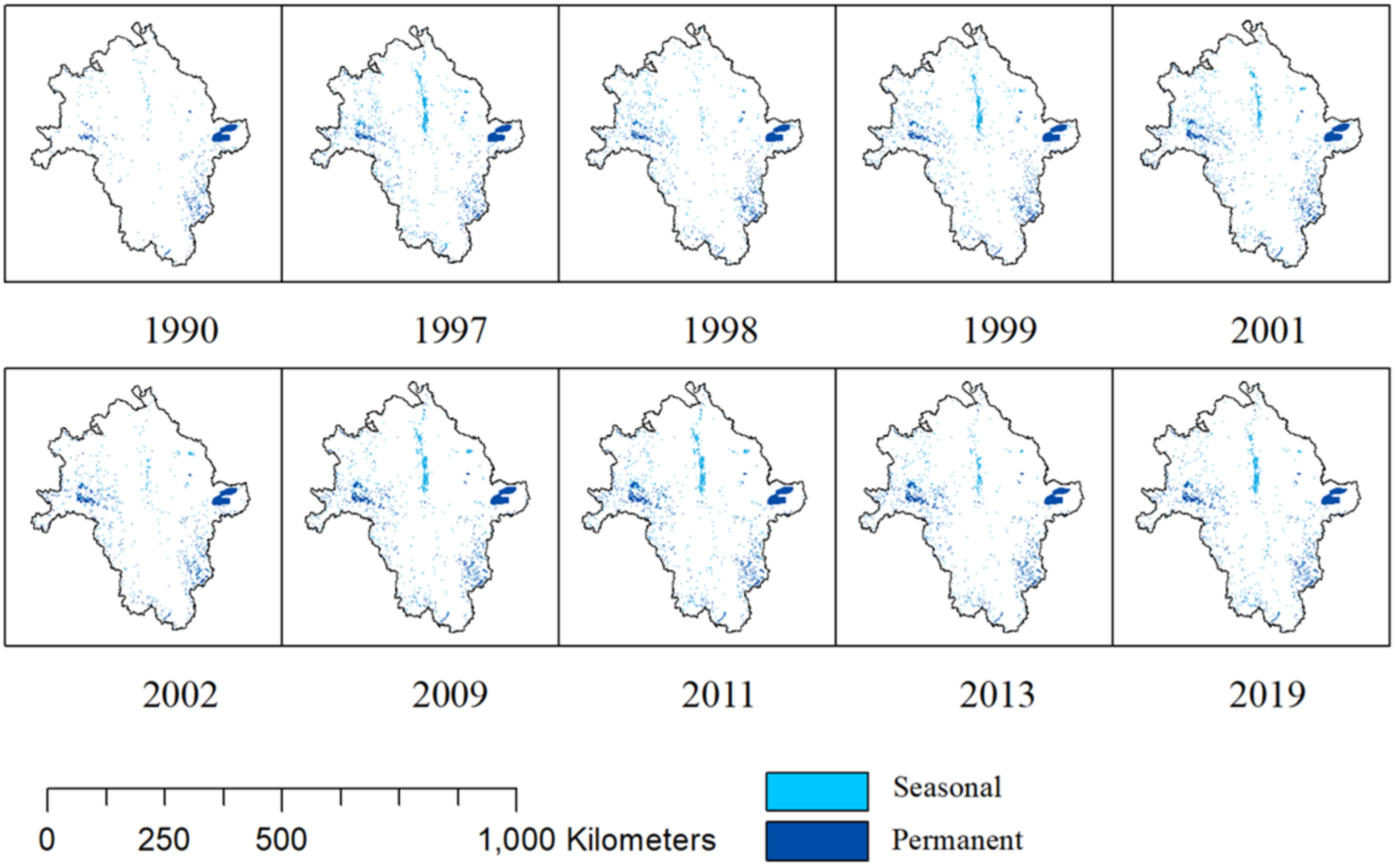

Figure 5-3- Spatiotemporal variation of seasonal water area in the Red River during 1990-2019. The dark color shows the permanent area with no change. Note that most extreme years in terms of wetness and dryness are shown.

Changes in large water bodies, such as the Devils Lake Basin of the western RRB, were rarely recorded in the eastern RRB. The Roseau River was the most prominent site where the seasonal-to-permanent water area transition was seen (Figure 5-5). SWA was present in the area from 1990 and 1997. The transition from seasonal to permanent, on the other hand, began in 1998 and finished in 1999. The PWA was present from 1999 till 2012. Since 2013, the area has been losing PWA permanent water and gaining SWA, but it has not totally converted to an SWA system.

Figure 5-6 depicts the chronological variations in the percentage contribution of PWA to RRB in upland and lowland locations (Figure 5-1b). In 1990, PWA contributed 18% in the upland and 58% in the lowland. During the preceding thirty years, the permanent area supplied by the upland to the RRB as a whole has expanded from 18% to 40%. In upland, there are two big periods of high area growth, one from 18% to 34% in 1990-1998 and another from 34% to 39% in 2007-2013. Following 2017, it slipped back to 37% from 2017 to 2019. In the lowland area, however, the PWA contribution has reduced from 58% to 44%. Like the upland area, the recession of the percent contribution by PWA to RRB has two major phases in the lowland area: one in 1990-1998 from 58% to 47% and one in 2007-2013 from 47% to 43%. During 2000-2006 and 2013-2016, the percent contribution of PWA is temporally stable in both upland and lowland areas.

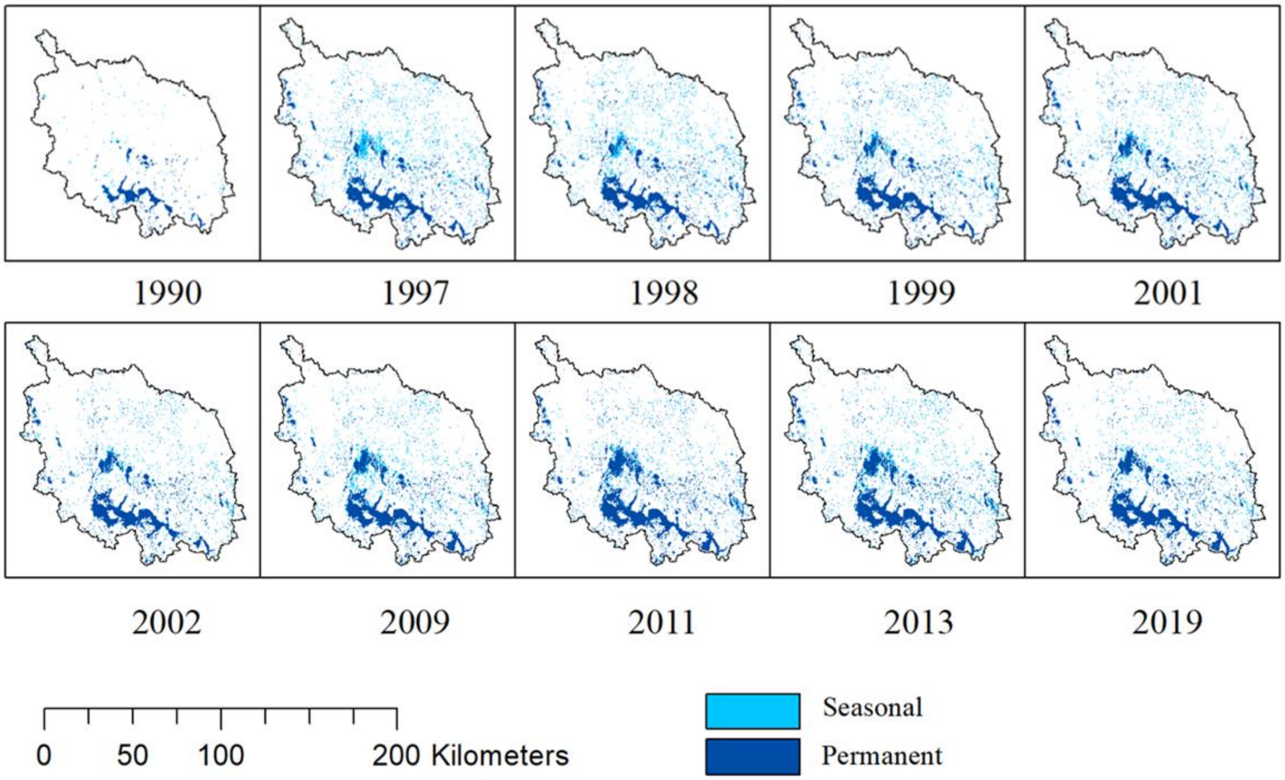

Figure 5-4- Spatiotemporal variation of permanent and seasonal water area in Devils Lake during 1990-2019. Most extreme years in terms of wetness and dryness are shown.

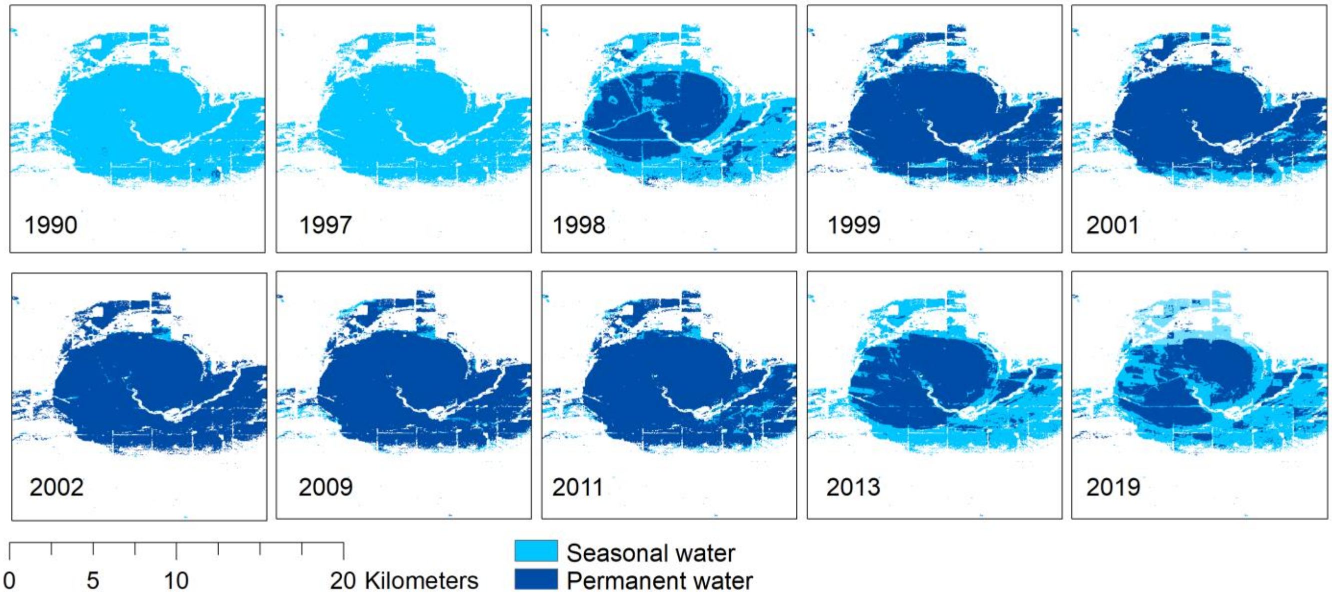

Figure 5-5- Spatiotemporal variation of permanent and seasonal water area in a small depression in the northeastern Red River during 1990-2019. Most extreme years in terms of wetness and dryness are shown.

To understand the spatiotemporal variability of TWA, SWA, and PWA, we investigate them in the six headwater basins situated at the different geomorphic units of the RRB (Figure 5-1b). The six headwater basins are: Devils Lake Basin (DLB), Sheyenne River Basin (SYB), LaSalle Watershed (LSLW), Tobacco Watershed (TBCW), Red Lake River Basin (RLB), and Buffalo Basin (BFB). DLB and SYB are in the upland area, TBCW is in the escarpment area and LSLW and RLB are hosted by the lowland area. BFB is in the highland area of the eastern RRB. The results show in upland, the temporal dynamics of the TWA, PWA, and SWA are consistent with that of the RRB, while the smaller basins such as LSLW and TBCW show different TWA, SWA, and PWA compared to the RRB. In the east of the basin, the temporal changes of TWA, SWA, and PWA of two headwater basins (RL and BFB) are consistent with the RRB.

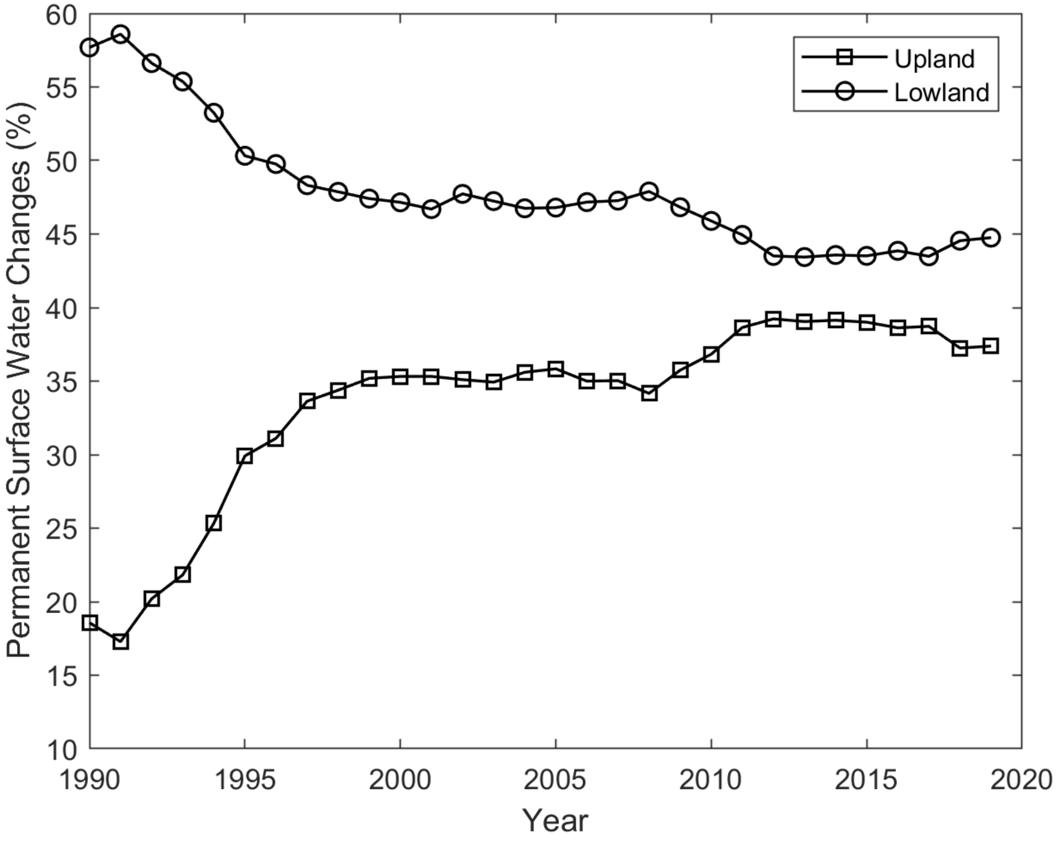

Figure 5-6-Temporal changes of the percent contribution by permanent water area to Red River Basin PWA in upland (Figure 5-1-b) and lowland areas (Figure 5-1-b). Upland is located on the west of the basin and the elevation varies from 427 to 723 m while the lowland is located in the center and east and the elevation varies from 218 to 370 m.

5.3.2. Monthly Surface Water Area

The long-term temporal trends of spring and summer TWA are consistent with those of annual PWA (Figure 5-8a), indicating a steady, increasing increase from 1990 to 1997 and a continuous variation after that year. Figure 5-8 shows a consistent seasonal pattern in which the spring TWA is significantly greater than the summer TWA. The difference between spring and summer TWAs is shown in Figure 5-8b. The disparity is greatest during flood years such as 1996 and 1997, and it is lowest during drought years such as 1993 and 2002.

We subsequently utilized a single spectrum analysis to identify four phases in the dynamics of monthly TWA (Figure 5-9). The moving average is also used to better distinguish the phases (Figure 5-9). A visual examination of the monthly TWA dynamics using SSA reveals four phases: phase 1 (1990-2001), phase 2 (2002-2005), phase 3 (2006-2013), and phase 2014-2019. These four phases in the RRB indicate an alternating of wetness (TWA increase) and drying (invariant TWA or modest decrease in TWA). Phase 1 clearly demonstrates wetness and a significant increase in TWA, however phase 2 shows a halt in the acceleration of TWA increment. After a slight pause in TWA incrementation, Phase 3 shows a continuous growth in TWA.

5.4. Discussion of Journal Paper 4

5.4.1. Annual Spatiotemporal Variability of Surface Water Area

Overall, our data indicate that the TWA in the RRB rose from 1990 to 2019, which is similar to the conclusions of Vanderhoof et al. (2018) and Archambault et al. (2019) [144, 177]. Our analysis includes the entire basin, whereas both studies just cover a portion of the western RRB. We further examined the seasonal and permanent water regions described by Pekel et al. (2016) and reported on the differences in the temporal evolution of the two types of water areas, permanent and seasonal water. Our study's findings regarding the direction of changes in the area of permanent water from 1990 to 2019 are consistent with those of Borja et al. (2020), who demonstrate that, aside from a few dramatic human-driven regional drying cases, the world's surface water systems have grown, primarily due to increased seasonal water from 1985 to 2015 [178]. The total, permanent, and seasonal surface water in the RRB have increased in general by 2890 km^2, 1151 km^2, and 1739 km^2, respectively in 30 years (see Table 5-1). Based on the map net change in Borja et al.

(2020) for surface water area over regional hydrological catchments between 1985–2000 and 2001–2015, permanent water in the RRB gains less than 2000 km^2 area, and surface and total water gain 2000 to 5000 km^2 area [178]. The total surface water includes a major impact on the pattern of seasonal water changing and a relatively small increase in permanent water changing. A comparison of estimated changes in long-term permanent water cover by Borja et al. (2020), between 1985 and 2015, shows disagreement in the direction of change that is like that between part 1 and Donchyts et al. (2016) [179]. Especially, Borja et al. (2020) study part 2 period, between 1985–2005, and 2013–2015, and Donchyts et al. (2016) are consistent in estimating an average net land area gain (permanent water loss) from the long 15-year period 1985–2005 to the short 3-year period 2013–2015, even though change magnitudes differ between these two studies [179]. PWA is largely governed by the volume of precipitation received by the wetland and the volume of water that flows into and out of the wetland. This indicates that locations with higher precipitation or more streamflow have a larger permanent water area. In contrast, SWA is influenced by how water interacts with wetlands and groundwater, as well as the rate of open water evaporation. The combination of these variables affects whether the wetland will experience seasonal flooding and how long it will remain flooded throughout the year. By demonstrating the more steady and progressive increase in PWA as well as the extremely varied temporal response by SWAs, our findings contribute to new understanding.

The spatial analyses of the PWA and SWA revealed further additional information in the context of the RRB. Our analysis revealed a notable seasonal water area in the RRB's central region (from Grand Forks to Emerson) (Figure 5-3). During rainy years (e.g., 2009, 2011, and 2013), this region floods during the spring season due to flat topography and downstream ice jams in Red River and Lake Winnipeg (Figure

5-3). In addition to detecting a sensitive area to seasonal water inundation, we further detected two most noticeable permanent water bodies with the diminishing influence of SWA during the study period; one is the chain of lakes in the Devils Lake Basin area (west of RRB in upland, Figure 5-4) and a large wetland Roseau River, 30 km^2 in the eastern RRB (Figure 5-5). Annual precipitation onto the lake surface (P_L) is 421.6 mm from 1907 to 1980, while P_L is 506.0 mm from 1981 to 2011 which shows the Devils Lake Basin experienced high precipitation regime since 1980 [128] resulting in filling up potholes and depression and basin storage. However, the surface water area has started to respond since mid-1990, as Figure 5-4 shows the emergence of SWA in 1997. The continued wetting converted the SWA to PWA during the study period. The diminishing influence of SWAs indicates that the Devils Lake Basin system transitioned from low streamflow and high evaporation system to high streamflow and low evaporation system while annual precipitation remains high and invariable during the study period (Archambault et al., 2019). The Devils Lake Basin region exhibits a remarkable shift between SWA and PWA during the research period, although being small in area (30 km^2) compared to chains of lakes (Figure 5-5). This wetland has also shown that the smaller water body is more vulnerable to any local or regional climate fluctuations.

Table 5-1- Seasonal, permanent, and total wetlands' surface water area assessed on annual surveys in the Red River Basin, 1990–2019.

Year	**Surface water Area (km^2)**		
	Seasonal	Permanent	Total
1990	656.9	2590.8	3247.7
1991	494.9	2557.5	3052.4
1992	1061.2	2640.7	3701.9

1993	1080.9	2782.7	3863.5
1994	1520.4	2962.2	4482.6
1995	2116.8	3169.4	5286.2
1996	2833.1	3277.7	6110.8
1997	2835.2	3462.8	6298.1
1998	1791.8	3517.3	5309.1
1999	2327.0	3599.5	5926.5
2000	1287.4	3581.8	4869.2
2001	2207.1	3642.6	5849.6
2002	1458.8	3601.2	5060.0
2003	1171.9	3550.1	4722.0
2004	2068.1	3597.9	5666.0
2005	1791.8	3647.9	5439.8
2006	2460.7	3575.7	6036.4
2007	1795.6	3623.8	5419.4
2008	1117.8	3580.7	4698.5
2009	2538.8	3650.5	6189.3
2010	2422.5	3729.7	6152.2
2011	2626.9	3874.6	6501.6
2012	1126.9	3588.6	4715.5
2013	1869.6	3759.0	5628.6
2014	1788.1	3766.0	5554.1
2015	1109.4	3721.8	4831.2
2016	1433.6	3681.1	5114.8
2017	1606.2	3651.5	5257.8
2018	1509.6	3503.9	5013.5
2019	2395.8	3635.4	6031.2

Our study also indicates that the western upland geomorphic unit of the RRB has higher PWA than the lowland geomorphic unit located at the central part and partly in the eastern RRB. This comparison between upland and lowland is also consistent with the hydro lake database by Messenger et al., (2004). According to the upland area PWA contribution to the RRB, PWA increased substantially, while the lowland PWA contribution to the RRB decreased. The percent of PWA contribution in 1990, 1999, 2009, and 2019 are 18, 35, 36, and 37% for the upland, while it is 58, 47, 47, and 45% for the lowland. Note that the PWA of upland RRB has increased at a much faster rate than the lowland. The upland's PWA has increased at a rate of 40 km^2/year while the rate is only 4 km^2/year in the lowland area. Rapid filling of potholes and depressions in the upland area during the 1990-1998 period has generated many permanent water bodies, improved wetland connectivity, and increased contributing areas resulting in substantial streamflow in the major tributaries (e.g., Sheyenne River, Mauvais Coulee) of Red River draining from the upland area. Similar phenomena are also observed during the 2009-2013 period resulting in massive streamflow and regional flooding in 2009, 2011, and 2013. We think the lowland permanent area is already filled at its maximum capacity at the onset of the study period. Moreover, compared to uplands, lowlands have a shallower water table due to lower elevation, flatter topography, and groundwater convergence from uplands, allowing for higher evapotranspiration and leaf area index in many places [180]. It can be concluded that the lowland is already filled up, for any flood in the future, the upland would be responsible and will lead the water to the lowland part which is in a flatter area.

The western RRB has a low density of streams and rivers but high densities of temporary and seasonal wetlands. The topographic formation of the RRB is of glacial origin and is unique due to the great number of shallow depressions of small lakes, ponds, wetlands, moraines, outwash plains, and drumlins (Sethre et al., 2005; Shook et al., 2013; Zhang et al., 2009). As can be seen in Figure 5-7, the permanent surface water has a big portion of the total water in both Devils Lake Basin and SYB which are from the upland area. In contrast, escarpment watersheds (TBCW and LSLW) have a low amount of PWA as the steeper slope of the channel causes rapid draining of wetlands and water bodies. The RLB has a low PWA due to the extensive development of drainage ditches at both headwater and downstream RLB (Stoner et al., 1993).

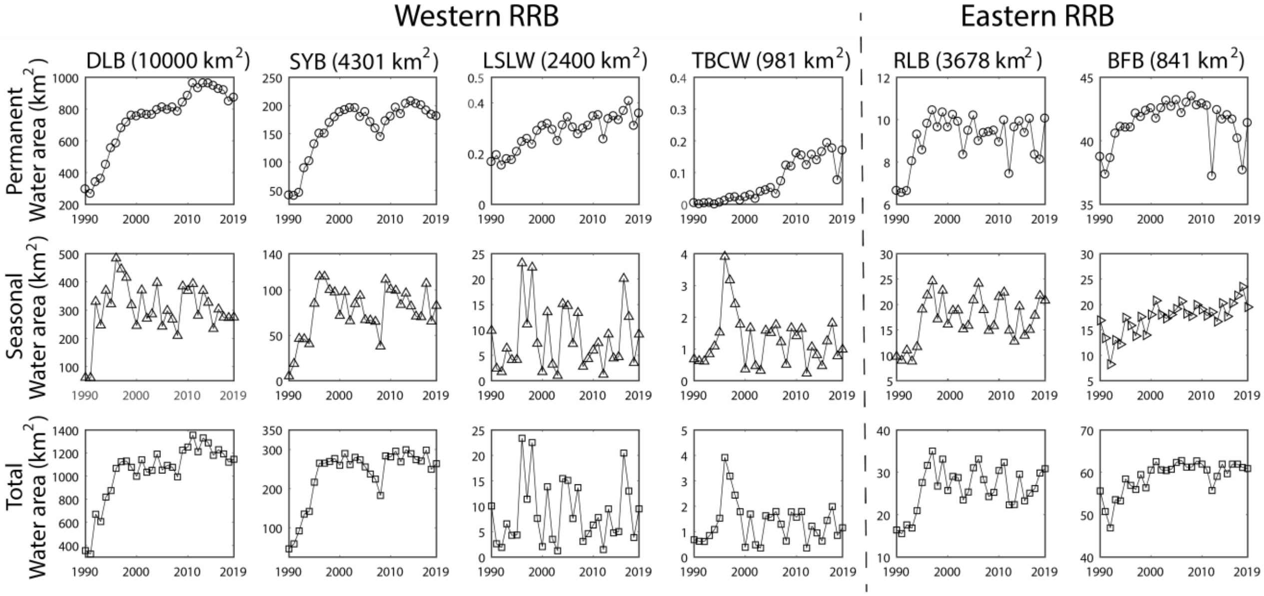

Figure 5-7- Temporal variation of permanent (lake) water area, seasonal (wetland) water area, and total water area during 1990-2019 in the six headwater basins. Note that the first four columns from the left represent the subbasins located in the western Red River while the rest of the two columns from the right represent the subbasins in the eastern Red River Basin. The first two columns from the left are Devils Lake Basin and SYB which are in the upland area.

5.4.2. Monthly Surface Water Area

The spring TWA strongly responded during the 1990-1997 wetting period, showing a significant increase across the RRB, but then subdued and fluctuated little for the rest of the study period (1998-2019) (Figure 5-8a). The summer TWA also responded to initial wetting and the TWA increment was observed till 2000. Since 2000, summer season TWA remained slightly variable (between 3000 and 4000 km^2) partly due to the consumption of summer rainfall by evapotranspiration (Figure 5-8a). The difference between the spring and summer TWAs ($diff_{TWA}$) shows an interesting pattern of temporal changes (Figure 5-8b). The spring TWA is dominated by snowmelt runoff, frozen soil infiltration, rain on snow, fill-spill hydrology, and variable contributing areas while the summer TWA depends on summer rainfall, the timing of the rainfall, evapotranspiration, open water evaporation, cloud-cover and images for spring to summer from GSWD days. Hence, the $diff_{TWA}$ is the result of the competition between winter snow accumulations, spring, and summer processes. The high $diff_{TWA}$ is observed during 1996, 1997, and 2006 as both years have contrasting spring (wet) and summer (dry) seasons. However, other years having wet springs like 2009, 2011, and 2013 have moderate $diff_{TWA}$ as the late summer rainfall is responsible for the rebound of the TWA.

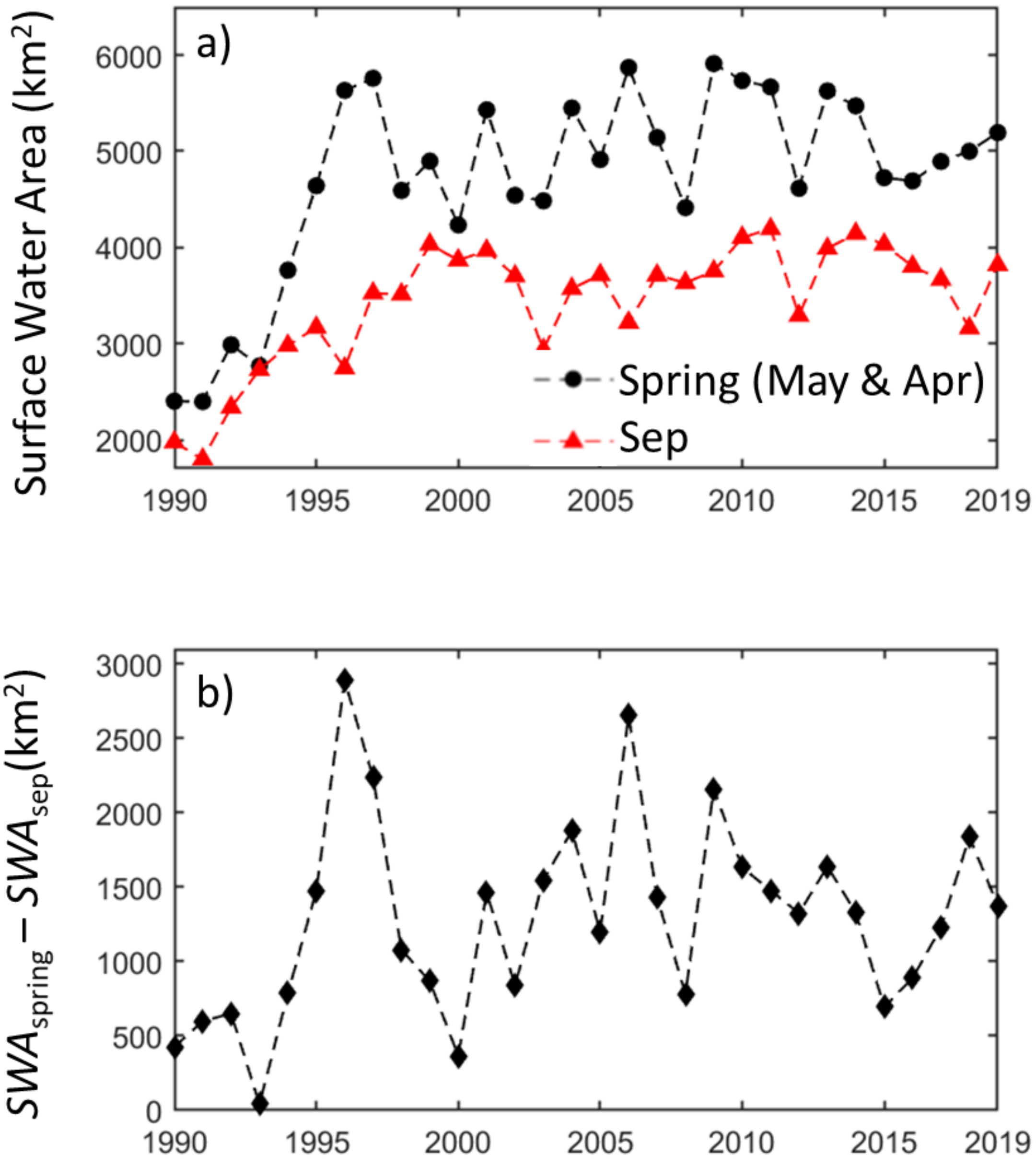

Figure 5-8- (a) Temporal dynamics of spring (Apr, May) and summer (Sep) monthly total water area (cloud-free and available data). (b) Temporal dynamics of the difference of total water area between spring and summer.

A visual examination of the monthly TWA temporal dynamics using SSA reveals four phases: phase 1 (1990-2001), phase 2 (2002-2005), phase 3 (2006-2013), and phase 4. (2014-2019). The Mann-Kendall tests are run on the SSA of monthly TWAs (Table 5-2), and the findings reveal an increased trend for phases 1 and 3, no trend for phases 2 and 4, and a negative trend for phase 4. These phases are congruent with the RRB's regional hydroclimatology, which states that phases 1 and 3 are soaking periods, phases 2 and 4 are part of the prairie drought. Phase 1 (1990-2001) exhibits wetting in which the RRB consistently received noticeable snowfall (with subsequent snow accumulation and melt) and rainfall resulting in the expansion of existing lakes and the creation of new lakes and smaller water bodies (Figures 5-3, -4, and -5). The monthly TWA increases steadily and significantly with time. Due to memory effects acquired from phase 1, the phase 2 period (2002-2005) had persistent high TWA and PWA (1990-2001). While the short dry period from 2002 to 2005 was insufficient to have a substantial impact on lakes, monthly TWA remained steady (Figure 5-9). Due to the drought condition during phase 2, the monthly TWA experienced minor fluctuations with no significant trend in the Mann-Kendall test statistic (Table 5-2). SWA depletion began in the summer of 1997 and persisted through 2003 due to persistently dry summer weather. Following this brief prairie drought (phase 2), the RRB had exceptional precipitation from 2006 to 2013. (phase 3 in Figure 5-9). Although precipitation began to increase in the fall of 2006, the wet condition did not completely develop until 2010. With 95% confidence, Table 2 demonstrates an increasing trend. The monthly TWA decreases in phase 4 (2014-2019), indicating a drying period in the RRB (Figure 5-9). At the 95% confidence level, Table 5-2 demonstrates negative trends for TWA, PWA, and SWA.

To further analyze how water area relates to climatic variability, precipitation and temperature data, as well as their temporal evolution over the research region, are considered. An additional Mann-Kendall test was done to establish the relationship between water surface area, temperature, and precipitation over the four recognized phases. Tables 5-3 and 4 exhibit the Mann-Kendall test findings for temperature and precipitation during the study period, respectively. There is no overall trend in temperature or precipitation over the study period, with the exception of an increased tendency in precipitation at the Upland station. Precipitation increased in both upland and lowland stations during the first phase, the excessively wet period from 1990 to 2001 (Table 5-4). Admittedly, there is no temperature trend in all stations throughout phase 1. We further study temperature changes throughout phase 1 and discover a period (1990-1996, $Z = -3.0$, $p = 0.001$) of cooling and wetting at Edmore (Upland) and Fargo (headwater lowland) stations. Over this time, the annual average temperature has decreased by 7 degrees Fahrenheit. Although the wetting continues throughout phase 1, there is no trend in temperature at the Edmore and Fargo stations and an upward trend at the Grand Forks station. We assume that the combination of cooling and wetting from 1990 to 1996 caused a significant rise in PWA, SWA, and monthly water areas. We believe that between 1990 and 1996, wetness provided moisture to the RRB system while cooling caused a lack of evaporation and sublimation loss, an extended winter and snow cover, and subsequent melt runoff to the RRB system.

Over the study period, an analysis of surface water area during a long-term drought-to-deluge cycle showed a net spike in temporal, permanent, and seasonal water areas in RRB. Figure 5-10 summarizes the details of such changes and shows the spatial distribution of the transitions between permanent water, seasonal water, and bare land and the net land cover changes over the last three decades. The RRB-wide transition from bare land to permanent (170 km^2) and seasonal (1851 km^2) water area is observed during the 1990-2001 period. In contrast, changes are minimal during the following stable period (2002-2005). During the most recent wetting period, 2006-2013, there was a net gain of 354 km^2 in permanent water from seasonal and bare land, whereas 434 km^2 changed from bare land to seasonal water area. These changes are primarily focused on the basin's west. Eventually, during the recent drought period (2014-2018), a large loss (462.3 km^2) of seasonal water area to bare land occurred. Table 5-5 summarized the changes in permanent and seasonal water areas, as well as barren land (non-water area), across each phase.

Table 5-2- Mann-Kendall trend tests with a p-value for the annual total, permanent, and seasonal water areas, and monthly (from Spring to Summer) total water areas in the Red River Basin for the 1990-2019, 1990-1999, 2000-2003, 20,04-2013 and 2014-2019 periods.

Period		Annual			Monthly
		Permanent	Seasonal	Total	Total
1990-2001	*Z*	4.18	2.4	2.67	11.14
	p	0.000014	0.008	0.0037	0.00
	Trend	Upward	Upward	Upward	Upward
2002-2005	*Z*	0.34	0.34	0.34	-0.34
	p	-	-	-	-
	Trend	No Trend	No Trend	No Trend	No Trend
2006-2013	*Z*	2.35	0	0.124	2.61
	P	0.009	-	-	0.004
	Trend	Upward	No Trend	No Trend	Upward
2014-2019	*Z*	0.375	0.75	0.376	-3.84
	p	0.012	-	-	0.00
	Trend	No Trend	No Trend	No Trend	Downward
1990-2019	*Z*	4.85	0.75	0.376	12.4
	p	0	-	0.037	0.00
	Trend	Upward	No Trend	Upward	Upward

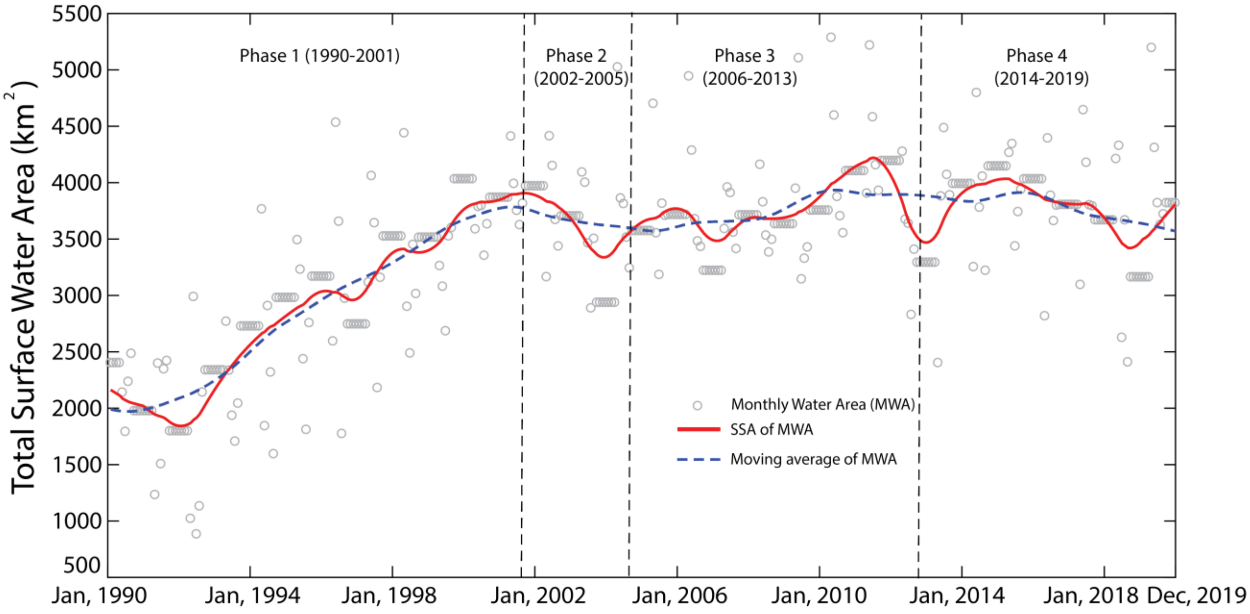

Figure 5-9- Monthly TWA, singular spectrum analyses (SSA), and moving average of monthly TWA during the study period.

Table 5-3- Mann-Kendall trend tests with a p-value for temperature in the Red River Basin for the 1990-2019, 1990-1999, 2000-2003, 20,04-2013, and 2014-2019 periods.

Period		Lowland		Upland
		Grand Forks	Fargo	Edmore
1990-2001	*Z*	-1.029	-0.206	0.069
	p	> 0.05	> 0.05	> 0.05
	Trend	No Trend	No Trend	No Trend
2002-2005	*Z*	0	-0.245	1.02
	p	> 0.05	> 0.05	> 0.05
	Trend	No Trend	No Trend	No Trend
2006-2013	*Z*	-0.124	0	-0.253
	P	>0.05	>0.05	-
	Trend	No Trend	No Trend	No Trend
2014-2019	*Z*	-0.75	-0.75	0.75
	p	>0.05	>0.05	>0.05
	Trend	No Trend	No Trend	No Trend
1990-2019	*Z*	-0.214	0.304	-0.174
	p	>0.05	>0.05	>0.05
	Trend	No Trend	No Trend	No Trend

Table 5-4- Mann-Kendall trend tests with a p-value for precipitation in the Red River Basin for the 1990-2019, 1990-1999, 2000-2003, 20,04-2013, and 2014-2019 periods.

Period		Lowland		Upland
		Grand Forks	Fargo	Edmore & Others
1990-2001	*Z*	2.5	1.787	2.336
	p	0.006	0.037	0.0098
	Trend	Upward	Upward	Upward
2002-2005	*Z*	0	1.225	1.019
	p	>0.05	>0.05	>0.05
	Trend	No Trend	No Trend	No Trend
2006-2013	*Z*	-0.124	0.124	1.361
	P	>0.05	>0.05	>0.05
	Trend	No Trend	No Trend	No Trend
2014-2019	*Z*	0.75	1.127	-0.34
	p	>0.05	>0.05	>0.05
	Trend	No Trend	No Trend	No Trend
1990-2019	*Z*	1.265	0.624	2.271
	p	>0.05	>0.05	0.0034
	Trend	No Trend	No Trend	Upward

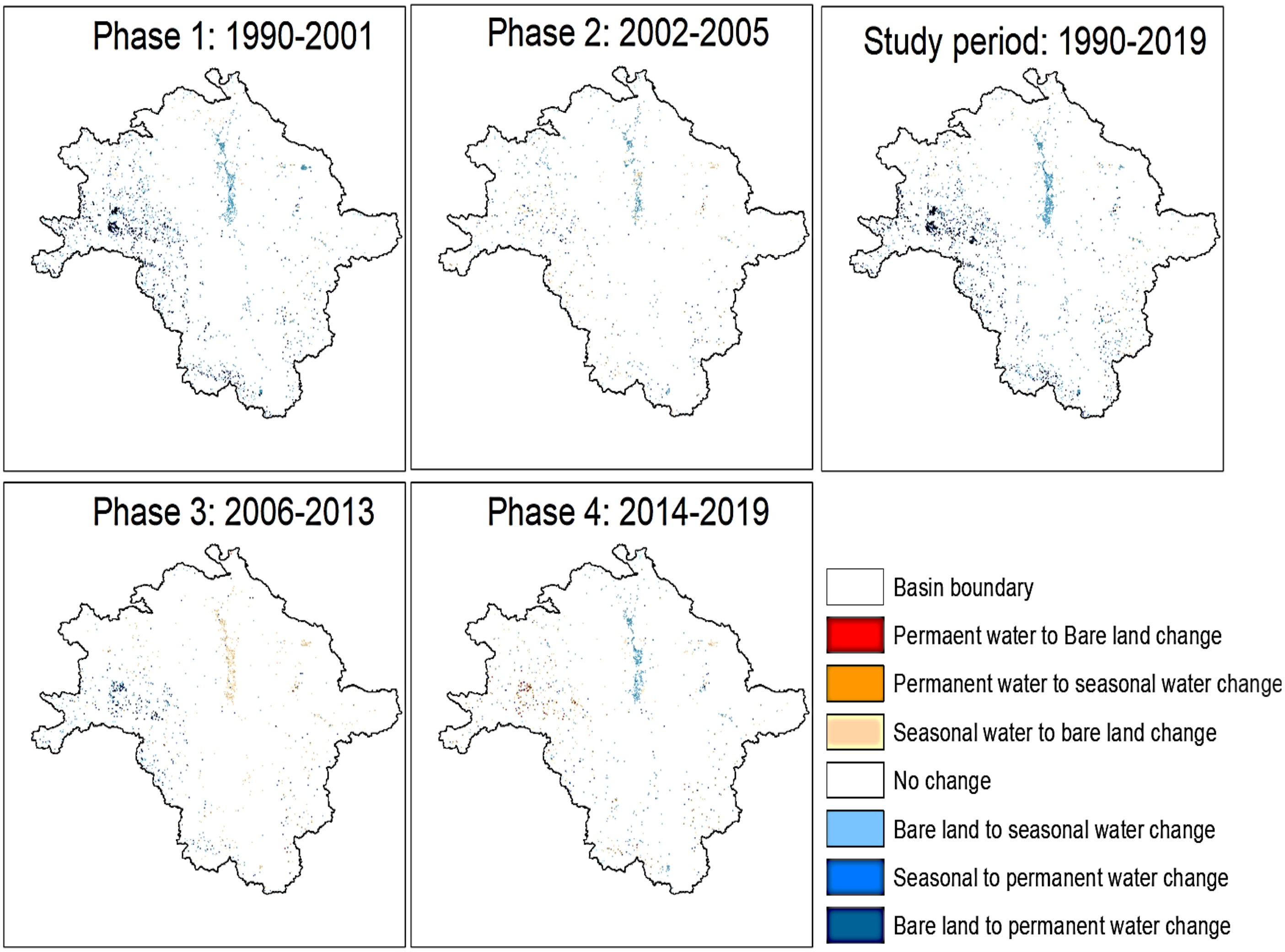

Figure 5-10- Change between permanent and seasonal water area and bare land (non-water area) during each phase and study period.

Table 5-5- Change in permanent and seasonal water area (km^2) and bare land (non-water area, km^2) during each phase.

Change	1990-01	2002-05	2006-13	2014-19	1990-2019
Permanent water to bare land	1	8	9	63	5
Permanent water to seasonal water	17	87	52	164	31
Seasonal water to bare land	141	355	812	462	143
No change	113467	115236	114889	114911	113309
Bare land to seasonal water	1851	722	435	857	1876
Seasonal water to permanent water	170	124	219	91	169
Bare land to permanent water	903	18	135	2	1018

5.5. Conclusion of Journal Paper 4

This study investigates the spatiotemporal variability of surface water area in the RRB from 1990 to 2019. We offered a more careful evaluation of the surface water area variation in RRB and noted surface water area responses to dry periods. Using the Global Surface Water Dataset (GSWD) with a 30 m resolution, we investigated permanent and seasonal water regions in this research. We discovered that the overall patterns for all total, permanent, and seasonal water areas exhibit an upward tendency during the duration of the study. From 1990 and 1997, there was an upward trend in TWA, PWA, and SWA. Such increasing trends of TWA, PWA, and SWA are partly due to cooling and wetting during the 1990-1996 period. After 1997, the seasonal water area exhibits noticeable fluctuations while the permanent water variation is slight.

From 1990 to 1998, significant depressions in Devils Lake, the largest upland watershed, were filled up and transformed into seasonal water bodies. From 2001 to 2011, these seasonal bodies of water were transformed to permanent bodies of water. We infer that since these shifts occurred, the upland has represented the Red River's permanent water area. In contrast, the transition from seasonal to permanent water occurred in the lowland between 1998 and 1999. Nevertheless, PWA declined after 2013 and was mostly converted back to SWA.

We detected four phases of variation in the surface water area, including phase 1, a wet period with a substantial increase in TWA from 1990 to 2001; phase 2 from 2002 to 2005; phase 3 from 2006 to 2013 with the acceleration of TWA increment stalled SWA; and phase 4, a dry period with a decrease in TWA from 2014 to 2019. The RRB-wide transition from bare land to permanent (170 km^2) and seasonal (1851 km^2) water area is observed during the 1990-2001 period. In contrast, during the following stable period (2002-2005), changes are minimal. In the recent wetting period of 2006-2013, a net gain of 354 km^2 in permanent water from seasonal and bare land is observed while 434 km^2 changes from bare land to the seasonal water area. These changes are heavily concentrated around the west of the basin. Finally, during the recent drying period (2014-2018), a significant loss (462.3 km^2) of seasonal water area to bare land occurred.

The PWA of upland RRB has grown faster than that of lowland RRB. As a result, significant and more frequent flooding has been reported in highland basins such as the Devils Lake Basin. Because water drains from upland to lowland via escarpment, the frequent and severe flooding in upland areas has prompted concerns about lowland floods. The fluctuations in surface water area and identified phases have major significance for forecasting future lake and wetland area responses in the RRB. Bonsal et al, (2013) predicted frequent occurrence of drought with high severity and persistent multi-year drought in the southern prairies [125]. The surface water area response to expected dry conditions in the future or wet-to-dry transition can be linked with phase 2 and phase 4 monthly TWA response. Further, the multi-year dry period (2002-2004) can be comparable to phase 2. This study can be used for preparedness for the dramatic and inevitable extreme surface water area response (flooding) and eutrophication in the Red River.

Our findings have consequences for the amount of nitrogen content in RRB lakes and wetlands, which are sensitive to eutrophication [181]. With a restricted supply from the watershed, an increase in surface water area can dilute nutrient content. Also, the geochemical environment of particular bodies of water causes denitrification. However, during hydrologically extreme events, large nutrient loads can enter the lakes and wetlands of the RRB. The use of water body determination indices such as NDWI, MNDWI, and AWEI in the Red River Basin will be investigated in our future studies. These indices will be employed to comprehensively map and monitor the spatiotemporal dynamics of water bodies in the region, as well as to estimate various water quality parameters. Our goal is to provide valuable insights into the use of remote sensing data for effective water resource management and hydrological studies in the Red River Basin.

6 Chapter 6. Conclusions and Future Directions

In conclusion, this study presented to highlight the importance of utilizing advanced techniques such as geospatial analysis, machine learning, and statistical modeling to better understand and predict floods and water level fluctuations in the Red River Basin. The findings suggest that accurate flood modeling and prediction can be achieved by incorporating various data sources, including bathymetry, flow velocity, and discharge flood data, and by employing advanced modeling techniques.

The study develops a nonlinear Muskingum model for two USGS stations and uses the Salp Swarm Algorithm to optimize the model's parameters. The optimized parameters improve the accuracy of flood predictions caused by snowmelt in icy rivers like the Red River. The results demonstrate that the Muskingum method can be effectively optimized using the SSA algorithm. The optimized parameters for the two categories suggest that NR=2 yields the optimized outflow for group “b“, whereas NR=1 produces the best results for group “a“.

This research used geospatial techniques to simulate floods on the Red River near Grafton, North Dakota, by calibrating Manning's n-coefficient. The study collected bathymetry data using ADCP and ASV with LiDAR data to determine flow during a flood event in 2022. HEC-RAS modeling generated flood mapping, revealing eddy flow after the bridge that becomes more significant with an increase in flow discharge and velocity, posing a risk for scour. The study suggests that ADCPs can be useful in flood inundation mapping studies due to their ability to integrate bathymetry, flow velocity, and discharge flood data.

In addition, three approaches for forecasting water levels in a time series, primarily for flood warning systems, were tested in this study: SARIMA, RF, and LSTM. According to the results of the investigation, the LSTM technique surpassed SARIMA and RF in terms of accuracy and prediction performance, making it a reliable choice for flood prediction. These results demonstrate the high precision of the Deep Learning algorithm as a reliable choice for flood prediction. Experimental results on Pembina, Drayton, and Grand Forks stations show a better performance with the LSTM model in all prediction times. However, to further enhance the predictive performance of machine learning models, it is recommended to incorporate a more comprehensive set of environmental variables, such as temperature, precipitation, and others. By integrating multiple predictors, we can potentially improve the accuracy and reliability of flood prediction systems in the Red River basin, thereby contributing to the development of effective flood mitigation strategies.

According to this study, the Red River Basin has seen an overall rise in water areas, including total, permanent, and seasonal water. Since 2013, the upland has seen a greater permanent water area increase, resulting in more frequent floods, whilst the lowland has seen a decline in permanent water area. The identified phases of surface water area variation can be used to anticipate future extreme flooding and eutrophication. Future studies will investigate water body determination indices to improve water resource management and hydrological studies in the region. Furthermore, our research findings on surface water changes suggest potential avenues for future investigations into the impact of flood events on nutrient concentration in lakes and wetlands of the Red River Basin. Specifically, our study highlights the potential for surface water area expansion to dilute nutrient concentration, assuming a limited supply from the Therefore, future research could explore the relationship between nutrient concentration, flood events, and other environmental variables in the RRB, which could inform the development of more effective nutrient management strategies and contribute to the preservation of the region's lakes and wetlands.

References

1. Lim, Y.H. and D.L. Voeller, Regional flood estimations in Red River using L-moment-based index-flood and bulletin 17B procedures. Journal of Hydrologic Engineering, 2009. 14(9): p. 1002-1016.
2. Board, R.R.B., Inventory team report: hydrology. Red River Basin Board: Moorhead, MN, USA, 2000.
3. Babiracki, D., Lateral Migration of the Red River, in the Vicinity of Grand Forks, North Dakota. 2015.
4. Hu, H.H., et al., Gridded snowmelt and rainfall-runoff CWMS hydrologic modeling of the Red River of the North Basin. Journal of Hydrologic Engineering, 2006. 11(2): p. 91-100.
5. Red River of the North Watershed. 2009, Minnesota Department of Natural Resources: St. Paul, Minnesota.
6. Center, D.W.S. Red River of the North at Grand Forks, North Dakota - 129 Years. Available from: https://www.usgs.gov/centers/dakota-water-science-center/red-river-north-grand-forks-north-dakota-129-years?qt-science_center_objects=0.
7. Laken, N.A., Red River of the North “A winding journey to history” Headwaters at Breckenridge, Minnesota, U.S.A. 2010.
8. Stoner, J.D., et al., RED RIVER OF THE NORTH BASIN, MINNESOTA, NORTH DAKOTA, AND SOUTH DAKOTA 1. JAWRA Journal of the American Water Resources Association, 1993. 29(4): p. 575-615.
9. Hirsch, R.M. and K.R. Ryberg, Has the magnitude of floods across the USA changed with global CO2 levels? Hydrological Sciences Journal, 2012. 57(1): p. 1-9.
10. Rice, J.S., et al., Continental US streamflow trends from 1940 to 2009 and their relationships with watershed spatial characteristics. Water Resources Research, 2015. 51(8): p. 6262-6275.
11. Akbari, G.H. and R. Barati. Comprehensive analysis of flooding in unmanaged catchments. in Proceedings of the Institution of Civil Engineers-Water Management. 2012. Thomas Telford Ltd.
12. Akbari, G.H., A.H. Nezhad, and R. Barati, Developing a model for analysis of uncertainties in prediction of floods. Journal of Advanced Research, 2012. 3(1): p. 73-79.
13. Gill, M.A., Flood routing by the Muskingum method. Journal of hydrology, 1978. 36(3-4): p. 353-363.

14. O'donnell, T., A direct three-parameter Muskingum procedure incorporating lateral inflow. Hydrological Sciences Journal, 1985. 30(4): p. 479-496.
15. Khan, M.H., Muskingum flood routing model for multiple tributaries. Water resources research, 1993. 29(4): p. 1057-1062.
16. Kshirsagar, M., B. Rajagopalan, and U. Lal, Optimal parameter estimation for Muskingum routing with ungauged lateral inflow. Journal of Hydrology, 1995. 169(1-4): p. 25-35.
17. Choudhury, P., Multiple inflows Muskingum routing model. Journal of Hydrologic Engineering, 2007. 12(5): p. 473-481.
18. Choudhury, P., R.K. Shrivastava, and S.M. Narulkar, Flood routing in river networks using equivalent Muskingum inflow. Journal of Hydrologic Engineering, 2002. 7(6): p. 413-419.
19. Samani, H.M. and G. Shamsipour, Hydrologic flood routing in branched river systems via nonlinear optimization. Journal of Hydraulic Research, 2004. 42(1): p. 55-59.
20. Orouji, H., et al. Flood routing in branched river by genetic programming. in Proceedings of the Institution of Civil Engineers-Water Management. 2014. Thomas Telford Ltd.
21. Kumar, D.N., F. Baliarsingh, and K.S. Raju, Extended Muskingum method for flood routing. Journal of Hydro-environment Research, 2011. 5(2): p. 127-135.
22. Vatankhah, A.R., Evaluation of explicit numerical solution methods of the Muskingum model. Journal of Hydrologic Engineering, 2014. 19(8): p. 06014001.
23. Wang, J., et al., Discussion of “parameter estimation of the nonlinear muskingum flood-routing model using a hybrid harmony search algorithm” by Halil Karahan, Gurhan Gurarslan, and Zong Woo Geem. Journal of Hydrologic Engineering, 2014. 839: p. 842.
24. Mirjalili, S., et al., Salp Swarm Algorithm: A bio-inspired optimizer for engineering design problems. Advances in engineering software, 2017. 114: p. 163-191.
25. Madin, L.P., Aspects of jet propulsion in salps. Canadian Journal of Zoology, 1990. 68(4): p. 765-777.
26. Anderson, P. and Q. Bone, Communication between individuals in salp chains. II. Physiology. Proceedings of the Royal Society of London. Series B. Biological Sciences, 1980. 210(1181): p. 559-574.
27. Andersen, V. and P. Nival, A model of the population dynamics of salps in coastal waters of the Ligurian Sea. Journal of plankton research, 1986. 8(6): p. 1091-1110.

28. Henschke, N., et al., Population drivers of a Thalia democratica swarm: insights from population modelling. Journal of Plankton Research, 2015. 37(5): p. 1074-1087.
29. Atashi, V., et al., Water Level Forecasting Using Deep Learning Time-Series Analysis: A Case Study of Red River of the North. Water, 2022. 14(12): p. 1971.
30. McCarthy, G., The unit hydrograph and flood routing, Conference of North Atlantic Division. US Army Corps of Engineers, New London, CT. US Engineering, 1938.
31. Das, A., Parameter estimation for Muskingum models. Journal of Irrigation and Drainage Engineering, 2004. 130(2): p. 140-147.
32. Mohan, S., Parameter estimation of nonlinear Muskingum models using genetic algorithm. Journal of hydraulic engineering, 1997. 123(2): p. 137-142.
33. Singh, V.P. and P.D. Scarlatos, Analysis of nonlinear Muskingum flood routing. Journal of Hydraulic Engineering, 1987. 113(1): p. 61-79.
34. Luo, J. and J. Xie, Parameter estimation for nonlinear Muskingum model based on immune clonal selection algorithm. Journal of Hydrologic Engineering, 2010. 15(10): p. 844-851.
35. Easa, S.M., et al. Discussion: New and improved four-parameter non-linear Muskingum model. in Proceedings of the Institution of Civil Engineers-Water Management. 2014. Thomas Telford Ltd.
36. Hosseini, S.M., Application of spreadsheets in developing flexible multiple-reach and multiple-branch methods of Muskingum flood routing. Computer Applications in Engineering Education, 2009. 17(4): p. 448-454.
37. Karahan, H., G. Gurarslan, and Z.W. Geem, A new nonlinear Muskingum flood routing model incorporating lateral flow. Engineering Optimization, 2015. 47(6): p. 737-749.
38. Farzin, S., et al., Flood routing in river reaches using a three-parameter Muskingum model coupled with an improved bat algorithm. Water, 2018. 10(9): p. 1130.
39. Yoon, J. and G. Padmanabhan, Parameter estimation of linear and nonlinear Muskingum models. Journal of Water Resources Planning and Management, 1993. 119(5): p. 600-610.
40. Fuat Toprak, Z. and M.E. Savci, Longitudinal dispersion coefficient modeling in natural channels using fuzzy logic. CLEAN–Soil, Air, Water, 2007. 35(6): p. 626-637.
41. Toprak, Z.F. and H.K. Cigizoglu, Predicting longitudinal dispersion coefficient in natural streams by artificial intelligence methods. Hydrological Processes: An

International Journal, 2008. 22(20): p. 4106-4129.

42. McCuen, R.H., Z. Knight, and A.G. Cutter, Evaluation of the Nash–Sutcliffe efficiency index. Journal of hydrologic engineering, 2006. 11(6): p. 597-602.

43. Kazemi, M. and R. Barati, Application of dimensional analysis and multi-gene genetic programming to predict the performance of tunnel boring machines. Applied Soft Computing, 2022. 124: p. 108997.

44. Hosseini, K., et al., Optimal design of labyrinth spillways using meta-heuristic algorithms. KSCE Journal of Civil Engineering, 2016. 20: p. 468-477.

45. Alizadeh, M.J., et al., Prediction of longitudinal dispersion coefficient in natural rivers using a cluster-based Bayesian network. Environmental Earth Sciences, 2017. 76: p. 1-11.

46. Todhunter, P.E., Uncertainty of the assumptions required for estimating the regulatory flood: Red River of the North. Journal of Hydrologic Engineering, 2012. 17(9): p. 1011-1020.

47. Deschamps, A., et al. Geospatial data integration for applications in flood prediction and management in the Red River Basin.

48. Abad, J.D., et al. Exploratory study of the influence of the wake produced by acoustic Doppler velocimeter probes on the water velocities within measurement volume. in World Water and Environmental Resources Congress. 2004. Salt Lake City.

49. Garcia, C.M., K. Oberg, and M.H. García, ADCP measurements of gravity currents in the Chicago River, Illinois. Journal of Hydraulic Engineering, 2007. 133(12): p. 1356-1366.

50. Vermeulen, B., A.J.F. Hoitink, and R.J. Labeur, Flow structure caused by a local cross-sectional area increase and curvature in a sharp river bend. Journal of Geophysical Research: Earth Surface, 2015. 120(9): p. 1771-1783.

51. Vermeulen, B., A.J.F. Hoitink, and M.G. Sassi, Coupled ADCPs can yield complete Reynolds stress tensor profiles in geophysical surface flows. Geophysical Research Letters 2011. 38(6).

52. Vermeulen, B., M.G. Sassi, and A.J.F. and Hoitink, Improved flow velocity estimates from moving-boat ADCP measurements. Water Resources Research, 2014. 50(5): p. 4186-4196.

53. Parsapour-Moghaddam, P. and C.D. Rennie. 3D versus 2D calibration of a 3D hydrodynamic model. in 37th IAHR World Congress. 2017a. Kuala Lumpur, Malaysia.

54. Muste, M., K. Yu, and M. Spasojevic, Practical aspects of ADCP data use for quantification of mean river flow characteristics; part I: moving-vessel measurements. Flow measurement and instrumentation, 2004. 15(1): p. 1-16.
55. Guerrero, M., et al., The acoustic properties of suspended sediment in large rivers: consequences on ADCP methods applicability. Water, 2016. 8(1): p. 13.
56. Rennie, C.D. and F. Rainville, Case study of precision of GPS differential correction strategies: Influence on aDcp velocity and discharge estimates. Journal of hydraulic engineering, 2006. 132(3): p. 225-234.
57. Vermeulen, B., M. Sassi, and A. Hoitink, Improved flow velocity estimates from moving-boat ADCP measurements. Water resources research, 2014. 50(5): p. 4186-4196.
58. Atashi, V., et al. Characteristics of Seasonality on 3D Velocity and Bathymetry Profiles in Red River of the North. in World Environmental and Water Resources Congress 2022.
59. Prabnakorn, S., et al., Development of an integrated flood hazard assessment model for a complex river system: a case study of the Mun River Basin, Thailand. Modeling Earth Systems and Environment, 2019. 5(4): p. 1265-1281.
60. Bhuyian, M.N., A.J. Kalyanapu, and F. Nardi, Approach to digital elevation model correction by improving channel conveyance. Journal of Hydrologic Engineering, 2015. 20(5): p. 04014062.
61. Cook, A. and V. Merwade, Effect of topographic data, geometric configuration and modeling approach on flood inundation mapping. Journal of hydrology, 2009. 377(1-2): p. 131-142.
62. Getahun, Y.S. and S.L. Gebre, Flood hazard assessment and mapping of flood inundation area of the Awash River Basin in Ethiopia using GIS and HEC-GeoRAS/HEC-RAS model. Journal of Civil & Environmental Engineering, 2015. 5(4): p. 1.
63. Saksena, S. and V. Merwade, Incorporating the effect of DEM resolution and accuracy for improved flood inundation mapping. Journal of Hydrology, 2015. 530: p. 180-194.
64. Merz, B., A. Thieken, and M. Gocht, Flood risk mapping at the local scale: concepts and challenges, in Flood risk management in Europe. 2007, Springer. p. 231-251.
65. Namara, W.G., T.A. Damisse, and F.G. Tufa, Application of HEC-RAS and HEC-GeoRAS model for Flood Inundation Mapping, the case of Awash Bello Flood Plain, Upper Awash River Basin, Oromiya Regional State, Ethiopia. Modeling Earth

Systems and Environment, 2022. 8(2): p. 1449-1460.

66. Zheng, X., et al., GeoFlood: Large-scale flood inundation mapping based on high-resolution terrain analysis. Water Resources Research, 2018. 54(12): p. 10,013-10,033.

67. Pinos, J., L. Timbe, and E. Timbe, Evaluation of 1D hydraulic models for the simulation of mountain fluvial floods: a case study of the Santa Bárbara River in Ecuador. Water Practice and Technology, 2019. 14(2): p. 341-354.

68. Noor, M., et al., Experimental and HEC-RAS modelling of bridge pier scouring. Journal of Advanced Research in Fluid Mechanics and Thermal Sciences, 2020. 74(1): p. 119-132.

69. Ghaderi, A., R. Daneshfaraz, and M. Dasineh, Evaluation and prediction of the scour depth of bridge foundations with HEC-RAS numerical model and empirical equations (Case Study: Bridge of Simineh Rood Miandoab, Iran). Engineering Journal, 2019. 23(6): p. 279-295.

70. Mehta, D.J. and S. Yadav, Analysis of scour depth in the case of parallel bridges using HEC-RAS. Water Supply, 2020. 20(8): p. 3419-3432.

71. Lindenschmidt, K.-E., et al., Ice jam modelling of the Lower Red River. Journal of Water Resource and Protection, 2012. 4(1): p. 1-11.

72. Richardson, E.V. and S.R. Davis, Evaluating scour at bridges. 2001, United States. Federal Highway Administration. Office of Bridge Technology.

73. Carlson, D.F., et al., An affordable and portable autonomous surface vehicle with obstacle avoidance for coastal ocean monitoring. HardwareX, 2019. 5: p. e00059.

74. Mueller, D.S., et al., Measuring discharge with acoustic Doppler current profilers from a moving boat. 2009: US Department of the Interior, US Geological Survey Reston, Virginia (EUA).

75. SonTek, RiverSurveyor S5/M9 system manual firmware version 3.00. 2012, SonTek/YSI San Diego, California.

76. Veilleux, A.G., et al., Estimating magnitude and frequency of floods using the PeakFQ 7.0 program: US Geological Survey Fact Sheet 2013–3108. US Geological Survey Fact Sheet, 2014. 2.

77. Brunner, G., CEIWR-HEC HEC-RAS River Analysis System: User’s Manual Version 6.0. US Army Corps of Engineers Institute for Water Resources, HEC, January: Davis, CA, USA, 2021.

78. Chow, V.T., Open-channel Hydraulics. New York: McGram-Hill Book Company. 1959, Inc.

79. Banks, J.C., J.V. Camp, and M.D. Abkowitz, Adaptation planning for floods: a review of available tools. Natural hazards, 2014. 70(2): p. 1327-1337.

80. U.S. Army Corps of Engineers, S.P.D., 180 Fifth Street East, Suite 700, St. Paul, Minnesota 55101-1678, Lower Red Basin Retention (LRBR) Study. 2019.

81. Charbeneau, R.J. and E.R. Holley, Backwater effects of bridge piers in subcritical flow. 2001: Center for Transportation Research, Bureau of Engineering Research ….

82. Pro, G.E., Grafton Bridge, Marshal County. 08/10/2015. p. 48.4133, -97.1377.

83. Zhao, M. and H.H. Hendon, Representation and prediction of the Indian Ocean dipole in the POAMA seasonal forecast model. Quarterly Journal of the Royal Meteorological Society: A journal of the atmospheric sciences, applied meteorology and physical oceanography, 2009. 135(639): p. 337-352.

84. Borah, D.K., Hydrologic procedures of storm event watershed models: a comprehensive review and comparison. Hydrological Processes, 2011. 25(22): p. 3472-3489.

85. Costabile, P., C. Costanzo, and F. Macchione, A storm event watershed model for surface runoff based on 2D fully dynamic wave equations. Hydrological processes, 2013. 27(4): p. 554-569.

86. Cea, L., M. Garrido, and J. Puertas, Experimental validation of two-dimensional depth-averaged models for forecasting rainfall–runoff from precipitation data in urban areas. Journal of Hydrology, 2010. 382(1-4): p. 88-102.

87. Fernández-Pato, J., D. Caviedes-Voullième, and P. García-Navarro, Rainfall/runoff simulation with 2D full shallow water equations: Sensitivity analysis and calibration of infiltration parameters. Journal of hydrology, 2016. 536: p. 496-513.

88. Caviedes-Voullième, D., P. García-Navarro, and J. Murillo, Influence of mesh structure on 2D full shallow water equations and SCS Curve Number simulation of rainfall/runoff events. Journal of hydrology, 2012. 448: p. 39-59.

89. Costabile, P., C. Costanzo, and F. Macchione, Comparative analysis of overland flow models using finite volume schemes. Journal of hydroinformatics, 2012. 14(1): p. 122-135.

90. Xia, X., et al., An efficient and stable hydrodynamic model with novel source term discretization schemes for overland flow and flood simulations. Water resources research, 2017. 53(5): p. 3730-3759.

91. Liang, X., et al., A simple hydrologically based model of land surface water and energy fluxes for general circulation models. Journal of Geophysical Research:

Atmospheres, 1994. 99(D7): p. 14415-14428.

92. Costabile, P. and F. Macchione, Enhancing river model set-up for 2-D dynamic flood modelling. Environmental Modelling & Software, 2015. 67: p. 89-107.

93. Nayak, P., et al., Short-term flood forecasting with a neurofuzzy model. Water Resources Research, 2005. 41(4).

94. Kim, B., et al., Urban flood modeling with porous shallow-water equations: A case study of model errors in the presence of anisotropic porosity. Journal of Hydrology, 2015. 523: p. 680-692.

95. Feldman, A., Hydrologic Modeling System HEC-HMS technical reference manual: US Army Corps of Engineers. Hydrologic Engineering Center (609 Second St., Davis, CA 95616), 2000.

96. Arnold, J.G., et al., Large area hydrologic modeling and assessment part I: model development 1. JAWRA Journal of the American Water Resources Association, 1998. 34(1): p. 73-89.

97. Croke, B.F., et al. Redesign of the IHACRES rainfall-runoff model. in 29th Hydrology and Water Resources Symposium. 2005.

98. Bicknell, B.R., et al., Hydrological simulation program-FORTRAN. user's manual for release 11. US EPA, 1996.

99. Fenicia, F., et al., Understanding catchment behavior through stepwise model concept improvement. Water Resources Research, 2008. 44(1).

100. Li, X.H., et al. A comparison of parameter estimation for distributed hydrological modelling using automatic and manual methods. in Advanced Materials Research. 2012. Trans Tech Publ.

101. Bui, D.T., et al., Hybrid artificial intelligence approach based on neural fuzzy inference model and metaheuristic optimization for flood susceptibilitgy modeling in a high-frequency tropical cyclone area using GIS. Journal of Hydrology, 2016. 540: p. 317-330.

102. Mosavi, A., P. Ozturk, and K.-w. Chau, Flood prediction using machine learning models: Literature review. Water, 2018. 10(11): p. 1536.

103. Yürekli, K., A. Kurunç, and F. Öztürk, Testing the residuals of an ARIMA model on the Cekerek Stream Watershed in Turkey. Turkish Journal of Engineering and Environmental Sciences, 2005. 29(2): p. 61-74.

104. Ghimire, B.N., Application of ARIMA model for river discharges analysis. Journal of Nepal Physical Society, 2017. 4(1): p. 27-32.

105. Nguyen, X.H., Combining statistical machine learning models with ARIMA for water

level forecasting: The case of the Red river. Advances in water resources, 2020. 142: p. 103656.

106. Kassem, A.A., A.M. Raheem, and K.M. Khidir, Daily Streamflow Prediction for Khazir River Basin Using ARIMA and ANN Models. Zanco Journal of Pure and Applied Sciences, 2020. 32(3): p. 30-39.

107. Singh, H. and M.R. Ray, Synthetic stream flow generation of river Gomti using ARIMA Model, in Advances in Civil Engineering and Infrastructural Development. 2021, Springer. p. 255-263.

108. Elganiny, M.A. and A.E. Eldwer, Enhancing the forecasting of monthly streamflow in the main key stations of the river nile basin. Water Resources, 2018. 45(5): p. 660-671.

109. Fernández, C., et al., Streamflow drought time series forecasting: a case study in a small watershed in North West Spain. Stochastic Environmental Research and Risk Assessment, 2009. 23(8): p. 1063-1070.

110. Mgandu, F.A., M. Mkandawile, and M. Rashid, Trend Analysis and Forecasting of Water Level in Mtera Dam Using Exponential Smoothing. 2020.

111. Faruk, D.Ö., A hybrid neural network and ARIMA model for water quality time series prediction. Engineering applications of artificial intelligence, 2010. 23(4): p. 586-594.

112. Yang, T., et al., Simulating California reservoir operation using the classification and regression-tree algorithm combined with a shuffled cross-validation scheme. Water Resources Research, 2016. 52(3): p. 1626-1651.

113. Wang, Z., et al., Flood hazard risk assessment model based on random forest. Journal of Hydrology, 2015. 527: p. 1130-1141.

114. Loos, M. and H. Elsenbeer, Topographic controls on overland flow generation in a forest–An ensemble tree approach. Journal of Hydrology, 2011. 409(1-2): p. 94-103.

115. Sahoo, B.B., et al., Long short-term memory (LSTM) recurrent neural network for low-flow hydrological time series forecasting. Acta Geophysica, 2019. 67(5): p. 1471-1481.

116. Le, X.-H., H.V. Ho, and G. Lee, River streamflow prediction using a deep neural network: a case study on the Red River, Vietnam. Korean Journal of Agricultural Science, 2019. 46(4): p. 843-856.

117. Shook, K., et al., Storage dynamics simulations in prairie wetland hydrology models: evaluation and parameterization. Hydrological Processes, 2013. 27(13): p. 1875-1889.

118. Shaw, D.A., et al., The fill–spill hydrology of prairie wetland complexes during drought and deluge. Hydrological Processes, 2012. 26(20): p. 3147-3156.
119. Bullock, A. and M. Acreman, The role of wetlands in the hydrological cycle. Hydrology and Earth System Sciences, 2003. 7(3): p. 358-389.
120. Sethre, P.R., B.C. Rundquist, and P.E. Todhunter, Remote detection of prairie pothole ponds in the Devils Lake Basin, North Dakota. GIScience & Remote Sensing, 2005. 42(4): p. 277-296.
121. Negm, A., et al., Effects of climate change on depression-focused groundwater recharge in the Canadian Prairies. Vadose Zone Journal, 2021. 20(5): p. e20153.
122. Mitsch, W.J. and M.E. Hernandez, Landscape and climate change threats to wetlands of North and Central America. Aquatic Sciences, 2013. 75(1): p. 133-149.
123. Robarts, R.D., A.V. Zhulidov, and D.F. Pavlov, The state of knowledge about wetlands and their future under aspects of global climate change: The situation in Russia. Aquatic sciences, 2013. 75(1): p. 27-38.
124. Dumanski, S., J.W. Pomeroy, and C.J. Westbrook, Hydrological regime changes in a Canadian Prairie basin. Hydrological Processes, 2015. 29(18): p. 3893-3904.
125. Bonsal, B.R., et al., An assessment of Canadian prairie drought: past, present, and future. Climate Dynamics, 2013. 41(2): p. 501-516.
126. Kolmakova, M., Hydrological and climatic variability in the river basins of the West Siberian Plain (from meteorological stations, model reanalysis and satellite altimetry data). 2012, Université Paul Sabatier-Toulouse III.
127. Harden, T.M., J.E. O'Connor, and D.G. Driscoll, Late holocene flood probabilities in the black hills, South Dakota with emphasis on the medieval climate anomaly. Catena, 2015. 130: p. 62-68.
128. Todhunter, P.E., Mean hydroclimatic and hydrological conditions during two climatic modes in the Devils Lake Basin, North Dakota (USA). Lakes & Reservoirs: Research & Management, 2016. 21(4): p. 338-350.
129. Rodell, M., et al., Emerging trends in global freshwater availability. Nature, 2018. 557(7707): p. 651-659.
130. Mahmood, T.H., et al., Hydrological responses to climatic variability in a cold agricultural region. Hydrological Processes, 2017. 31(4): p. 854-870.
131. Stadnyk, T., et al., The 2011 flood event in the Red River Basin: causes, assessment and damages. Canadian Water Resources Journal/Revue canadienne des ressources hydriques, 2016. 41(1-2): p. 65-73.
132. Blais, E.-L., J. Greshuk, and T. Stadnyk, The 2011 flood event in the Assiniboine

River Basin: causes, assessment and damages. Canadian Water Resources Journal/Revue Canadienne des Ressources Hydriques, 2016. 41(1-2): p. 74-84.

133. Kharel, G., H. Zheng, and A. Kirilenko, Can land-use change mitigate long-term flood risks in the Prairie Pothole Region? The case of Devils Lake, North Dakota, USA. Regional Environmental Change, 2016. 16(8): p. 2443-2456.

134. Todhunter, P.E. and R. Fietzek-DeVries, Natural hydroclimatic forcing of historical lake volume fluctuations at Devils Lake, North Dakota (USA). Natural Hazards, 2016. 81(3): p. 1515-1532.

135. Bonsal, B.R., et al., Drought research in Canada: A review. Atmosphere-Ocean, 2011. 49(4): p. 303-319.

136. Wang, S. and H.A. Russell, Forecasting snowmelt-induced flooding using GRACE satellite data: A case study for the Red River watershed. Canadian Journal of Remote Sensing, 2016. 42(3): p. 203-213.

137. Liu, G., et al., Discharge and water-depth estimates for ungauged rivers: Combining hydrologic, hydraulic, and inverse modeling with stage and water-area measurements from satellites. Water Resources Research, 2015. 51(8): p. 6017-6035.

138. Kelly, S.A., et al., Human amplified changes in precipitation–runoff patterns in large river basins of the Midwestern United States. Hydrology and Earth System Sciences, 2017. 21(10): p. 5065-5088.

139. Vanderhoof, M.K. and L.C. Alexander, The role of lake expansion in altering the wetland landscape of the Prairie Pothole Region, United States. Wetlands, 2016. 36(2): p. 309-321.

140. Vanderhoof, M.K., L.C. Alexander, and M.J. Todd, Temporal and spatial patterns of wetland extent influence variability of surface water connectivity in the Prairie Pothole Region, United States. Landscape Ecology, 2016. 31(4): p. 805-824.

141. Pekel, J.-F., et al., High-resolution mapping of global surface water and its long-term changes. Nature, 2016. 540(7633): p. 418-422.

142. Gulbin, S., Impact Of Wetlands Loss On The Long-Term Flood Risks Of Devils Lake In A Changing Climate. 2017: The University of North Dakota.

143. Van Hoy, D.F., et al., Mechanisms of cold region hydrologic change to recent wetting in a northern glaciated landscape. Water Resources Research, 2020. 56(7): p. e2019WR026932.

144. Archambault, A.L., Wetland Dynamics In A Terminal Lake Basin: Implications To Recent Hydroclimatic Evolution. 2019.

145. Rasouli, K., et al., Linking hydrological variations at local scales to regional climate teleconnection patterns. Hydrological Processes, 2020. 34(26): p. 5624-5641.

146. Kendall, M.G., Rank correlation methods. 1948.

147. de Loë, R., Sharing the waters of the Red River basin: a review of options for transboundary water governance. Prepared for International Red River Board, International Joint Commission. Rob de loë Consulting Services, Guelph, Canada.[online] URL: http://www.ijc.org/files/publications/Sharing%20the%20Waters%20of%20the%20Red%20River%20Basin.pdf, 2009.

148. Rogers, P., et al., A comparative hydrometeorological analysis of the 2009, 2010, and 2011 Red River of the North Basin Spring floods. National Weather Service, Central Region Technical Attachment, 2013(13-03).

149. Belda, M., et al., Climate classification revisited: from Köppen to Trewartha. Climate research, 2014. 59(1): p. 1-13.

150. Peel, M.C., B.L. Finlayson, and T.A. McMahon, Updated world map of the Köppen-Geiger climate classification. Hydrology and earth system sciences, 2007. 11(5): p. 1633-1644.

151. Krenz, G. and J. Leitch, A river runs north: managing an international river. 1993: Red River Water Resources Council.

152. Group, P.C., 30-year normals. 2015, Oregon State University Corvallis, OR, USA.

153. Bengtson, M.L. and G. Padmanabhan, A hydrologic model for assessing the influence of wetlands on flood hydrographs in the Red River Basin: Development and application. 1999: Citeseer.

154. Juliano, K. and S.P. Simonovic, The impact of wetlands on flood control in the Red River Valley of Manitoba. Final Report to International Joint Commission, International Joint Commission, Washington, DC, 1999.

155. Simonovic, S. and K. Juliano, The role of wetlands during low frequency flooding events in the Red River basin. Canadian Water Resources Journal, 2001. 26(3): p. 377-397.

156. Hearne, R.R., Evolving water management institutions in the Red River Basin. Environmental Management, 2007. 40(6): p. 842-852.

157. de Loë, R., Sharing the waters of the Red River basin: a review of options for transboundary water governance. Prepared for International Red River Board, International Joint Commission. Rob de loë Consulting Services, Guelph, Canada.[online] URL: http://www. ijc. org/files/publications/Sharing% 20the%

20Waters% 20of% 20the% 20Red% 20River% 20Basin. pdf 2009 2009.

158. Zhang, B., F.W. Schwartz, and G. Liu, Systematics in the size structure of prairie pothole lakes through drought and deluge. Water Resources Research, 2009. 45(4).

159. Galloway, J.M., Simulation of the effects of the Devils Lake State Outlet on hydrodynamics and water quality in Lake Ashtabula, North Dakota, 2006-10. 2011, U. S. Geological Survey.

160. USGS, L.M., Landsat 8 Data Users Handbook. 2016, United States Geological Survey, Reston.

161. Gorelick, N., et al., Google Earth Engine: Planetary-scale geospatial analysis for everyone. Remote sensing of Environment, 2017. 202: p. 18-27.

162. Kartikeyan, B., K.L. Majumder, and A. Dasgupta, An expert system for land cover classification. IEEE Transactions on geoscience and remote sensing, 1995. 33(1): p. 58-66.

163. Lu, D. and Q. Weng, A survey of image classification methods and techniques for improving classification performance. International journal of Remote sensing, 2007. 28(5): p. 823-870.

164. Shoshany, M., Knowledge based expert systems in remote sensing tasks: quantifying gain from intelligent inference. Int. Soc. Photogramm. Remote Sens. Arch., 2008. 37: p. 1085-1088.

165. Keim, D.A., et al., Visual analytics: Scope and challenges, in Visual data mining. 2008, Springer. p. 76-90.

166. Yang, J.-B. and D.-L. Xu, On the evidential reasoning algorithm for multiple attribute decision analysis under uncertainty. IEEE Transactions on Systems, Man, and Cybernetics-Part A: Systems and Humans, 2002. 32(3): p. 289-304.

167. Guo, J., et al., Singular spectrum analysis of ionospheric anomalies preceding great earthquakes: Case studies of Kaikoura and Fukushima earthquakes. Journal of geodynamics, 2019. 124: p. 1-13.

168. Shen, Y., et al., Long-term prediction of polar motion using a combined SSA and ARMA model. Journal of Geodesy, 2018. 92(3): p. 333-343.

169. Vautard, R. and M. Ghil, Singular spectrum analysis in nonlinear dynamics, with applications to paleoclimatic time series. Physica D: Nonlinear Phenomena, 1989. 35(3): p. 395-424.

170. Yiou, P., E. Baert, and M.-F. Loutre, Spectral analysis of climate data. Surveys in Geophysics, 1996. 17(6): p. 619-663.

171. Golyandina, N., V. Nekrutkin, and A.A. Zhigljavsky, Analysis of time series structure: SSA and related techniques. 2001: CRC press.

172. Mann, H.B., Nonparametric tests against trend. Econometrica: Journal of the econometric society, 1945: p. 245-259.

173. Önöz, B. and M. Bayazit, The power of statistical tests for trend detection. Turkish journal of engineering and environmental sciences, 2003. 27(4): p. 247-251.

174. Partal, T. and M. Küçük, Long-term trend analysis using discrete wavelet components of annual precipitations measurements in Marmara region (Turkey). Physics and Chemistry of the Earth, Parts A/B/C, 2006. 31(18): p. 1189-1200.

175. Adamowski, K., A. Prokoph, and J. Adamowski, Development of a new method of wavelet aided trend detection and estimation. Hydrological Processes: An International Journal, 2009. 23(18): p. 2686-2696.

176. Todhunter, P., Hydrological basis of the Devils Lake, North Dakota (USA), terminal lake flood disaster. Natural Hazards, 2021. 106(3): p. 2797-2824.

177. Vanderhoof, M.K., et al., The influence of data characteristics on detecting wetland/stream surface-water connections in the Delmarva Peninsula, Maryland and Delaware. Wetlands Ecology and Management, 2018. 26(1): p. 63-86.

178. Borja, S., Z. Kalantari, and G. Destouni, Global wetting by seasonal surface water over the last decades. Earth's Future, 2020. 8(3): p. e2019EF001449.

179. Donchyts, G., et al., Earth's surface water change over the past 30 years. Nature Climate Change, 2016. 6(9): p. 810-813.

180. Subin, Z., et al., Resolving terrestrial ecosystem processes along a subgrid topographic gradient for an earth-system model. Hydrology and Earth System Sciences Discussions, 2014. 11(7): p. 8443-8492.

181. Jeannotte, T.L., et al., Impacts of cold region hydroclimatic variability on phosphorus exports: Insights from concentration-discharge relationship. Journal of Hydrology, 2020. 591: p. 125312.